Air Force Institute of Technology

AFIT Scholar

9-2010

All Solid-State Mid-IR Laser Development, Nonlinear Absorption Investigation and Laser-Induced Damage Study

Torrey J. Wagner

Follow this and additional works at: https://scholar.afit.edu/etd

Part of the Materials Science and Engineering Commons, and the Plasma and Beam Physics Commons

www.manaraa.com

ALL SOLID-STATE MID-IR LASER DEVELOPMENT,

NONLINEAR ABSORPTION INVESTIGATION

AND LASER-INDUCED DAMAGE STUDY

DISSERTATION

Torrey J. Wagner, Major, USAF

AFIT/DS/ENP/10-S07

DEPARTMENT OF THE AIR FORCE
AIR UNIVERSITY

AIR FORCE INSTITUTE OF TECHNOLOGY

Wright-Patterson Air Force Base, Ohio

APPROVED FOR PUBLIC RELEASE; DISTRIBUTION UNLIMITED

The views expressed in this dissertation are those of the author and do not reflect the official policy or position of the United States Air Force, Department of Defense, or the United States Government.

AFIT/DS/ENP/10-S07

ALL SOLID-STATE MID-IR LASER DEVELOPMENT,

NONLINEAR ABSORPTION INVESTIGATION

AND LASER-INDUCED DAMAGE STUDY

DISSERTATION

Presented to the Faculty

Graduate School of Engineering and Management

Air Force Institute of Technology

Air University

Air Education and Training Command

In Partial Fulfillment of the Requirements for the

Degree of Doctor of Philosophy

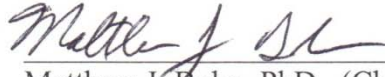Torrey J. Wagner, BS, MS
Major, USAF

August 2010

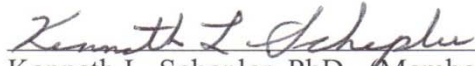APPROVED FOR PUBLIC RELEASE; DISTRIBUTION UNLIMITED

AFIT/DS/ENP/10-S07

ALL SOLID-STATE MID-IR LASER DEVELOPMENT,

NONLINEAR ABSORPTION INVESTIGATION

AND LASER-INDUCED DAMAGE STUDY

Torrey J. Wagner
Major, USAF

Approved:

_____ 14 Jul 2010
Matthew J. Bohn, PhD   (Chairman)   Date

_____ 14 July 2010
Kenneth L. Schepler, PhD   (Member)   Date

_____ 16 July 2010
Robert L. Hengehold, PhD   (Member)   Date

_____ 15 Jul 2010
Ronald A. Coutu Jr., PhD   (Member)   Date

Accepted:

_____\\ SIGNED _____   ___5 Aug 2010___
M. U. Thomas, PhD   Date
Dean, Graduate School of
Engineering and Management

Abstract

In this research, nonlinear optical absorption coefficients and laser-induced damage thresholds are measured in Ge and GaSb, which are materials that are used in IR detectors. Using a simultaneous fitting technique to extract nonlinear absorption coefficients from data at two pulse widths, two-photon and free-carrier absorption coefficients are measured in Ge and GaSb at 2.05 and 2.5 μm for the first time. At these wavelengths, nonlinear absorption is the primary damage mechanism, and damage thresholds at picosecond and nanosecond pulse widths were measured and agreed well with modeled thresholds using experimentally measured parameters. The damage threshold for a single-layer Al_2O_3 anti-reflective coating on Ge was 55% or 35% lower than the uncoated threshold for picosecond or nanosecond pulses, respectively. It was necessary to develop a pulsed 2.5 μm wavelength laser to conduct these measurements, as prior lasers at this wavelength possessed insufficient pulse energy to induce nonlinear absorption or damage these materials. Using a Cr^{2+}:ZnSe gain medium, a 3.1 mJ pulse energy laser was created whose peak power exceeded all Cr^{2+}:ZnSe literature by a factor of eight. The characteristics of the laser include nanosecond pulse width, 52% slope efficiency, beam quality of $M^2 = 1.4$, Gaussian spatial profile and a spectral line width of 110 nm.

Acknowledgements

First of all, I would like to express my sincere appreciation to my faculty advisor and committee for their guidance, support and patience throughout the course of the dissertation effort. I am indebted to the teams at AFRL/RYJW and AFRL/RXPJ for teaching me the basics, the advanced methods and showing me how to do these experiments the right way. Without any directive from above, they have given me countless hours explaining theories, weeks in the lab and months of on-call support which has directly contributed to the success of this effort.

Thanks to the personnel at the AFIT cleanroom, who spent hours with me studying damage spots and materials with their SEM and AFM. I also appreciated the assistance from University of Dayton and University of New Mexico faculty members for the optical coatings and theoretical understanding, SRI international for the full band structure model used to verify a portion of this work and also UCLA for the refurbished CTH:YAG pump laser. Finally, I have been completely sustained by my family during this stressful time – thanks for being my cheering section every night when I come home for dinner!

Torrey J. Wagner

Table of Contents

List of Figures

List of Tables

ALL SOLID-STATE MID-IR LASER DEVELOPMENT,

NONLINEAR ABSORPTION INVESTIGATION

AND LASER-INDUCED DAMAGE STUDY

Chapter 1. **Introduction**

In this introductory chapter, the objectives of this research that will advance the art and science of mid-IR laser design and effects analysis are presented, and several factors are discussed that motivated this work.

The broad goals of this research were to develop a high pulse energy mid-IR solid-state laser source and then use that source (and others) in a nonlinear absorption (NLA) investigation in conjunction with a laser-induced damage study. NLA data from two pulse widths at the same frequency were used to isolate and extract the values of intrinsic two photon absorption (TPA) and free carrier absorption (FCA) coefficients. Then, as NLA effects are the primary damage mechanism in semiconductors illuminated by sub-bandgap photons, it is a logical extension to use the coefficients extracted to predict the conditions under which damage will occur and then test this parameter space.

Objectives

There were four specific objectives in this research. The first was to develop a gain-switched, high pulse energy Cr^{2+}:ZnSe 2.5 μm pulsed laser. The second was to measure the nonlinear absorption coefficients of germanium (Ge) and gallium antimonide (GaSb) at 2.05 μm and 2.5 μm as these materials can be used in either IR detectors or optical limiters. These materials were also selected to study the difference in nonlinear

absorption and laser-induced damage between direct bandgap (GaSb) and indirect bandgap (Ge) semiconductors. The third objective was to model the dynamics of nonlinear absorption that lead to surface temperature rise and eventually thermal damage from a single laser pulse. The final objective was to test the laser-induced damage threshold due to nonlinear effects and compare with modeled results.

Motivation

This research was motivated by pressing needs in the area of mid-IR laser development, application of nonlinear optical material properties and the need to understand the damage mechanisms that result from these material properties.

Laser development: Eye-safe mid-IR laser source technology is needed for numerous military, medical and scientific uses. These uses include sensing of the battle space, providing active sources for countermeasures, spectroscopic material identification at range, many forms of laser surgery, medical diagnostics and atmospheric sensing. For the reasons described above, it is important to generate laser power in the atmospheric transmission windows of 2-5 µm and 8-12 µm. A chromium-doped zinc selenide (Cr^{2+}:ZnSe) laser is an excellent source for nonlinear frequency conversion which could be used to access all of the 2-5 µm and 8-12 µm regions

A Cr^{2+}:ZnSe laser gives output centered at 2.5 µm and can be tuned from 1.9-3.1 µm, however, the lower atmosphere does not transmit well from 2.5 µm to 2.85 µm. This is primarily due to absorption from water vapor, CO_2, N_2O and CH_4. This absorption is shown in Figure 1, which was created by Fiorino *et al* from a HiTran-based model named LEEDR [1], and shows transmittance along a 1 km path at sea level in a mid-latitude summer atmosphere.

2
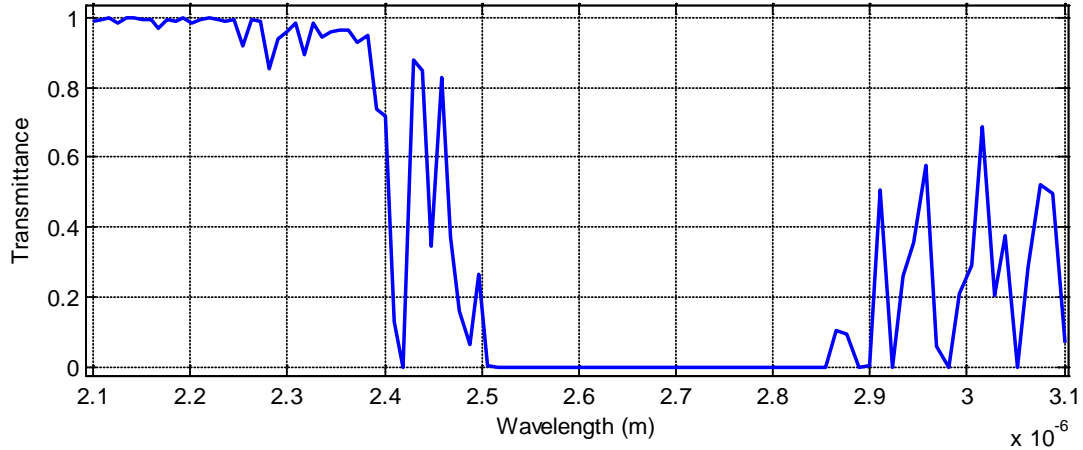
Figure 1. Transmittance through 1 km of standard atmosphere

There is interest in Cr^{2+}:ZnSe lasers despite significant atmospheric absorption over part of its emission spectrum, as the laser is broadly tunable into regions with good transmittance. The tuning curve of a nonlinear frequency conversion device was calculated using conservation of photon energy and conservation of photon momentum and is shown in Figure 2. The material is orientation-patterned GaAs (OPGaAs), where a 141μm grating period is used to convert a 2.2-2.45 μm Cr^{2+}:ZnSe pump into a 3.8-5.2 μm signal/idler.

Nonlinear and damage studies: Since the invention of the laser [2,3], incrementally shorter pulses and higher mid-IR pulse energies have been demonstrated [4], resulting in high peak irradiances which can cause significant changes in optical material properties. As observed in this work, the absorption of a material can change nonlinearly from less than 5% to greater than 90% based solely on the level of incident irradiance. The absorbed energy is converted to heat in the material, which is why the subjects of nonlinear absorption and damage are intertwined.

3
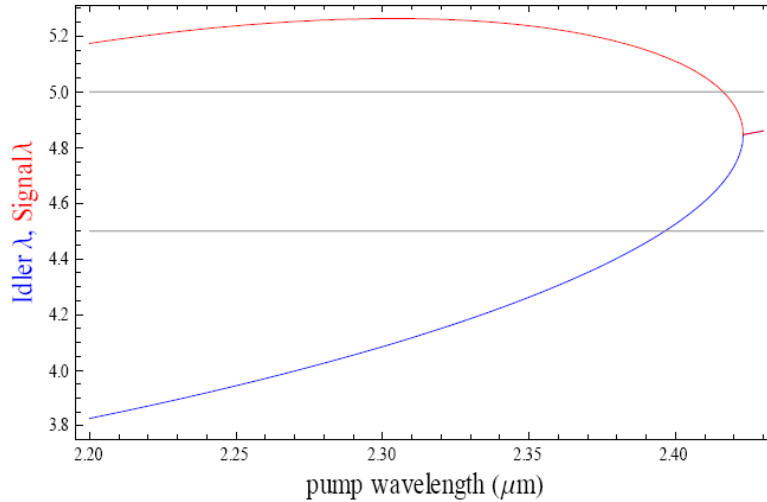
Figure 2. Nonlinear optical frequency conversion in OPGaAs

As higher power mid-IR laser sources are developed, the nonlinear properties of materials need to be measured and understood so that the effects and resulting vulnerabilities can be assessed. There are numerous applications of NLA and damage, which can be separated into applications where these effects are desired and where these effects are a design constraint. NLA has been exploited in the widely-ranging areas of nonlinear spectroscopy, mid-IR laser surgery, measurement of ultrashort pulses, and high speed all-optical switching [5]. The effect can be used to protect military sensors [6,7], or damage sensors if the appropriate wavelength and irradiance are chosen [8,9]. In industry, NLA has been used in micromachining and lithography for IC fabrication [10].

There are many situations where an understanding of nonlinear absorption is necessary to avoid the effect. NLA can limit the transmitted power used in optical communications [11]. In laser design, especially at UV wavelengths, NLA is a performance limiting factor for optics used in the National Ignition Facility in the USA and the Laser MegaJoule facility in France [12,13].

4

Chapter 2.   Theory

Background research and literature review was conducted in the areas of nonlinear absorption and laser-induced damage studies to set the stage for this research effort. This chapter also documents the development of a finite difference model that incorporates the nonlinear absorption theory that is presented.

Nonlinear Absorption Investigation

In this section the fundamental parameters and processes that contribute to NLA are described. Theoretical and empirical methods of predicting NLA parameters are explored and then the literature is reviewed for prior studies in Ge and GaSb.

Nonlinear absorption was first proposed in 1931 by Nobel laureate Maria Goppert-Mayer [14] and was presented in her dissertation under the advice of Max Born at the University of Göttingen, Germany. However, two-photon absorption (TPA) could not be confirmed without the high irradiances provided by the invention of the laser in 1960, and this effect was first observed in 1961 by Kaiser and Garret [15].

At high irradiances, nonlinear effects can cause absorption and refraction in materials that are transparent at low irradiances. Nonlinearities are wavelength-dependent, and as higher power laser sources are developed at 2.5 μm [4], the nonlinear properties of materials at this wavelength need to be studied.

The bandgap (E_{gap}) separating the conduction and valence bands of a material determine which wavelengths pass through without absorption. Bandgaps of materials relevant to this dissertation are listed in Table 1, along with a conversion to equivalent photon energy.

5

Table 1. Material bandgaps and equivalent wavelengths

Material	Bandgap (eV / λ)	0.5 * Bandgap (eV / λ)	Reference
InSb	0.17 eV / 7.3 μm	0.09 eV / 14 μm	[16]
Ge	0.67 eV / 1.9 μm	0.34 eV / 3.7 μm	[17]
GaSb	0.7 eV / 1.8 μm	0.35 eV / 3.5 μm	[17]
GaAs	1.4 eV / 0.9 μm	0.70 eV / 1.8 μm	[17]
ZnSe	2.7 eV / 0.5 μm	1.4 eV / 0.9 μm	[18]

A photon at a wavelength of 2.5 μm has an energy of 0.50 eV. Using the bandgap property, GaAs and GaSb will be transparent to a 2.5 μm photon at low intensities as their bandgap energy is greater than the photon energy. However, the same photon will not transmit through InSb due to linear absorption.

At high irradiances, the first multi-photon ionization process that develops is two-photon absorption (TPA). As the name implies, two photons raise one electron to the conduction band using a virtual state, and the possible range of photon energies absorbed is $0.5E_{gap} < E_{photon} < E_{gap}$, as shown in Table 1. At high irradiances, a 2.5 μm photon could be absorbed in GaSb and Ge due to TPA, and nonlinear absorption will be the dominant damage mechanism. Also, if the irradiance is great enough, tunneling ionization and higher multi-photon absorption will contribute as described later in the damage study section of this chapter [19].

The optically and thermally excited carriers generated by linear and nonlinear absorption cause many processes that govern the interaction of an optical wave and a semiconductor material, as shown in Figure 3. These processes and their related parameters are then defined and discussed.
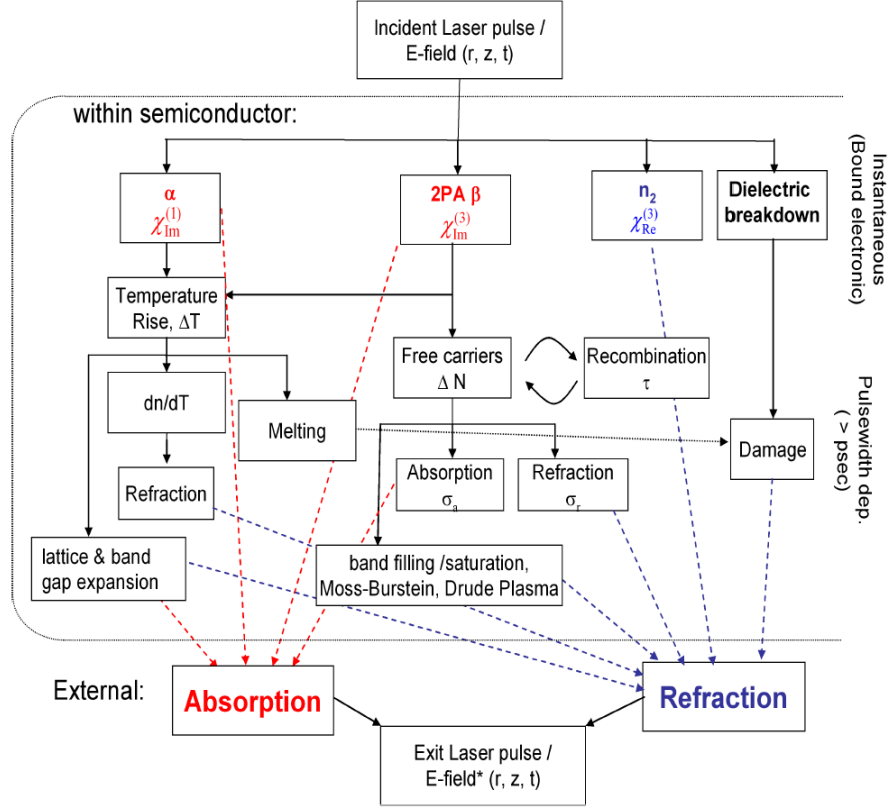
Figure 3. Linear and nonlinear optical processes within a semiconductor [20]

The processes in Figure 3 affect the level of absorption, heat rise and carrier density in a material and causes radiation to propagate according to Eq. 1-3 [21]:

$$\frac{dI}{dz} = -\alpha I - \beta I^2 - \sigma(N_0 + N)I \tag{1}$$

$$\frac{dN}{dt} = \frac{\alpha I}{h\nu} + \frac{\beta I^2}{2h\nu} - \frac{N}{\tau_R} \tag{2}$$

$$\frac{dT}{dt} = \frac{\alpha I}{\rho C} + \frac{\beta I^2}{\rho C} + \frac{\sigma(N_0 + N)I}{\rho C} \tag{3}$$

The parameters in Eq. 1-3 that govern linear and nonlinear absorption are defined in Table 2, and are further discussed in this section. These equations ignore three-photon (and higher) absorption, tunneling ionization and impact ionization. Eq. 3 assumes that

7

all absorbed energy is immediately transferred to the lattice, and further assumptions stated in the *Finite Difference Model* section of this chapter.

Table 2. Nonlinear rate equation parameters

Symbol	Parameter	Units
I	Irradiance	W/cm^2
α	Linear absorption coefficient	cm^{-1}
β	Two-photon absorption coefficient	cm/GW
σ	Free carrier absorption coefficient	cm^2
N_0	Intrinsic free carrier density	cm^{-3}
N	Generated free carrier density	cm^{-3}
hv	Photon energy	J
τ_R	Free carrier relaxation time	s
T	Temperature	K
ρ	Density of material	g/cm^3
C	Specific heat of material	J/gK

NLA is highly dependent on pulse width, as shown in Figure 4 where predicted transmission for several pulse widths is calculated using Eq. 1-3. For shorter pulses, higher peak irradiance can be tolerated before nonlinear absorption occurs, but all pulse widths are susceptible. In Figure 4, the x-axis is the peak pulse irradiance which ranges from 1 MW/cm^2 to 1 TW/cm^2.

Linear and Nonlinear Absorption Parameters

The parameters in Eq. 1-3 that affect absorption in semiconductors due to both instantaneous and cumulative effects are described in this section.

8
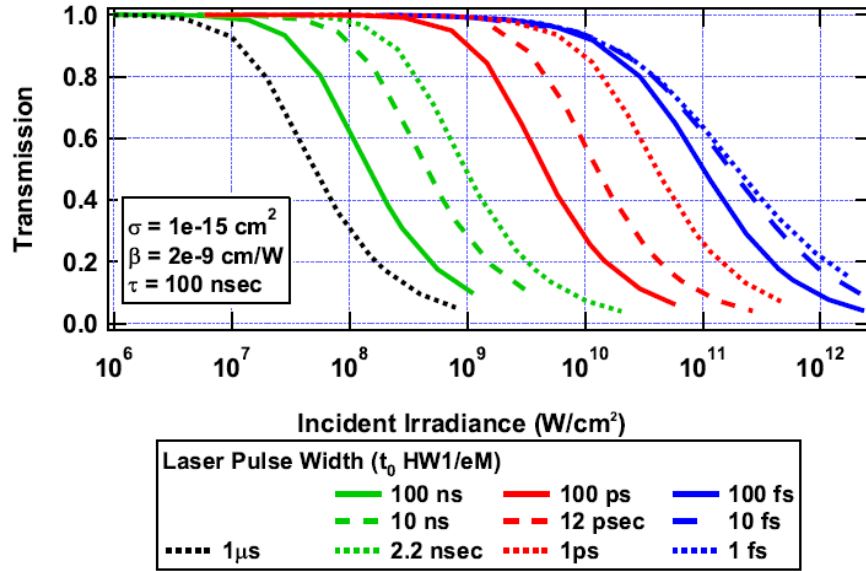
Figure 4. Theoretical nonlinear transmission variation with pulse width and peak pulse irradiance [20]

Two-photon absorption

Two photon absorption (TPA) is an instantaneous process that occurs when two photons bridge the material bandgap using a virtual state. The level of two photon absorption that occurs in a material is dependent on the irradiance squared and is described by a coefficient β that is typically expressed in units of cm/GW. For example, if a material has $\beta = 1.2$ cm/GW, that means that at an irradiance of 1 GW/cm^2, the material will absorb as if $\alpha = 1.2$ cm^{-1}.

This nonlinear irradiance-dependent absorption is proportional to the 3rd order nonlinear susceptibility χ^3, and does not depend on the material doping level. This susceptibility can be described quantum mechanically as the sum of all possible optical transitions (ω_i, ω_{jj}) and their respective dipole moments (μ_i, μ_{jj}) [22]:

9

$$\chi^{(3)}(\pm\omega_1, \pm\omega_2, \pm\omega_3) = \qquad (4)$$

$$\frac{N}{\hbar^3} \sum_{i,j,k,l} \sum_{a,u,b} \mu_{ga} \frac{\mu_{au}}{(\omega_{ag} \mp \omega_i)} \frac{\mu_{ub}}{(\omega_{ug} \mp \omega_i \mp \omega_j)} \frac{\mu_{bg}}{(\omega_{bg} \mp \omega_i \mp \omega_j \mp \omega_k)}$$

Degenerate TPA is studied in this work, where two photons of equal energy combine to bridge the material bandgap, which is acknowledged by setting $\omega_2 = \omega_3$ in Eq. 4. It is also possible to study non-degenerate TPA using two beams of differing frequencies. While nonlinear refraction (n_2) is proportional to the real part of $\chi^{(3)}$, two-photon absorption is proportional to the imaginary part of $\chi^{(3)}$ [22]:

$$\beta(\omega_1; \omega_2) = \frac{3\omega_1}{2\varepsilon_o n_o(\omega_1) n_o(\omega_2) c^2} \Im\{\chi^{(3)}(\omega_1, -\omega_2, -\omega_2)\} \qquad (5)$$

The polarization response $\bar{P}$ of a material is determined by its complex linear and nonlinear susceptibilities, which can be expressed as a series:

$$\bar{P} = \varepsilon_o \left[\chi^{(1)} + \chi^{(2)} E + \chi^{(3)} E^2 + \cdots \right] E \qquad (6)$$

Finally, the polarization response couples into the nonlinear wave equation, which can be derived from Maxwell's equations where E is the electric field and c is the speed of light:

$$\nabla \times (\nabla \times) E + \frac{1}{c^2} \frac{\partial^2}{\partial t^2} E = \frac{4\pi}{c^2} \frac{\partial^2 \bar{P}}{\partial r^2} \qquad (7)$$

Now that a theoretical perspective of two-photon absorption has been established, an empirical method is presented. β can be predicted from the bandgap E_g, photon energy E_p, Kane parameter K and index n using Van Stryland's empirical simplification to Wherrett's scaling law given in Eq. 8 [23,24]:

10

$$\beta(\omega) = K \frac{\sqrt{E_p}}{n^2(\omega)E_g^3} F_2\left(\frac{hv}{E_g}\right) \text{ where } F_2(x) = \frac{(2x-1)^{1.5}}{(2x)^5} \text{ and } x = \frac{hv}{E_{gap}} \qquad (8)$$

Using this method for Ge and GaSb, estimated β vs. wavelength has been

calculated in Figure 5, which shows its variation with wavelength and relative magnitude.

Ge two photon absorption: Bandgap=0.80 eV, n=4.06
GaSb two photon absorption: Bandgap=0.726 eV, n=3.749
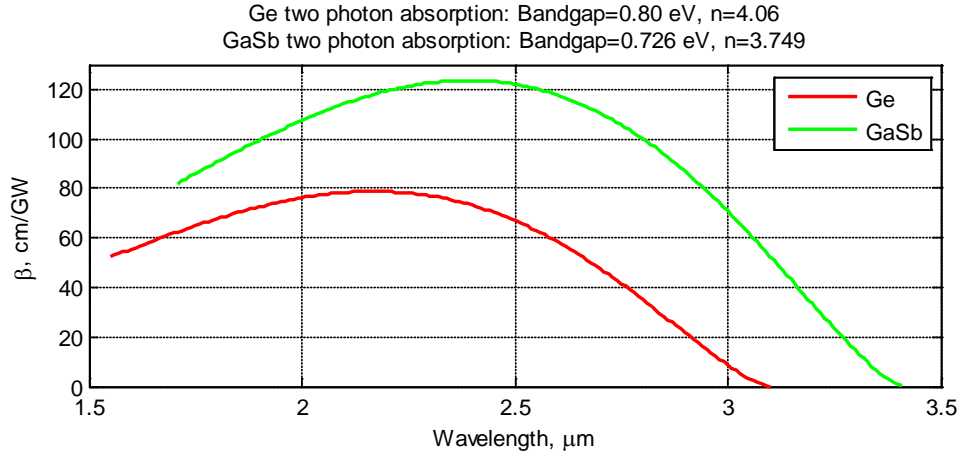
Figure 5. TPA coefficient theoretical calculations for Ge and GaSb

Free carrier absorption

Free carrier absorption (FCA) is an optical transition where a photon is absorbed

by an excited carrier (electron or hole), and is proportional to the free carrier absorption

cross section σ. This cross section is dependent on wavelength and temperature and is

related to the free carrier density N by the expression $\alpha_{FCA} = \sigma N$ [25]. σ is expressed in

units of cm^2 – if a material has $\sigma = 1 \times 10^{-16}$ cm^2, that means that at a free carrier density

$N = 1 \times 10^{16}$ cm^{-3}, the material will absorb as if $\alpha = 1$ cm^{-1}. Referencing Figure 6,

absorption can occur from free electrons in the conduction band or from free holes in the

valence band.

11

An expression that describes the variation of free carrier absorption α_{FCA} with wavelength is given in [26]:

$$\alpha_{FCA}(\lambda) = \frac{\lambda^2 N e^3}{4\pi^2 c^3 n_o \epsilon_o m_{eff}^2 \mu} \tag{9}$$

In Eq. 9, e, c, n_o, ϵ_o, μ and m_{eff} are defined as electron charge, speed of light, index of refraction, vacuum permittivity, vacuum permeability and effective mass, respectively. Additionally, α_{FCA} is directly proportional to σ, so this expression states that $\sigma \sim \lambda^2$.
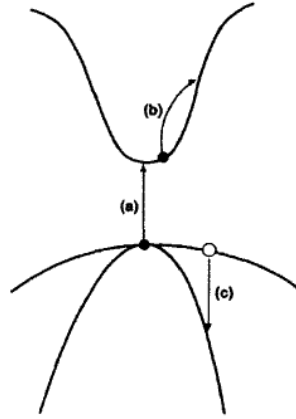
Figure 6. Sources of free carrier effects: a) electron-hole pair creation, b) intraband optical/thermal excitation, c) intervalence band transition [26]

This is a cumulative nonlinearity as there is a lifetime associated with the excited carriers. The free carriers will continue to absorb until they relax, which occurs at a material-dependent rate. Because of this effect, conventional wisdom has held that β can be isolated with an ultrashort pulse. That pulse width (τ_p) is derived in a recent work [27], which states that the pulse width must satisfy the condition in Eq. 10 to isolate β:

$$\tau_p \ll \frac{2h\nu\beta L}{\sigma_{abs}} \tag{10}$$

12

In Eq. 10, *L* is the sample length. The 10 ps pulse width NLA experiments in this work do not satisfy this condition for either the Ge or GaSb sample, which would require $\tau_p \ll 45$ fs. The fact that the pulses were too long to isolate β was evident in the simultaneous β and σ fits shown in this study.

Unlike β, free carrier effects can be affected by the material doping level, as a greater level of initial carriers will induce more absorption and refraction. TPA and FCA both contribute to nonlinear absorption. Because of this it can be difficult to isolate their parameters, and a code has been developed in this work to extract the parameters from data that is collected at the same wavelength but two different pulse widths.

Free carrier lifetime τ_R (s)

Excited electron-hole pairs eventually recombine, and the total free carrier recombination lifetime τ_R can be calculated from the inverse Auger recombination rate, radiative recombination rate and Shockley-Read-Hall (SRH) recombination rate. Each of these recombination rates is dependent on free carrier density. Free carrier lifetimes could be measured with a pump-probe technique [20], but lifetimes are well understood and will not be experimentally obtained.

Intrinsic free carrier density N_0 (cm^{-3})

The intrinsic free carrier density indicates the number of free carriers present when the material is in equilibrium. This parameter is material dependent and can be altered by doping the material with other elements. In this work, N_0 is neglected as it is measured to be orders of magnitude less than the generated free carrier density.

13

Generated free carrier density N (cm^{-3})

N indicates the free carrier density generated when the material is illuminated with an optical wave. Carriers are generated by linear or nonlinear absorption according to Eq. 2. If the number of generated free carriers exceeds 1% or 10% of total valence electrons, material bond softening or ablation (respectively) may result [19]. This generally only occurs for high-irradiance fs pulse widths. In Ge, the atomic density is 4.4×10^{22} atoms/cm^3 and there are four valence electrons per atom, so a generated free carrier density at of least $\sim 10^{22}$ cm^{-3} would be required to see this effect. At the irradiances used in this work, the maximum free carrier density is 10^{20} cm^{-3} so material bond softening or ablation is not expected.

Temperature T (K)

Temperature rise due to NLA from a single-pulse can be sufficient to melt the surface of a sample, which is modeled and measured in this work. Lattice expansion due to temperature rise can alter linear absorption, β, bandgap and N.

Linear or one-photon absorption α (cm^{-1})

If the photon energy is smaller than the bandgap of the material, there minimal interaction with the lattice and α is negligible in comparison to β and σ [21]. However, α can rise exponentially as the material is heated past 350-400 K, leading to a *thermal runaway* effect that is explored in this work.

Nonlinear refraction

Refraction can be induced in a material from nonlinear refraction (n_2), thermal lensing (dn/dT) or free carrier refraction (σ_{FCR}), based on instantaneous, thermal or cumulative effects, respectively. Refraction could focus or defocus the beam, varying the

irradiance within the material and therefore the level of nonlinear absorption. However, modeling is performed in Chapter 3 to show that these phenomena will not affect the test conditions in this work.

Literature search – NLA studies for Ge and GaSb

Prior Ge and GaSb nonlinear studies in the literature are now reviewed, and four studies for Ge shown in Table 3. NLA at 2.05 μm or 2.5 μm is studied in this work, and the nearest literature wavelengths were 2.36 μm and 2.6 μm, but those studies did not account for free-carrier absorption. The next closest study occurred at 2.8 μm, which according to theory [24] should have one-third the TPA of 2.5 μm photons in Ge.

Table 3. Survey of nonlinear studies for germanium, ordered by wavelength

λ (nm)	Pulse width	TPA (β) cm/GW	FCA (σ) cm^2	Dopant level (cm^{-3})	Reference
2360	not given	1000	-	not given	[28] Zubov 1969
2600-3100	100 ns	2500	-	not given	[29] Wenzel 1973
2650	480 ns	680	-	n $\sim10^{15}$-10^{16}	[30] Gibson 1976 Fig. 8
2800	480 ns	325	-	n $\sim10^{15}$-10^{16}	[30] Gibson 1976 Fig. 8
2900	2 ps	80±10	*6±1x10^{-17}	not given	[31] Rauscher 1997
2950	480 ns	100	-	n $\sim10^{15}$-10^{16}	[30] Gibson 1976 Fig. 8
3000	2 ps	20±5	*6±1x10^{-17}	not given	[31] Rauscher 1997

* non-degenerate value measured using a 2.9 μm pump and a 3 μm probe

GaSb is far less studied, and there is only one paper where two-photon absorption was measured. In a 1996 work, Akmanov [32] used an estimated $\sigma = 2x10^{-17}$ cm^2 to measure $\beta = 380$ cm/GW in GaSb at 2.94 μm. At 2.05 μm, a β of 156 cm/GW was reported as a theoretical calculation [33].

15

Serious errors can occur if FCA is neglected, as shown in a 1973 study where NLA was observed in 5.1 mm thick uncoated germanium [29]. The laser output covered a spectrum from 2.6-3.1 μm, pulse width was 100 ns, and peak irradiances ranged from 1-10 MW/cm^2. FCA was not used, and β alone was used to fit the transmission, resulting in $\beta = 2500$ cm/GW for the data shown in Figure 7. The same transmission can be fit using the finite difference model developed later in this chapter and actual NLA values measured from this work. After scaling for wavelength, $\beta = 30$ cm/GW and $\sigma = 8 \times 10^{-16}$ cm^2 fit the data well, highlighting the need for a simultaneous β and σ measurement technique.
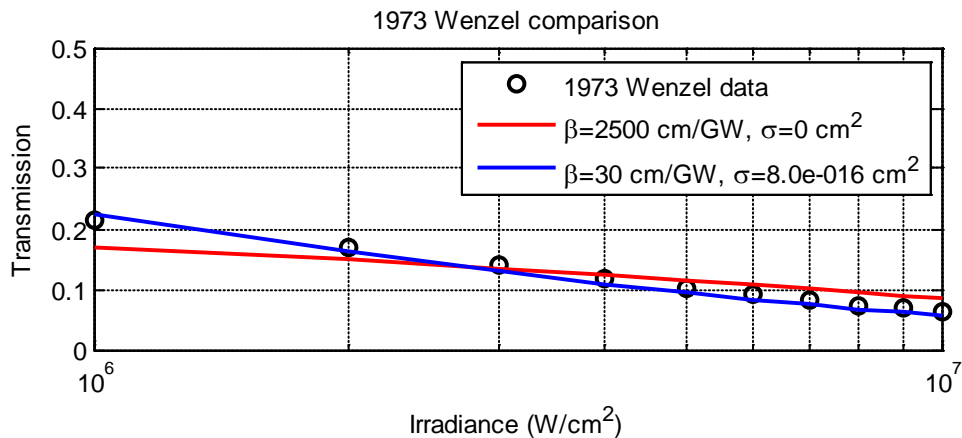
Figure 7. Finite difference model applied to data from [29], showing that nonlinear transmission data can be fit with widely varying β and σ values.

Laser-Induced Damage Study

As mid-IR laser development progresses, the ability of these lasers to dazzle or damage IR sensors must be assessed. In this section the material properties that contribute to laser-induced damage are described, timescale-dependent phenomena are

16

presented, and experimental guidance is examined. Finally, the literature is reviewed for prior damage studies in Ge and GaSb.

A reported value of in-band pulse energy required to damage an EO sensor is 50-250 mJ at typical combat ranges, although the pulse width was unspecified [7]. Figure 8 presents two examples of laser-induced damage to EO sensors.

No damage   Damage

a   b
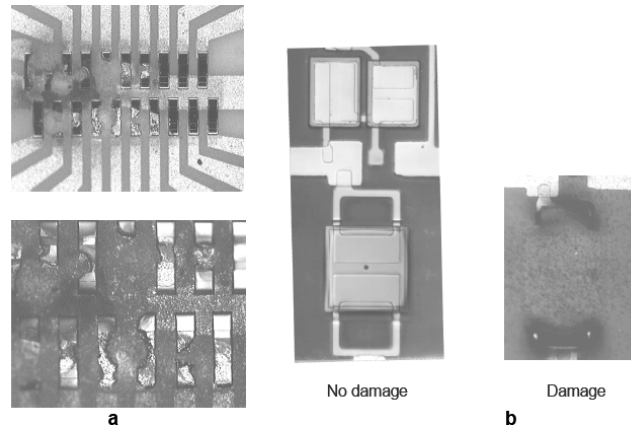
Figure 8. Laser damage in (a) HgCdTe detector and (b) Silicon microbolometer [7]

Laser-induced damage depends on numerous factors including pulse width, irradiance and wavelength, and it is much easier to damage a sensor if the radiation is in-band for the sensor, as filtering is unlikely at those wavelengths. The pulse width dependence is clearly shown in this work, as the high peak irradiances in the ps pulses resulted in damage at µJ levels while ns pulses required mJ pulse energies.

Timescale-dependent laser damage mechanisms

The laser-induced damage threshold (LIDT) is determined by many simultaneous processes operating on timescales that vary widely. This section describes the mechanisms that dominate when the timescale of the incident radiation is varied from

17

continuous wave (CW) to ultrashort fs pulse widths. Material properties that can affect damage thresholds include reflectivity, linear and non-linear absorption, density, thermal conductivity, specific heat and melting temperature. Material failure modes can include crack formation, melting, buckling, ablation or exceeding the critical temperature of electronics.

CW damage mechanisms: At CW or long pulse widths on the order of one second, the damage threshold is mainly determined by the thermal conductivity of the sample [8]. For CW illumination, as laser radiation couples into the material, a thermo-mechanical signal is propagated, which will affect different materials in different ways, including thermal, mechanical and nonlinear effects. Thermal effects can include loss of strength, melting, pyrolysis, ablation, vaporization, ignition, deflagration or detonation. Mechanical response can include thermal-mechanical stresses and also pressure shock waves. Finally, nonlinear responses can include absorption, self-focusing, and generation of hot electrons, x-rays or THz electromagnetic pulses [34].

μs to ps pulse damage mechanisms: For μs pulse widths, the threshold fluence (J/cm^2) is mainly determined by linear absorption, material heat capacity, free-carrier diffusivity and thermal diffusivity [35]. The dominant damage mechanism is thermal melting, and the pulse width and laser spot size will determine if free-carrier or thermal diffusion will reduce the LIDT.

fs-pulse damage mechanisms: The mechanisms that affect damage at fs scale are very different than longer pulses, transitioning from thermal mechanisms to dielectric breakdown. The extreme level of peak irradiance resulting from the ultra-short pulse duration can cause the energy to be deposited faster than free carriers can relax into

phonons [19]. Mechanisms of damage vary depending on what percentage of excited carriers are generated, as a percent of valence electrons. At <1% excitation, damage is due to excitation of coherent phonons. At ~1% excitation, damage occurs as a result of bond softening, and at ~10% excitation it is due to non-thermal ablation [19].

The transition between thermal mechanisms and dielectric breakdown can be described by two methods. The first method states that dielectric breakdown can occur when τ_p becomes shorter than the phonon relaxation time, which for example is 0.1 to 0.5 ps in silicon [36]. Keldysh theory [37] is the second method, and is widely discussed in the fs damage literature to predict the transition between dielectric breakdown and thermal damage mechanisms [19,38,39]. The Keldysh parameter γ is the ratio of the incident electric field frequency to the tunneling frequency, and the $\gamma = 1$ case is the dividing line between the classical and quantum regimes [40]. When $\gamma << 1$, damage is dominated by dielectric breakdown, which primarily results from Zener tunneling between Bloch bands. When $\gamma >> 1$, damage is dominated by thermal mechanisms that result from photoionization, including TPA.

γ is defined in Eq. 11 where ω is the optical frequency, ω_t is the tunneling frequency, I_p is the ionizing potential (eV), U_p is the ponderomotive energy (eV), I is irradiance (PW/cm^2) and λ is wavelength (nm) [41]:

$$\gamma = \frac{\omega}{\omega_t} = \sqrt{\frac{I_p}{2U_p}} \quad \text{where} \quad U_p = 9.337x10^{-5} * I\lambda^2 \tag{11}$$

19

In Chapter 5, the Keldysh parameter is calculated for the actual test conditions, using an ionizing potential of 5.03 eV for GaSb [42] and 7.86 eV for Ge [43]. If the peak irradiance is sufficient at a fs pulse width, electrons are ripped away and the resulting positively charged atom undergoes a Coulomb explosion, resulting in non-thermal ablation. This effect is especially useful in laser machining, where molten residue is undesirable.

Experimental guidance

A valuable resource for designing damage test experiments is ISO standard 11254-1, which governs single-shot laser-induced damage testing [44].   It defines the damage threshold as "*the highest quantity of laser radiation incident upon the optical surface for which the extrapolated probability of damage is zero*". An example of this method is shown in Figure 9 where the resulting fluence threshold is circled in red.

Beam diameter on-sample is recommended to be > 800 μm for pulses shorter than 100 ns and > 200 μm for longer pulses, with spacing between sites of 1.25-5 times the beam diameter. Pre-test sample cleaning consists of a four step process by cleaning the sample with acetone, then methanol, then de-ionized water and finally the surface is dried with N_2 gas. The standard specifies a minimum test plan, where ten sites per fluence are required and a minimum total of 75 sites. Finally, damage is defined as any permanent surface modification visible with a Nomarski-type differential interference microscope.

20
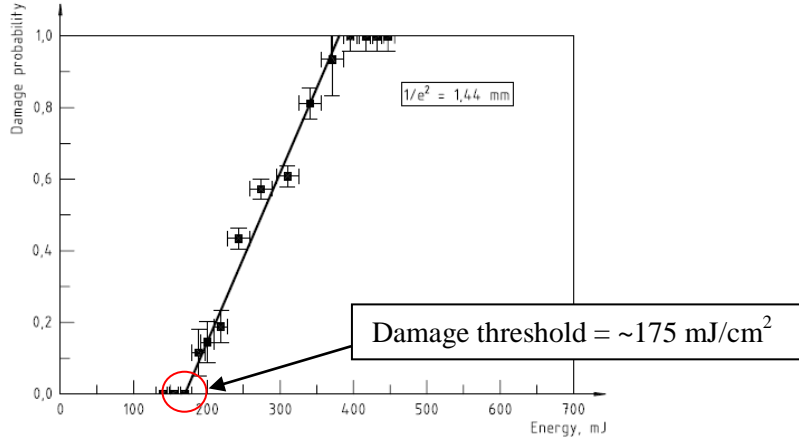
Figure 9. Extrapolation method of determining damage threshold [44]

Literature search – damage studies for Ge and GaSb

There were no damage studies found in the literature for GaSb, and two Ge

studies are reported in Table 4. The 250 nm study occurs in the linear absorption regime,

and the only test where TPA is the dominant damage mechanism is the 2.8 μm study by

Seo *et. al.* Additionally, the 2.8-5.2 μm tests were conducted on the Vanderbilt free-

electron laser, which is a 10,000 shot test, not a single shot test as performed in this work.

Table 4. Survey of damage studies for germanium

λ (μm)	Pulse width	LIDT (J/cm^2)	Dopant level (cm^{-3})	Beam spot radius (μm)	Reference
0.25	38 ns	**0.327**	p ~10^{17}	1500	[45] Jellison 1986
2.8	5 μs FEL[1]	**5.3**	n = 10^{13}-10^{14}	260-380	[46] Seo 2008
3.2	5 μs FEL[1]	**12.8**	same	260-380	[46] Seo 2008
3.6	5 μs FEL[1]	**21.5**	same	260-380	[46] Seo 2008
4.0	5 μs FEL[1]	**22.5**	same	260-380	[46] Seo 2008
4.4	5 μs FEL[1]	**26**	same	260-380	[46] Seo 2008
4.8	5 μs FEL[1]	**24.8**	same	260-380	[46] Seo 2008
5.2	5 μs FEL[1]	**22.8**	same	260-380	[46] Seo 2008

[1] Free electron laser – 30 Hz, 5 μs length macro pulse consisting of 10,000 1 ps micro pulses.

21

Finite Difference Model

Significant effort went into the development and verification of a single-pulse finite difference (FD) model, which was used extensively in this work for NLA design of experiments, measurement of nonlinear absorption coefficients and to model temperature rise resulting in laser-induced damage. In this section the modeling method and assumptions are presented and a comparison is made to a simplified analytic solution. Then, additional rate equations are coupled into the model and parameter behavior is explored. Finally, model verification is performed and the modeling of a non-Gaussian pulse is described.

The model incorporates Eq. 1-3 presented previously on page 7 for optical absorption, free carrier density and temperature rise [21]. Additionally, free-carrier density dependent recombination $\tau_R(N)$ in Eq. 12 and temperature dependent linear absorption $\alpha(T)$ in Eq. 13 are implemented for each element in radius (r), position (z), time (t) and temperature (T):

$$\frac{1}{\tau_R} = B_{radiative} * N(r, z, t) + C_{auger} * N(r, z, t)^2 \tag{12}$$

$$\alpha = \alpha\{T(r, z, t)\} \tag{13}$$

Previously, the temperature rate equation was a diagnostic and did not affect irradiance and free carrier density. Now, the inclusion of $\alpha(T)$ has the effect of coupling temperature (Eq. 3) into the irradiance and free carrier equations (Eq. 1-2), resulting in higher accuracy.

22

Several assumptions are made with the model:

- The incident beam has radial symmetry and contains quasi-monochromatic light
- The sample is thin compared to the beam confocal parameter, resulting in negligible diffraction while traversing the sample, and nonlinear refraction is insignificant
- The sample is of sufficient purity that the intrinsic carrier density N_0 is insignificant in comparison to the generated free carrier density
- The slowly varying envelope and paraxial approximations can be applied
- Three-photon (and higher) absorption and tunneling ionization are insignificant
- The temperature dependence of β, σ and τR are insignificant
- The combination of pulse width, spot radius (r_o) and pulse repetition frequency (PRF) are chosen to avoid both free-carrier diffusion and thermal diffusion
- The peak pulse irradiances are low enough to avoid dielectric breakdown

Analytic solution

While the full set of coupled nonlinear partial differential equations can only be solved numerically, the first equation can be solved analytically if the following assumptions are made in addition to those listed above:

- The pulse has Gaussian profiles in time and space: $I(r,t) = I_0 e^{-\left(\frac{r}{r_o}\right)^2} e^{-\left(\frac{t}{t_o}\right)^2}$
- There is no linear absorption ($\alpha = 0$)
- Fresnel losses at surfaces are ignored
- The pulse width is short enough that FCA is insignificant compared TPA. As described previously, this condition is $\tau_p \ll \frac{2h\nu\beta L}{\sigma_{abs}}$ [27]

If a dimensionless parameter Q is defined as $Q = \beta I_o L$, (L is sample length) then an analytic solution for transmission (T) can be derived as Eq. 14 [47] and is graphed as a function of Q in Figure 10:

$$T = \frac{1}{\sqrt{\pi}Q} \int_{-\infty}^{\infty} ln\left[1 + Qe^{-\left(\frac{t}{t_o}\right)^2}\right] dt \qquad (14)$$

23
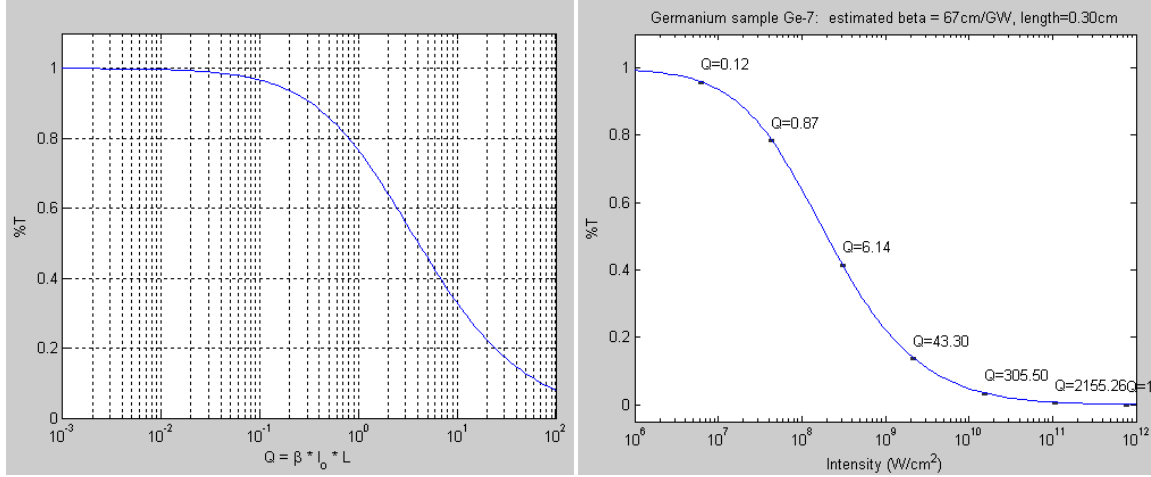
Figure 10. (left) Nonlinear transmission vs. *Q* parameter. (right) Ge sample theoretical transmission vs. peak pulse irradiance with *Q* overlay

Finite difference treatment of coupled nonlinear differential equations

An implicit finite difference (FD) numerical method was used to solve the coupled nonlinear differential equations in Eq. 1-3 and Eq. 12-13, and was used both to extract nonlinear absorption coefficients and to model temperature rise resulting in laser-induced damage. An explicit solution solves the equations as only a function of the current state (*z* or *t*), while an implicit form solves the equation as a function of both the current system state (*z* or *t*) and the state after one step (*z+1* or *t+1*). The implicit form is the proper numerical method and leads to increased accuracy and stable results. Eq. 15 results when Eq. 1 is expressed as an implicit finite difference, and is solved as quadratic equation in Eq. 16:

$$\frac{I_{z+1} - I_z}{\Delta z} = -\alpha I_{z+1} - \beta I^2_{z+1} - \sigma N I_{z+1} \tag{15}$$

$$0 = -I_z + [1 + \Delta z(\alpha + \sigma N)]I_{z+1} + \Delta z \beta I^2_{z+1} \tag{16}$$

24

In a similar fashion, the generated free-carrier density and temperature equations are implicitly solved to yield Eq. 17-18:

$$N_{t+1} = \left(\frac{1}{1 + \Delta t / \tau_R}\right)\left[N_t + \Delta t \left(\frac{\alpha I}{h\nu} + \frac{\beta I^2}{2h\nu}\right)\right] \tag{17}$$

$$T_{t+1} = \frac{\Delta t}{\rho C}(\sigma N I + \alpha I + \beta I^2) \tag{18}$$

The pulse profile in time and space is modeled beyond the typical $1/e$ or FWHM level. In Figure 11 (left), half of a Gaussian pulse is shown with a $1/e$ spatial and temporal profile denoted by a semi-transparent aqua surface intersecting the pulse shape. Some energy would be lost if the effects below this level are ignored, so the limits of integration are extended to include pulse time and radii where $I = 0.005 * I_o$ in order to improve accuracy.

In the FD model, the pulse and sample are broken up into elements in time, sample radius and sample length as shown in Figure 11 (right). Radial symmetry is assumed, and for each radial slice the differential equations are applied to each element, whose output is fed to the next element on the z-axis until the sample end.
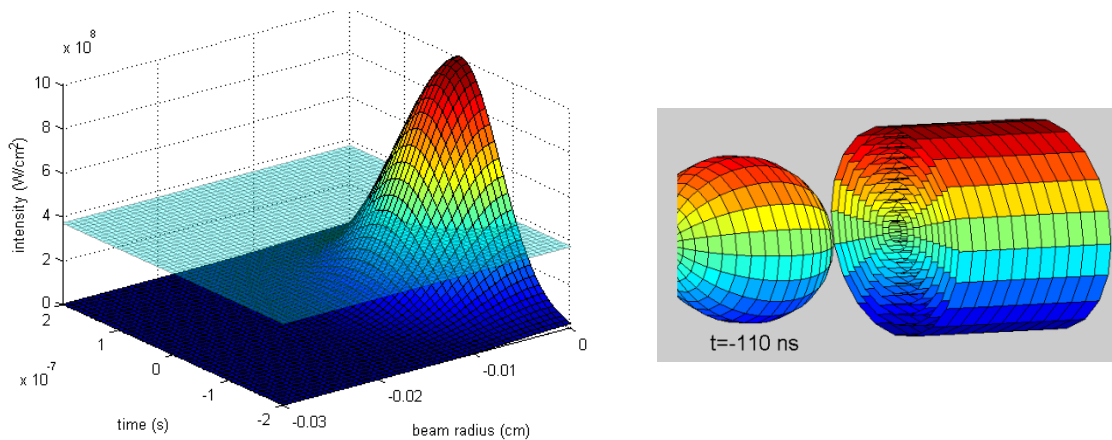
**Figure 11. (left) 100 ns Gaussian pulse shape highlighting 1/e intensity profile.
(right) the FD model divisions are shown for the pulse (sphere) and sample (cylinder)**

25

The loop structure is presented below:

- Start with a Gaussian pulse and a defined sample length, sample radius and input pulse energy (E_{in})
- Loop 1: for each radial element…
    - o Loop 2: for each time relative to the pulse center…
        - ▪ Loop 3: for each z-axis position…
            - • Find irradiance according to the Gaussian profile, which varies with radius and time relative to pulse center
            - • This irradiance is presented to the crystal face
            - • Irradiance attenuation, free-carrier variation and temperature variation are computed for that element.
            - • The resulting irradiance is presented to the next element in z
            - • During Loop 3, N and T arrays are maintained to propagate cumulative effects to the next time step in Loop 2
        - ▪ Loop 3 is repeated for each z-axis position
    - o Loop 2 is repeated for each time relative to the pulse center
- Loop 1 is repeated for each radial element

During Loop 2, for a single radial element, the resulting irradiances are integrated over time to calculate the resulting transmitted fluence for that radial element. At the end of Loop 1, the resulting fluences from each radial element are integrated to determine the exiting pulse energy (E_{out}). Finally, the transmittance is calculated as E_{out}/E_{in}.

Addition of free carriers and temperature

The next step is to couple in the free carrier absorption and temperature equations. The free carrier absorption equation will result in greater absorption, while the temperature equation is a diagnostic and does not affect absorption unless temperature dependent linear absorption is implemented.

The influence of free carrier relaxation time on free carrier density is now investigated. In the top graph of Figure 12, N follows the irradiance profile of the pulse as the τ_R of 10 ns is shorter than the example pulse width of 100 ns. On the bottom graph,

26

www.manaraa.com

$\tau_R = 1000$ ns and N remains elevated even after the irradiance has decreased, as there is insufficient time for the free carriers to recombine during the pulse.
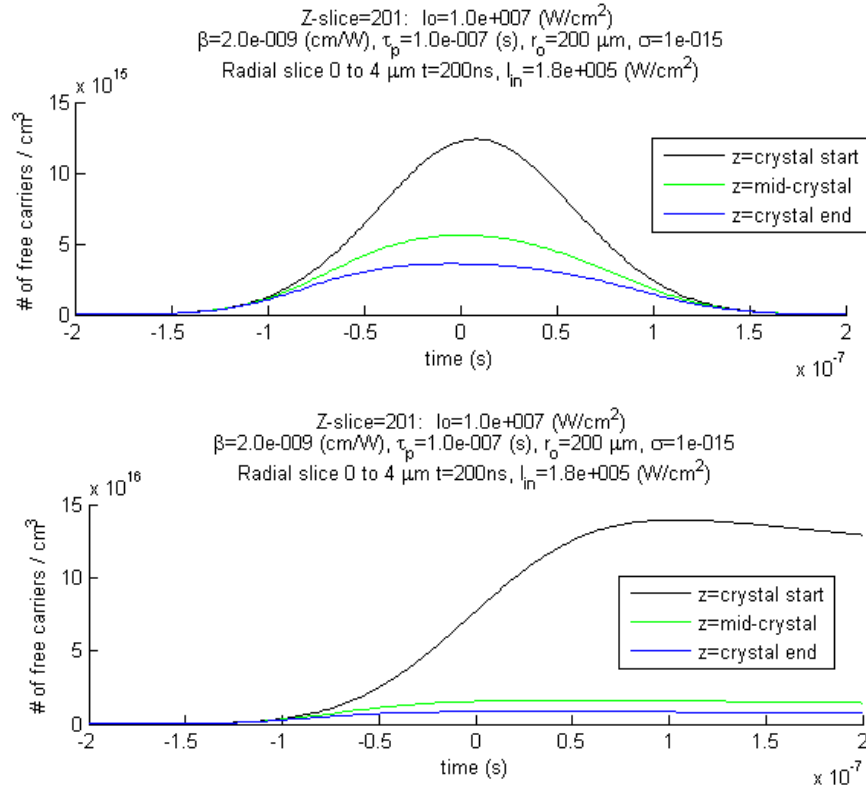
Figure 12. Behavior of free carrier density within the timeframe of the incident 100 ns pulse. Multiple curves are different points in the crystal: black = start, green = middle, and blue = end. (top) free carrier relaxation time is fast at 10 ns. (bottom) free carrier relaxation time is slow at 1000 ns

By saving a time history of all radii and z data, distributions of irradiance or free carrier density can be created, as shown in Figure 13. This illustrates that the highest N and T variation occurs in a shallow skin depth and also proved helpful during model development for troubleshooting.

27
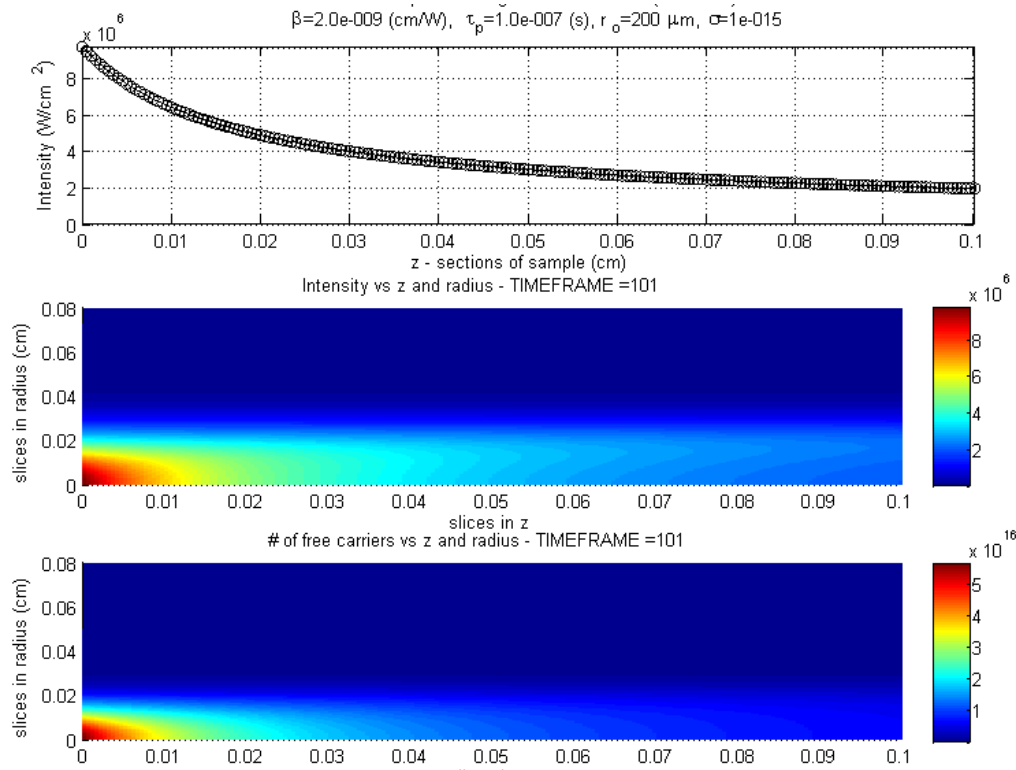
Figure 13. Irradiance of on-axis radial element (top), Irradiance vs. radius (middle), and free carrier density (bottom) as a function of *z* location within a 0.1 cm sample length.

An advantage of the numerical method is that a non-Gaussian temporal pulse can be used. This allows the accurate modeling of nonlinear parameters even if the input pulse has a unusual time profile, which is typical of Cr^{2+}:ZnSe gain-switched lasers [48,49] as shown in Figure 25 on page 45.

Fresnel reflections are modeled, whose resulting linear transmission can be obtained from a spectrophotometer or FTIR measurement. If the sample is 70% transmissive (*T*), the 30% loss occurs from Fresnel reflections from the two faces of the crystal, as it is assumed that linear absorption does not occur for sub-bandgap photon energies. The first Fresnel reflection reduces the irradiance presented to the crystal face by a factor of 1-$\sqrt{T}$ or 16%, which then lowers the irradiance within the sample and

28

results in reduced nonlinear absorption. At the exit face, transmission is reduced by another $1-\sqrt{T}$ factor, which results in 70% total transmission if no absorption has taken place. The reflection from the back face is assumed to be scattered within the sample and will be small enough to not affect nonlinear properties, as a significant portion (up to 90%) has already been absorbed.

In Figure 14, model output for ten pulse widths is presented where linear transmission is set to 100%. The limit on the left-hand side (towards 1 μs τ_p) occurs due to the free carrier lifetime τ_R of 100 ns. At this limit, $\tau_R \ll \tau_p$ and further variation of τ_R no longer affects the nonlinear absorption. The right side of Figure 14 (towards 1 fs τ_p) shows that the influence of FCA drops off when $\tau_p \ll \frac{2h\nu\beta L}{\sigma_{abs}}$, as predicted [27]. At this limit, the dominant absorption effect is β and the transmission curve becomes independent of further reductions in τ_p.
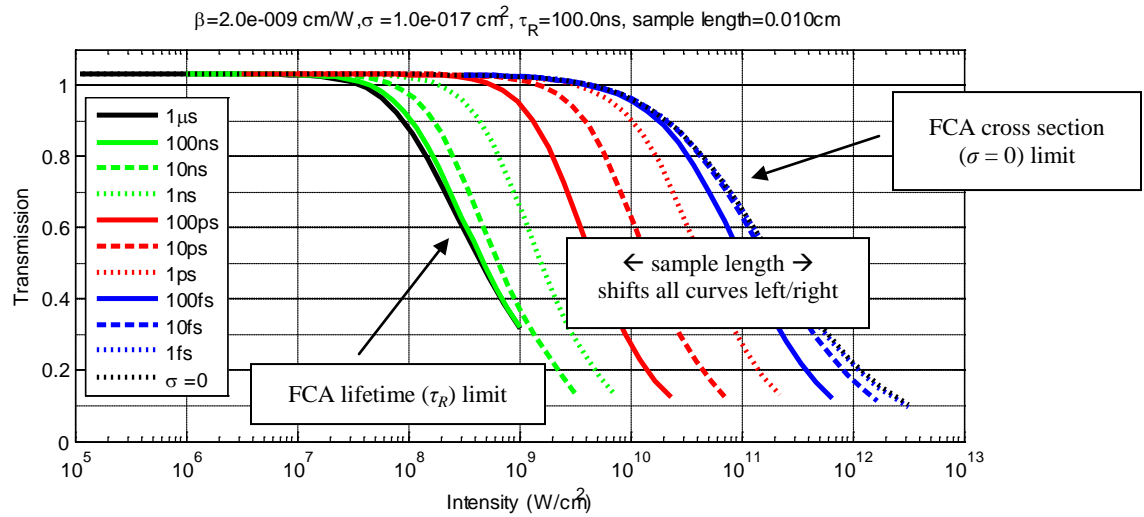
Figure 14. Theoretical nonlinear transmission as a function of irradiance and pulse width, including TPA and FCA

29

Model accuracy can be improved by increasing the number of steps (divisions) in time, radius and z position. However, there is a point where increased simulation time is not worth the extra accuracy gained. Figure 15 shows that accuracy within half of a percent can be achieved with 350 divisions, which is the value used in all modeling performed. Each simulation takes about 20 seconds in this case.
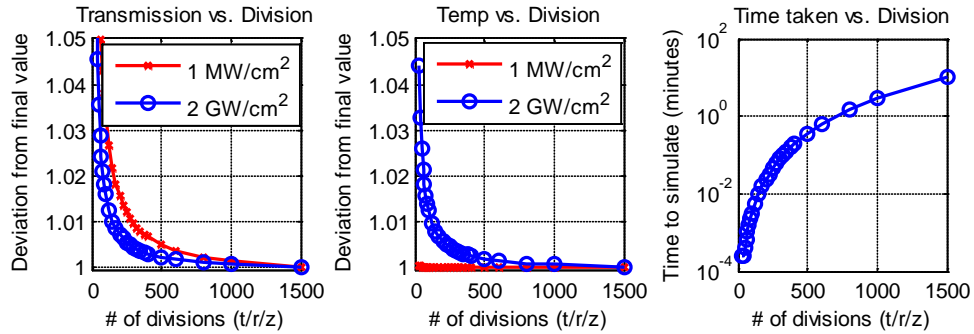
Figure 15. Accuracy improvement by increasing the model fidelity. Left is transmission, middle is temperature and right is the simulation time

Model verification

Extensive verification of the FD model was performed. First, the analytic model was compared to a simplified version of the finite difference model. As required by the analytic model, the models are both set to exclude Fresnel losses, linear absorption and free carrier absorption. In this comparison, the sample was broken up into 500 length, radii and pulse sections, and a maximum 0.5% relative error was found.

The accuracy of modeling α was verified when studying irradiance-dependent bleaching in a Cr^{2+}:ZnSe sample. Low irradiance transmission was predicted by $\%T = e^{-\alpha z} = 37.8\%$ for the sample, which matched spectrophotometer measurements. The model predicted $\%T = 37.9\%$ in this case.

30

Verifying the model with σ present was accomplished by comparing the results over ten different pulse widths (Figure 16) with the AFRL/RXPJ model (Figure 4 on page 9), and a match was achieved.
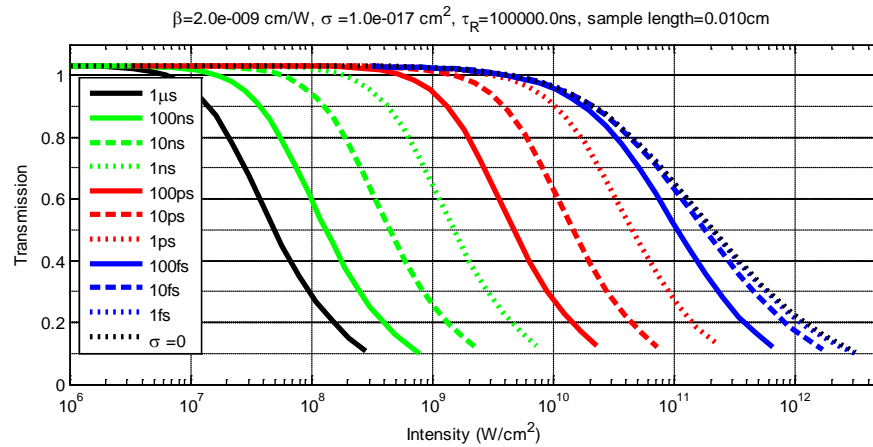
Figure 16. Comparison graph to prior work: theoretical nonlinear transmission as a function of irradiance and pulse width

Finally, 28 comparison cases between the present work and [51] were accomplished with varying levels of α, β, σ, Fresnel reflections and τ_R. Excellent agreement was achieved in the resulting peak free carrier density, peak on-axis temperature rise and energy transmission through the sample for each case. The author again thanks the AFRL/RXPJ team for frequent assistance.

Modeling 2.5 µm gain-switched pulses

The development of a Cr^{2+}:ZnSe gain-switched laser will be described in Chapter 3, whose pulses possess a non-Gaussian temporal profile. The modeling of these pulses is performed in this section for incorporation into the finite difference model.

For the nonlinear absorption tests, the laser output was fixed at 1.5 mJ. The repeatable 1.5 mJ temporal profile that is loaded into the FD model is shown in Figure 17 (left). For comparison, an equivalent 1.5 mJ Gaussian pulse is fit to the gain-switched pulse which resulted in an admittedly poor best fit of 68 ns pulse half width. It is shown that the peak irradiance of the gain-switched pulse is much greater than an equivalent Gaussian.
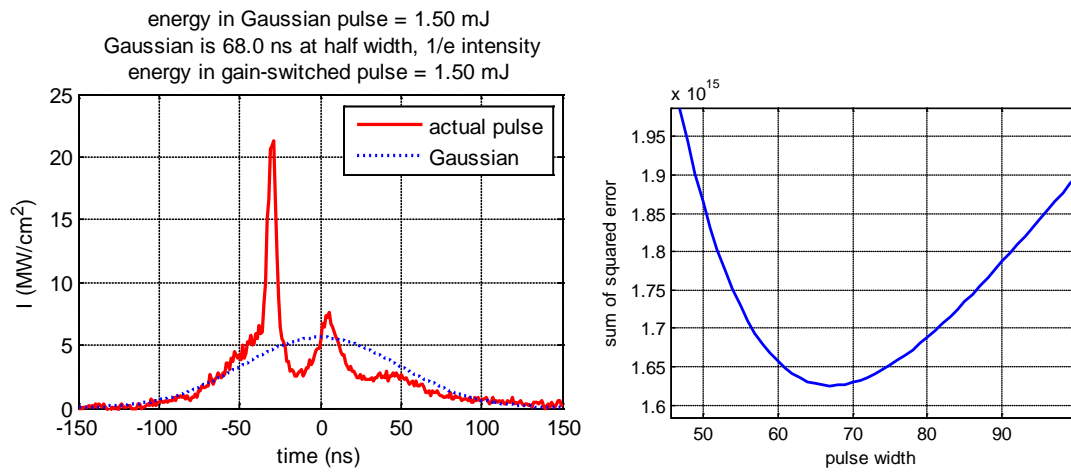
Figure 17. (left) gain-switched pulse with Gaussian best fit overlay, (right) sum of squared error variation with Gaussian pulse width, showing 68 ns best fit

The pulse energy in a non-Gaussian pulse can be expressed as $E = Area \int Idt$, or alternatively $E = Area_{spot} \sum(I_i * \tau)$ where τ is the oscilloscope time step of 0.2 ns. The irradiance profile I_i can be determined by multiplying the oscilloscope voltage trace V_i by a constant M, and varying that constant until $1.5 \text{ mJ} = Area_{spot} \sum(V_i M * \tau)$. Using this method and a 265 μm spot radius, the peak irradiance was calculated as 22.3 MW/cm^2, as shown in Figure 17. The peak

irradiance and pulse energy vary linearly with the scaling factor, for example a 10x reduction in scaling factor gives a peak irradiance of 2.2 MW/cm^2 and E=0.15 mJ.

The peak irradiance is much higher than an equivalent Gaussian pulse and the effect is now explored. This increase in peak irradiance increases the nonlinear absorption of the pulse when compared to an equivalent Gaussian. A comparison is given in Figure 18, where the FD model was modified to load this scope trace and the scaling factor was used to vary the incident pulse energy.

Ge: β=81 cm/GW, σ=1.04e-016 cm^{-2}, B$_{rad}$=6.4e-014 cm^3/s, Auger=2.0e-031 cm^6/s λ=2.50 μm
Gaussian pulse: τ_p=68.0 ns, 1/e spot radius=265 μm, linear %T=90.0
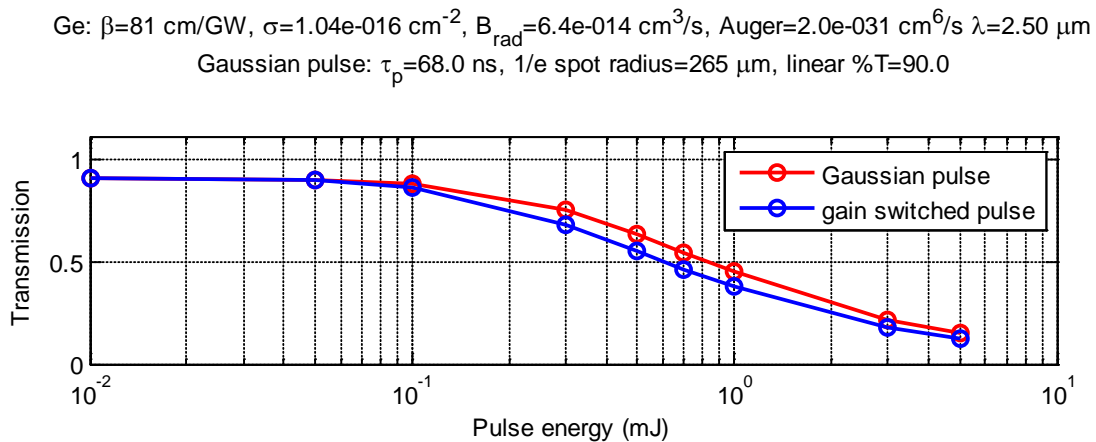
Figure 18. Comparison of transmission from Gaussian pulses (red) and gain-switched pulses (blue) of identical pulse energy

The difference is highlighted in Table 5, where the higher peak irradiance decreases the transmission, increases the generated free carrier density and increases the temperature rise in comparison to an equivalent gain-switched pulse. Ge melts at 1210 K, which is a temperature rise of 937 K above room temperature. For this scenario, a 5 mJ gain-switched pulse would melt the surface of the sample while an equivalent Gaussian pulse would not.

33

Table 5. Comparison of transmission, generated free carrier density and temperature rise from Gaussian pulses and gain-switched pulses in Ge

Incident energy (mJ)	Gaussian pulse			Gain-switched pulse		
	Transmission (%)	Free carriers ΔN (cm^{-3})	Temp rise ΔT (K)	Transmission (%)	Free carriers ΔN (cm^{-3})	Temp rise ΔT (K)
0.01	90	5.5×10^{13}	0	90	9.4×10^{13}	0
0.05	89.9	1.4×10^{15}	0	89.5	2.4×10^{15}	0
0.1	87.9	5.5×10^{15}	0.01	85.9	9.4×10^{15}	0.02
0.5	63.2	1.4×10^{17}	0.9	54.8	2.3×10^{17}	1.8
1	44.9	5.5×10^{17}	7	37.5	9.1×10^{18}	14
5	14.8	4.5×10^{18}	649	12.0	4.7×10^{18}	945

34

Chapter 3.　　　Method

This chapter contains the calculations, analysis and design work that supports the nonlinear absorption and damage threshold results achieved in Chapter 4. Two nanosecond laser sources are described which were required to complete the NLA and damage test plans: a 2.5 μm laser source was developed; and modifications to a 2.05 μm laser are documented. Additionally, the semiconductor samples are characterized and calculations are performed to support development of the nonlinear absorption and damage test plans.

Gain-switched laser

A 2.5 μm nanosecond laser source was required for testing, and a gain-switched Cr^{2+}:ZnSe laser was created whose peak power exceeds all designs reported to date by a factor of eight. In this section the aspects of the lasing active ion and host material that apply to gain-switched laser development are discussed. Additionally, the pump laser, gain-switched cavity design and laser output are described, including slope efficiency and pulse width variation for different outcouplers.

Material Properties

Divalent chromium (Cr^{2+}) is a group 6 transition metal (TM) and was selected as the lasing transition ion because of its broad tunability in ZnSe from 1.9 μm to 3.1 μm [52]. In 1995, tunable mid-IR lasing at room temperature from Cr^{2+} ions was first achieved [53,54]. Benefits of Cr^{2+}:ZnSe lasers include room-temperature operation, up to 70% conversion efficiency [4], pure CW power up to 14 W [56] and pulsed average power up to 18.5 W [49]. Transitions to nearby excited states are spin forbidden, which

35

gives this gain medium advantages over earlier TM lasers such as Co^{2+} and Ni^{2+} [57,58].

Additionally, at room-temperature, Cr^{2+}:ZnSe exhibits small nonradiative relaxation, a large gain cross section, no excited state absorption, and finally high thermal conductivity, infrared transparency and quantum efficiency [61].

The energy level diagram that explains the Cr^{2+}:ZnSe mid-IR transition is given in Figure 19 (left), where lasing occurs from the ^5E excited state to the $^5T_2$ ground state.
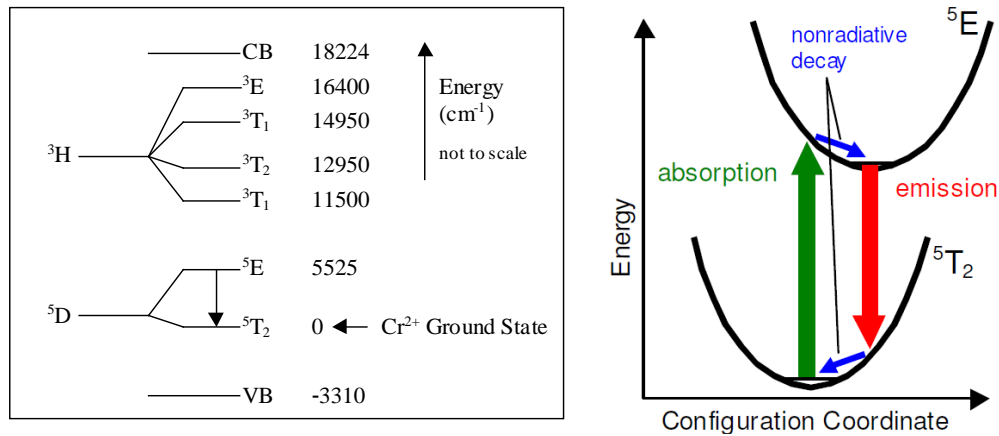
Figure 19. (left) Cr^{2+} Energy levels in Cr^{2+}:ZnSe, (right) Configuration Coordinate diagram explaining four-level behavior from a two-level system [59]

While there are only two levels involved in the lasing transition, Cr^{2+}:ZnSe behaves as it were a four level system due to the offset in configuration coordinate between the energy levels, as shown in Figure 19 (right). This offset, when combined with strong vibrational coupling to the host lattice [60], creates the broad emission and absorption bandwidths that are shown in Figure 20. The broad absorption spectrum allows pumping from a variety of laser sources, including erbium fiber, thulium fiber, Tm,Ho:YLF and finally Cr,Tm,Ho:YAG that is used in this work.

36
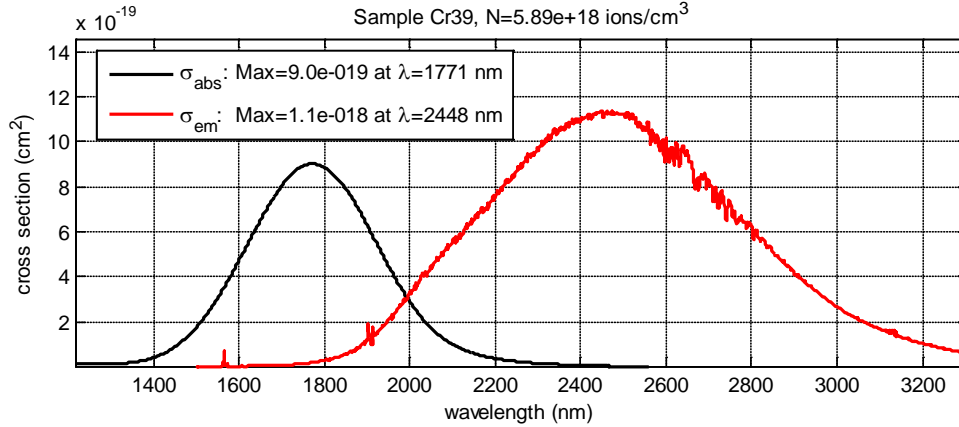
Figure 20. Absorption and emission cross sections of a typical Cr^{2+}:ZnSe sample

Challenges with Cr^{2+}:ZnSe

There are challenges when working with Cr^{2+}:ZnSe because it has a large thermo-optic coefficient (dn/dT) of 70x10^{-6} K^{-1} and short radiative lifetime (τ_{rad}) of ~6 μs [62]. The high dn/dT results in thermal lensing [60] that can lead to cavity instability for CW and high-PRF pulsed laser designs. Additionally, while a long τ_{rad} is desirable for storing energy in the laser gain medium prior to lasing, Cr^{2+} doping levels up to 100-200 parts per million (0.02-0.04% atomic) yield a τ_{rad} of only 6 μs which is orders of magnitude smaller than other ions.

In Cr^{2+}:ZnSe, τ_{rad} decreases at doping levels above 200 ppm (0.04% atomic) due to concentration quenching, which occurs due to an increase in the rate of nonradiative relaxation [63]. In other materials such as Nd:YAG, concentration quenching does not occur until concentrations reach several percent, which is orders of magnitude greater than Cr^{2+} [64]. If techniques such as hot-pressed ceramics [65] can be refined to dope higher ion levels into ZnSe without inducing concentration quenching, longer τ_{rad} at

37

room temperature should be achievable, which will give increased energy storage and performance.

Literature search

In a 2004 review of Cr^{2+}:ZnSe laser development [61], the highest pulse energy obtained at the time was 0.43 mJ. Three other gain-switched lasers have been created during or after 2004, which are shown in Table 6 along with the pulse energy record from the 2004 review.

<div align="center">

Table 6. Cr^{2+}:ZnSe gain-switched lasers

</div>

Pulse energy	Pulse full width	Slope efficiency (%)	PRF (Hz)	Outcoupler (%R)	Reference
0.43 mJ	200 ns	50	10,000	90	McKay 2002 [48]
2.6 mJ	100 ns	65	7,000	30	Carrig 2004 [49]
2.0 mJ	*	3 or 5	*	99.5	Gallian 2006 [65]
14 mJ	120 μs	66	1	66	Koranda 2007 [66]

* not given

Gallian used a hot-pressed ceramic crystal to achieve 2 mJ pulse energy, and Koranda's highest pulse energy of 14 mJ was achieved by pumping with pulses that exceeded the Cr^{2+}:ZnSe radiative lifetime by a factor of 20. Thus, these pulses are over 2,000 times longer than those reported in this work which means the operation was more continuous-wave than gain-switched. Carrig's 2004 work occurred at a high PRF, yielding the current average power record of 18.5 W.

Pump laser

The pump for the gain-switched Cr^{2+}:ZnSe laser is a Schwartz Cr,Tm,Ho:YAG laser which was recently refurbished by R. Shori at UCLA to improve stability and provide 2.095 μm, 13 mJ, TM_{00} spatial profile pulses. The pump's flashlamp driver was set to 3 Hz, 990 V operation and details of the laser include a 67 cm linear cavity, 68% reflective outcoupler, 10° C water temperature and the spinning Q-switch mirror speed was 12,000 rpm.

The pulse width of the Schwartz pump laser was measured as 85 ns FWHM which corresponds to a 55 ns half-width at $1/e$ irradiance. This was measured using a sub-ns rise time Boston Electronics PVM-10 detector and a LeCroy 2 GHz Waverunner 204MXi oscilloscope with 50 Ω coupling. It was possible to align the Schwartz laser to achieve > 17 mJ pulses, but only with a degraded temporal and spatial profile. At higher pulse energies, double or triple pulsing occurred within a 1 μs timescale. Also, the spatial profile became non-Gaussian as an 8-null radial spatial profile was observed near the laser's 74 mJ maximum pulse energy output.

Cavity design

Several interconnected topics are considered in the cavity design, including active ion bleaching, absorption, mode size and damage thresholds. If all possible Cr^{2+} ions are excited during pumping, the material will become transparent as there is no excited state absorption allowed in Cr^{2+}:ZnSe [64]. While this effect is useful for passive Q-switching [67], in this design it is undesirable as it reduces efficiency. The irradiance where bleaching starts to occur is the saturation irradiance (I_{sat}) and was experimentally determined to be ~2 MW/cm^2 for a 2.095 μm pump.

39

For pulsed Cr^{2+}:ZnSe laser design, I_{sat} is the practical concern as it will dictate the optimal mode diameter for the gain-switched laser. To avoid bleaching and for best absorption of the pump, a radius and length of gain crystal was selected to operate at 1-3 MW/cm^2 peak irradiance with ~95% absorption of the pump. This is on the edge of the bleaching curve, where any more pulse energy will reduce efficiency as less % absorption of the pump will occur.

If a Gaussian pulse profile in time and space is assumed, the resulting peak pulse irradiance I from a pulse energy E is derived on page 68 to yield Eq. 19. Eq. 20 solves Eq. 19 so that a radius r_o can be calculated to achieve the desired I of 1-3 MW/cm^2:

$$I = \frac{E}{\sqrt{\pi}\tau_p \pi r_o^2} \qquad\qquad r_o = \sqrt{\frac{E}{I\sqrt{\pi}\tau_p \pi}} \qquad\qquad (19/20)$$

The mode radius r_o that gives 1-3 MW/cm^2 peak irradiance from a range of Schwartz pump pulse energies are represented by the solid lines in Figure 21. Cavity design was guided by this constraint, and also the resulting fluence level from a given pulse energy and spot radius are graphed as dotted lines. A ZnSe LIDT fluence of 2.8 J/cm^2 was reported at a wavelength of 10.6 μm and pulse full width of 100 ns. For 2.095 μm pumping, the damage mechanism in ZnSe would likely be 4-5 photon absorption, not dielectric breakdown as would be the case at a wavelength of 10 μm. However, the threshold should not change significantly, and a value of 2.0 J/cm^2 was selected as the fluence constraint for the cavity. Figure 21 does not include intra-cavity magnification induced by the outcoupler, but the damage constraint should be satisfied as a fluence < 0.5 J/cm^2 results if 1-3 MW/cm^2 peak pulse irradiance is maintained.

40
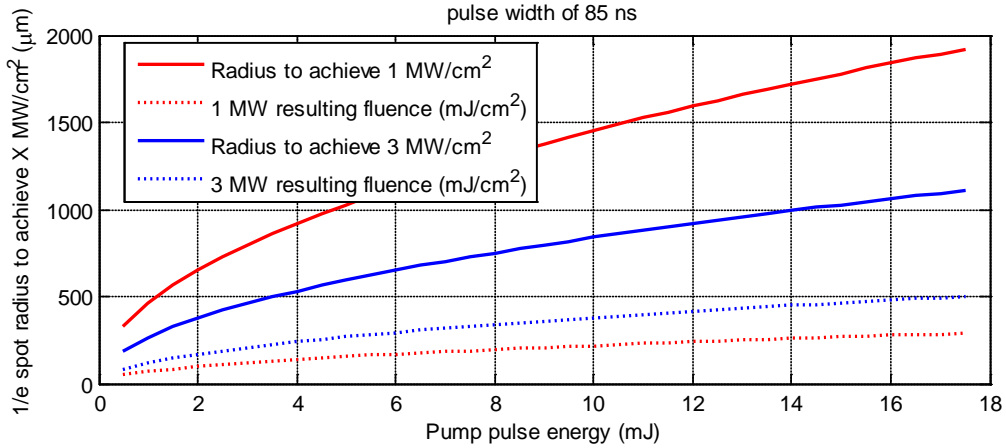
Figure 21. Radius to achieve 1-3 MW/cm² peak irradiance for a range of pump energies (solid lines), resulting fluence level from a given pulse energy and spot radius (dotted lines)

Pump absorption is the next consideration, and the available Cr^{2+}:ZnSe crystal lengths and doping levels were reviewed to find a suitable crystal. The optimum crystal length to achieve 95% absorption for a given α is shown in Figure 22 and is calculated using Eq. 21-23:

$$\frac{I_{out}}{I_{in}} = e^{-\alpha z} \qquad 0.05 = e^{-\alpha z} \qquad z = \frac{-log(0.05)}{\alpha} \qquad (21/22/23)$$
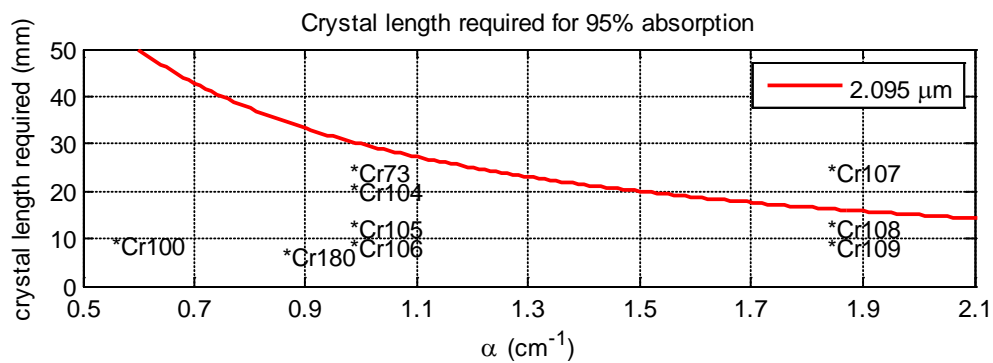
Figure 22. Crystal length required for 95% pump absorption of a 2.095 µm pump. In the figure, CrXXX is the sample identifier

41

There were several uncoated Cr^{2+}:ZnSe crystals that absorb well at this wavelength (Cr73, Cr107, Cr108), however Cr107 and Cr108 can only be placed at normal incidence which would induce intolerable losses within a resonator. The edges of Cr73 are cut at the Brewster angle to eliminate Fresnel losses, which make it the best candidate. This has an added benefit of spreading out the spatial profile on the crystal, which raises its damage threshold when compared to normal incidence. The crystal was purchased from Photonics Innovations, with a specified Cr^{2+} doping level of $N = 7.8 \times 10^{18}$ cm^{-3} and dimensions of 5.3x4.7x24 mm. The path length in the laser cavity is 2.4 cm, giving an acceptable $e^{-0.98*2.4} = 10\%$ T, or 90% absorption.

The minimum entrance dimension of the crystal (Cr073) is 4.7 mm. However, the crystal orientation in the cavity due to its Brewster cut limits the mode diameter to 2 mm, as shown in Figure 23. Another design constraint is that diffraction losses may occur if the clear aperture is less than three times the mode size.

A V cavity was designed with a variable length d_1 to allow the mode size to be adjusted to match I_{sat} for varying levels of pump power. In the cavity design shown in Figure 23 (top right), *M1* is a 50 cm ROC mirror, d_1 is 7.5 cm and d_2 is 15 cm. Figure 23 (top left) shows the LASCAD analysis that predicts a $1/e^2$ mode radius of 600 μm at the planar outcoupler (*o/c*) and 444 μm at the planar *M2* folding mirror. Matching the pump mode to the resonant mode was accomplished by focusing the pump with a one meter focal length lens, and adjusting the lens position for optimum pulse energy. The laser cavity is pictured in Figure 23 (bottom), where the laser output is shown in yellow.

42

1

www.manaraa.com
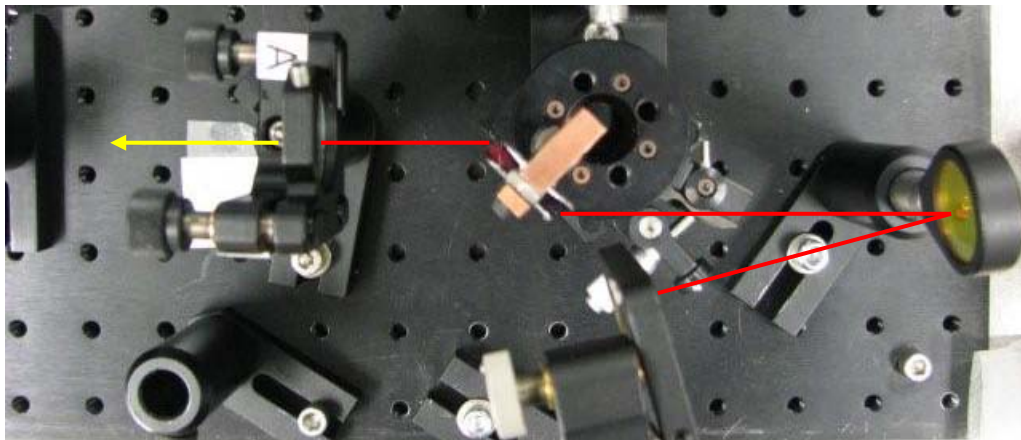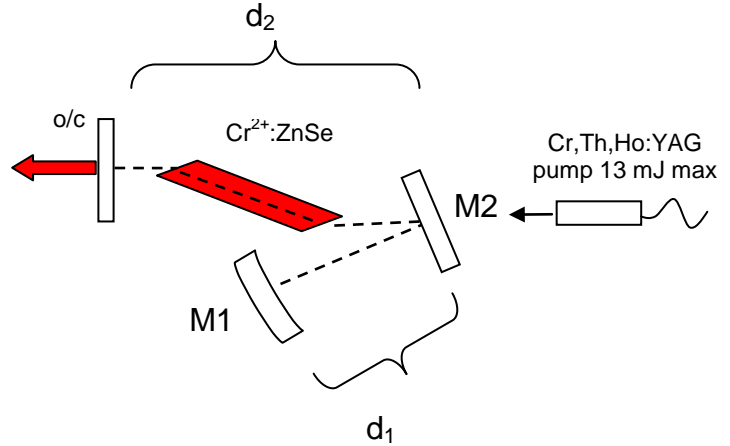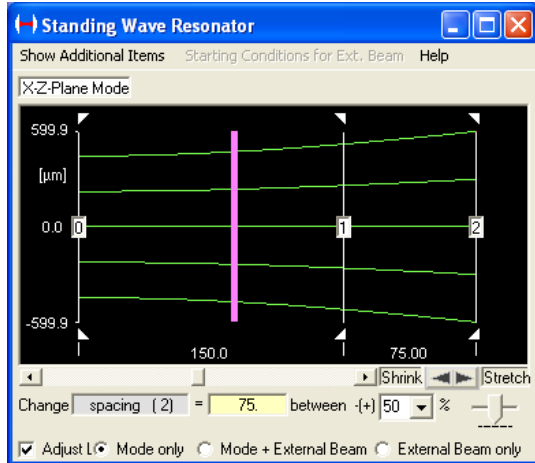
Figure 23. Cavity design for Cr^{2+}:ZnSe gain-switched laser including mode size (top left), optical layout (top right) and actual laser cavity (bottom)

Gain-switched output

The pulse energy, slope efficiency, temporal profile, spatial characteristics and spectral profile of the gain-switched output are analyzed in this section.

Lasing pulse energies using 50% and 70% outcouplers are presented in Figure 24 along with their slope efficiencies. In order to measure lasing slope efficiencies, the incident pump pulse energy was calibrated to the reflection from a Thor Labs BP108 beam splitting pellicle, and Cr^{2+}:ZnSe pulse energy was measured on an RJ-735 energy head and RJ-7620 ratiometer. Measurement of unabsorbed pump energy was performed

43

over the range of pump powers by recording the laser output after dumping the Cr^{2+} emission away with a dichroic mirror. This unabsorbed pump energy was subtracted from the incident pulse energy to yield the '*absorbed pump*' x-axis in Figure 24.
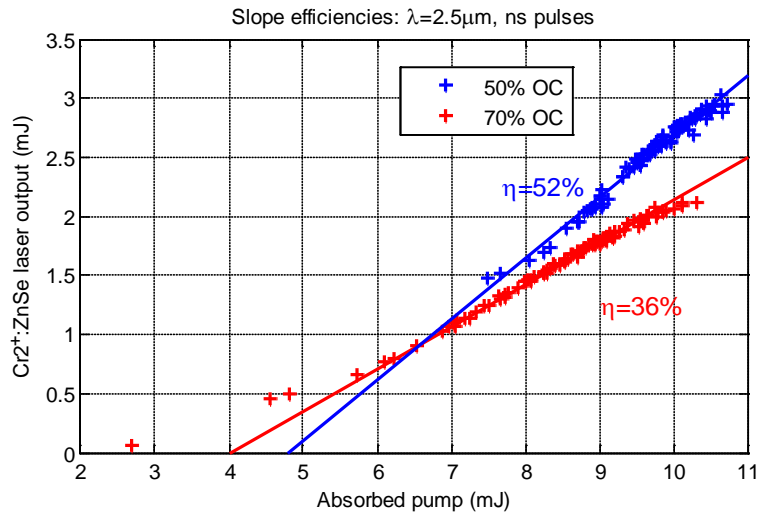
Figure 24. Slope efficiencies for gain-switched Cr^{2+}:ZnSe output

The 3.1 mJ pulse energy is compared to maximum theoretical pulse energy using an efficiency method and also an excited ion method. Using the efficiency method, the maximum gain-switched laser output is the product of the quantum efficiency, pump efficiency, coupling efficiency and pump energy.

Quantum efficiency for this 4-level laser is $\frac{h\nu_{2.5}}{h\nu_{2.05}}$, or 82%. Imperfect mode-matching could result in ~ 80% pump efficiency. Coupling efficiency should be high at ~90% as Seigman (p1014) states "*the output energy from a Q-switched laser is largely independent of the exact cavity output coupling ... providing the coupling is not so large as to reduce r (the inversion ratio) too close to unity*". Combining these terms yields an

estimated efficiency of 60%, resulting in 6.2 mJ possible output from 10.5 mJ of absorbed pump energy.

Another way to calculate the theoretical maximum pulse energy is to find the energy in the mode volume if all Cr^{2+} ions are excited. This energy is the product of hv, the mode volume and doping level of 7.8×10^{18} cm^{-3}, and a maximum energy close to 10 mJ results from a 500 μm mode radius. Atmospheric absorption is the likely cause for the laser's failure to provide maximum theoretical pulse energy, although sub-optimal coatings or passive losses within the gain medium could also contribute.

The gain-switched temporal profile is shown in Figure 25 (left) for a 50% reflective outcoupler (blue) and a 70% reflective outcoupler (red). Also shown are the temporal profiles from two other works that used a 90% or 30% reflective outcoupler.
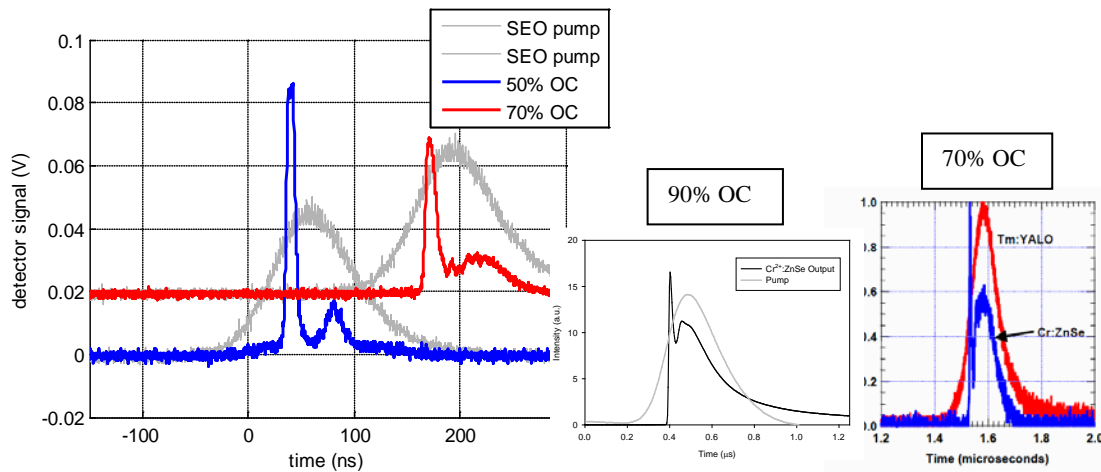
Figure 25. Temporal profile of gain-switched Cr^{2+}:ZnSe output (left) and output from two previous works: middle [48], right [49]

45

As the outcoupler reflectivity is reduced, the amount of energy in the secondary peak is shifted towards the primary peak. It would be desirable to have all the energy in the primary peak, which may be possible if a 40% outcoupler were available.

For this laser, a beam quality of $M^2 = 1.4$ was measured for both x and y axes, with a slight astigmatism as shown in Figure 26 (left). Figure 26 (right) shows that the beam has a near-Gaussian spatial profile at focus, as measured with a 10 μm pinhole.
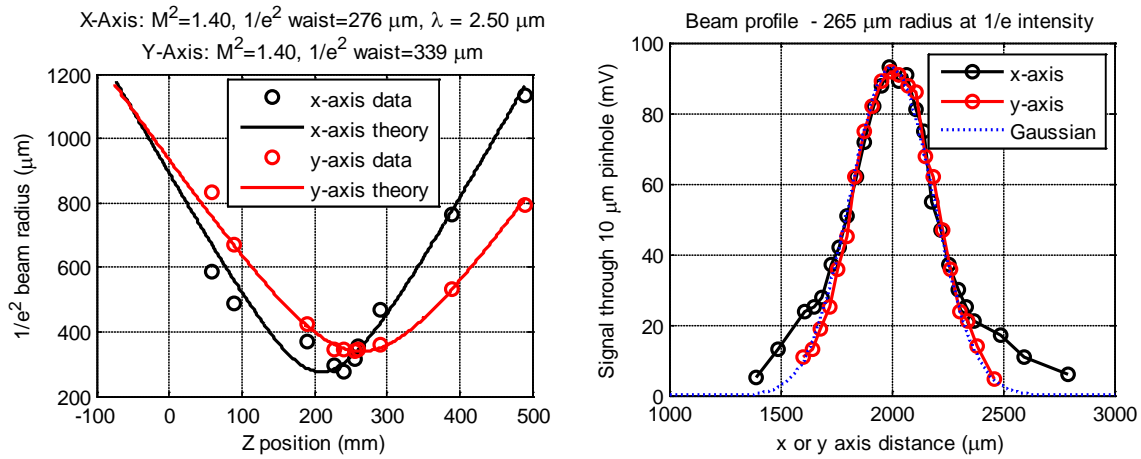
Figure 26. Cr^{2+}:ZnSe laser beam quality measurement (left), and spatial profile (right)

The spectral content of the pulses were measured with an ARC SpectraPro-750 three-quarter meter monochromator. The spectrum was sampled at 0.2 nm increments from 2000-2800 nm by using 2 mJ pulses and measuring the monochromator output on an RJ-735 energy head, which varied from 1-25 μJ. During the experiment, the incident pulse energy was sampled with another RJ-735 energy head and the RJ-7620 ratiometer *ratio* output was used as the input to the SpectraPro GUI. The measurements given in Figure 27 showing a 2.47 μm peak emission, 110 nm linewidth (full width at 1/*e* pulse

energy) and verifies there is no 2.095 μm pump present. Additionally, the LEEDR-predicted [1] atmospheric transmittance over a 2 meter path length is overlaid in black.
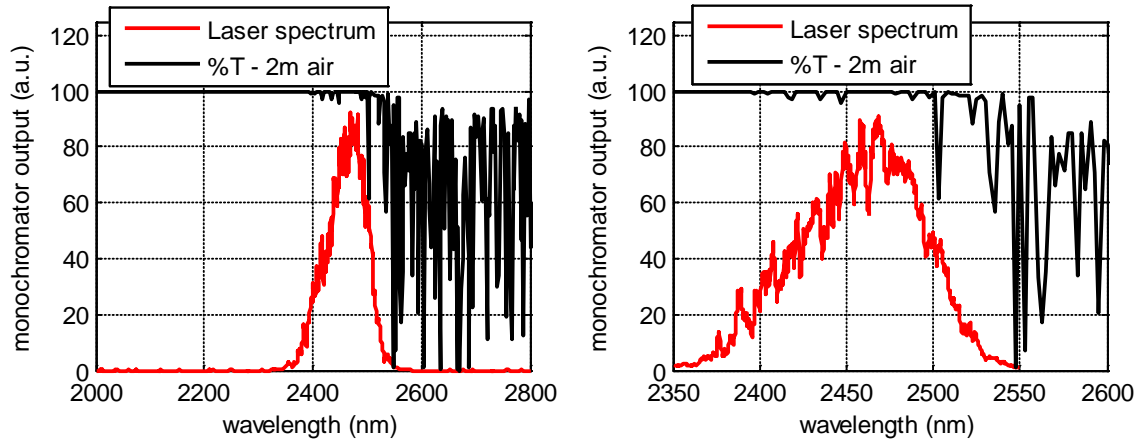
Figure 27. Spectra of gain-switched Cr^{2+}:ZnSe laser output. (left) Complete spectra showing no 2.095 μm pump present, (right) zoomed in to show peak emission and linewidth

Significance

Record Cr^{2+}:ZnSe peak power has been achieved with this laser, as shown in Table 7. Peak power is defined as the pulse energy divided by the full pulse width, and 3.1 mJ pulse energy in a 60 ns pulse width yields a peak power of 52 kW, doubling the record held by Carrig's 18.5 W average power gain-switched laser [49]. However, the peak power is higher if calculated directly, which is performed below the table.

All gain-switched Cr^{2+} pulses in the literature have a temporal profile consisting of an impulse followed by a structured pulse. As previously shown in Figure 25, the pulses produced by the laser in this work have a much higher proportion of energy in the initial 10 ns FWHM impulse, making it worthwhile to calculate the peak power directly.

Table 7. Cr²⁺:ZnSe literature search, organized by peak power

Pulse energy	Pulse full width	Slope efficiency (%)	PRF	Outcoupler (%R)	Peak Power (W)	Mode of operation	Reference
2 mJ	*	3 or 5	-	99.5	-	GS	Gallian [65]
-	-	-	-	-	12	CW	Moskalev [69]
14 mJ	120 μs	66	1Hz	66	117	GS	Koranda [66]
4 nJ	11 ps	-	100 MHz	-	364	ML	Pollack [70]
0.4 mJ	200 ns	50	10 kHz	90	2,000	GS	McKay [48]
375 pJ	100 fs	-	200 MHz	-	3,750	ML	Sorokina [71]
444 pJ	80 fs	-	180 MHz	-	5,556	ML	Sorokina [72]
2.6 mJ	100 ns	65	7 kHz	70	26,000	GS	Carrig [49]
3.1 mJ	60 ns	52	3 Hz	50	**51,667 (194,000)**	GS	Present work

Legend: * = not published. CW = continuous wave, GS = gain-switched, ML = modelocked

The power P_i at each scope time step ($\tau = 0.2$ ns) is calculated by fitting the entire scope trace to the expression 3.1 mJ $= \sum P_i * \tau$. The output of this method is presented in Figure 28, where the peak power of the pulse is calculated as 194 kW.

energy in gain-switched pulse = 3.10 mJ, Peak Power = 194 kW
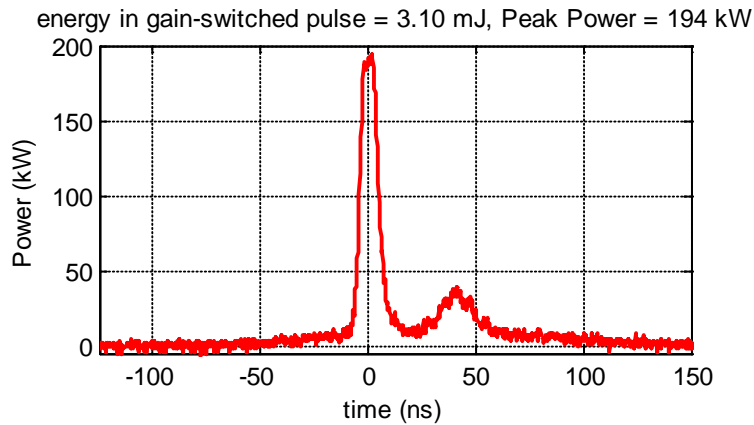
Figure 28. Peak power calculation for 3.1 mJ gain-switched Cr²⁺:ZnSe laser output

4.5 mJ and 5.0 mJ pulse energies were also observed from the laser, but upon further investigation they were not a single pulse. Instead, they consisted of two ~50 ns pulses within a 1 µs timeframe. This would not increase the peak power of the laser, and resulted from the pump drifting to a poor temporal profile. The final observation from Table 7 is that mode-locked peak power is low despite a fs or ps pulse width, because the energy of individual pulses is very small (nJ or pJ).

2.05 µm Laser Source Modifications

A nanosecond 2.05 µm Tm,Ho:YLF laser [48] used in the NLA tests is described in this section, however, the laser was designed for CW or kHz Q-switched operation which is not suitable for NLA testing. Modifications are documented which allowed the laser to run in a single-shot mode or low PRF in order to satisfy the thermal diffusion constraint on PRF which is calculated later in this chapter.

The laser crystal was cooled to -140 °C using a CryoTiger closed-cycle system and was pumped by a 792 nm water-chilled diode focused to a 450 µm spot radius on the crystal. Losses in the cavity were modulated using a NEOS acousto-optic Q-switch, and cavity design details include a 20 cm one-way path length and an 80% outcoupler with a 50 cm radius of curvature. Characterization was performed on the laser resulting in a 30% slope efficiency, lasing threshold of 4 W pump, 2 nm linewidth and a beam quality of $M^2 = 1.2$. The laser possessed a Gaussian spatial profile and 1.8 mrad divergence.

The quasi-CW pumping scheme described here was implemented to give 10 Hz operation by implementing a Q-switched mode of operation that pumps the crystal for 6 ms prior to each pulse with a variable repetition rate [73,74]. In this scheme, the pump

diode is modulated and a delay generator is triggered from the diode driver, which in turn opens the Q-switch after a variable delay.

The delay before opening the Q-switch is based on Louchev's work, which used an 8-level model to determine that a 0.7 ms delay allowed optimum relaxation from the Tm^{3+} $^{3}H_4$ level to the $^{3}F_4$ level and finally to the lasing Ho^{3+} $^{5}I_7$ level [75,76]. Louchev's empirical verification of the optimal delay is shown in the left graph of Figure 29, and the right graph presents a comparison of the resulting CryoTiger pulse energy in blue and pulse full width in red.
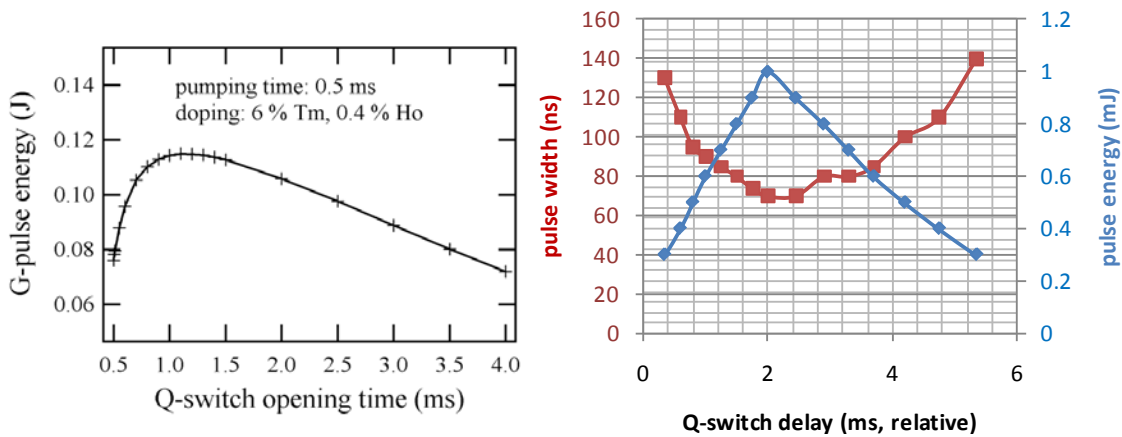
Figure 29. (left) Louchev quasi-CW pulse energy vs. delay Q-switch opening [75,76]. (right) Comparison with data taken for CryoTiger laser, including pulse width

Semiconductor Samples

The two materials investigated are Ge and GaSb, which are shown in Figure 30. The optical, electrical and thermal properties of these samples are characterized in this section. Two second order effects that influence NLA and damage are modeled, which are variation of linear absorption with temperature and variation of free carrier recombination time with free carrier density. The effectiveness of an anti-reflective

coating is studied and then surface quality is evaluated with measurements from a scanning electron microscope and atomic force microscope. Finally, all material properties from measurements and literature values are summarized in Table 8.

Figure 30. Semiconductor samples: germanium (left) and gallium antimonide (right)

Ge is an indirect bandgap material according to the band structure diagram shown in Figure 31 (left) where the effective bandgap is circled in red. For an indirect bandgap material, theoretical predictions of β use the effective bandgap $E_{\Gamma1}$, as β was found to be a factor of 2,000 times less at the indirect gap [77].
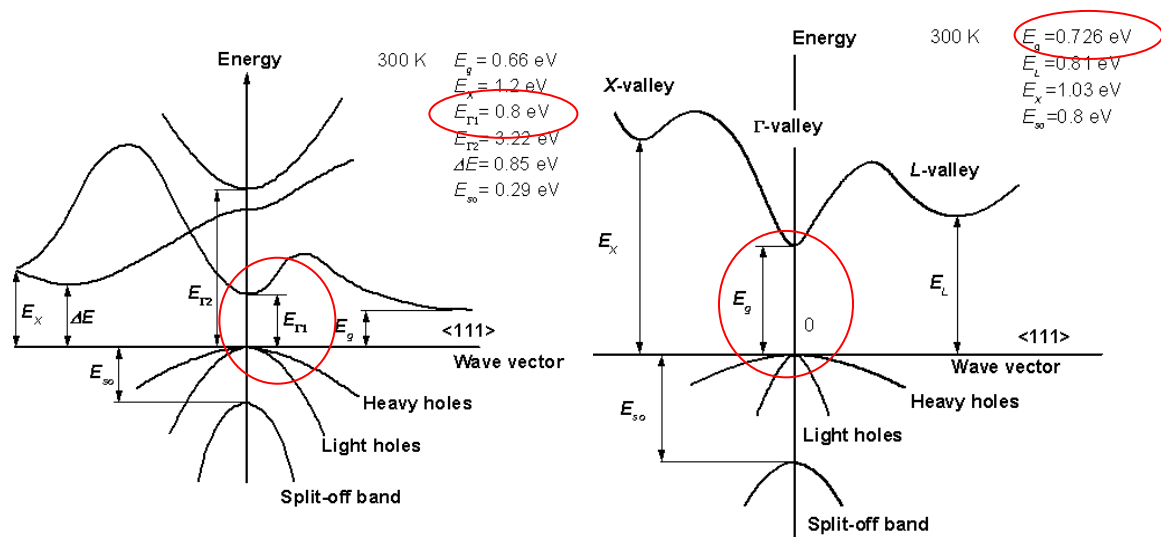
Figure 31. Band structure of Ge (left) and GaSb (right) [78]

Temperature dependent linear absorption

In order to increase the accuracy of damage modeling, FTIR spectra for Ge and GaSb spectra were obtained from room to near-melting temperatures [79]. The goal of this effort was to capture the dramatic increase in linear absorption (α) that occurs due to lattice expansion and an increase in phonon vibration from thermally excited carriers. This phenomenon is named 'thermal runaway' because for CW illumination, if a sample starts to heat up, it will continue to increase in absorption and heat up further, triggering an exponential process that results in damage.

As shown in Figure 32, linear absorption increases dramatically at temperatures above 450 K or 500 K for Ge and GaSb, respectively. The dashed blue lines are 600 K spectra for both materials, showing that the effect is much stronger in Ge. The bottom graph in Figure 32 presents $\alpha(T)$ for both materials at 2.5 μm where α is calculated using Eq. 24-26, where *%T* is normalized to account for Fresnel reflections:

$$I(z)\Big/I(0) = \frac{\%T}{100} = e^{-\alpha z} \qquad \ln\left(\frac{\%T}{100}\right) = -\alpha z \qquad \alpha = -\ln\left(\frac{\%T}{100}\right)\Big/z \qquad \text{(24/25/26)}$$

The material bandgap also changes, as shown by a rightward shift of the transmission edge from wave number $k = 5500$ cm^{-1} to $k = 4500$ cm^{-1} in Figure 32. The change in material bandgap is presented in [79] and will change the nonlinear absorption by altering β. While discussed here, $E_g(T)$ and the resulting $\beta(T)$ are not implemented in the finite difference model as the resulting $\Delta\beta$ was calculated to be less than the error bars on the final measurements.

52
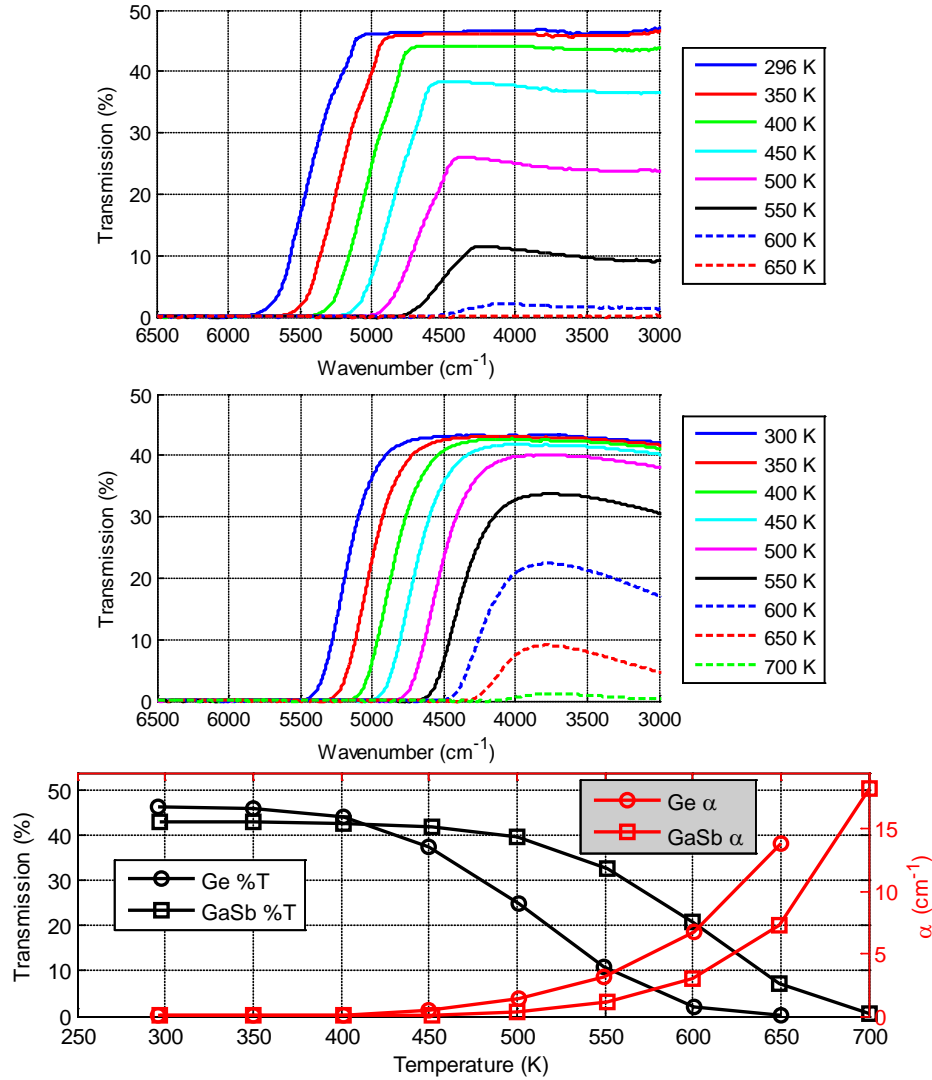
Figure 32. Temperature-dependent spectra for Ge (top) and GaSb (middle) [79]. The bottom chart is the resulting *%T* and *α* vs. temperature at 2.5 μm (*k* = 4000 cm⁻¹).

Free carrier density dependent recombination

The level of nonlinear absorption will decrease if a significant number of free carriers recombine during a pulse. Because free carriers relax at a rate which depends on the free-carrier density, this effect is studied as it can significantly affect free-carrier absorption, transmission and temperature rise leading to damage. *N*-dependent recombination lifetimes $\tau_R(N)$ are determined here for inclusion into the FD model.

53

There are three processes that contribute to relaxation: Auger recombination, radiative recombination and Shockley-Read-Hall (SRH) recombination. At the modeled carrier densities in these experiments (10^{16}-10^{20} cm^{-3}), SRH recombination [80,81] can be neglected as it is insignificant compared to either radiative or Auger recombination.

When the recombination rates in Table 8 are used to calculate τ_R from Eq. 12, an important difference between indirect and direct bandgap materials is highlighted. For an equivalent N, radiative recombination is suppressed in Ge as it must be phonon assisted, and resulted in $\tau_R(N)$ of 250-500 ns during the NLA testing. This was several times longer than the 37-68 ns pulses in these experiments, and τ_R did not reduce NLA in Ge. However, the GaSb $\tau_R(N)$ of 45-65 ns was on the order of the pulse width, which reduced the NLA and the increased the LIDT as carrier recombination occurred during the pulse.

Figure 33 graphs the recombination parameters both separately (dashed and dotted lines) and combined (solid lines) over a range of N. As shown in Figure 33, radiative recombination dominates in GaSb until N is greater than 10^{20} cm^{-3} (damage-level), while in Ge, Auger recombination dominates for any N greater than 10^{17} cm^{-3}. This inhibits relaxation when compared to GaSb, causing a greater number of generated carriers which then increases free-carrier absorption and lowers the Ge LIDT. The impact of this parameter is explored in the *sensitivity analysis* section of this chapter.

Anti-reflective coatings

The high indices of these materials result in significant Fresnel reflection at each surface, as calculated in Table 8 at the end of this section. This could add a challenge to the nonlinear measurements – even if Ge has zero absorption at a given irradiance, only 39.7% of the light will pass through, and for GaSb 43.6% will transmit.

54
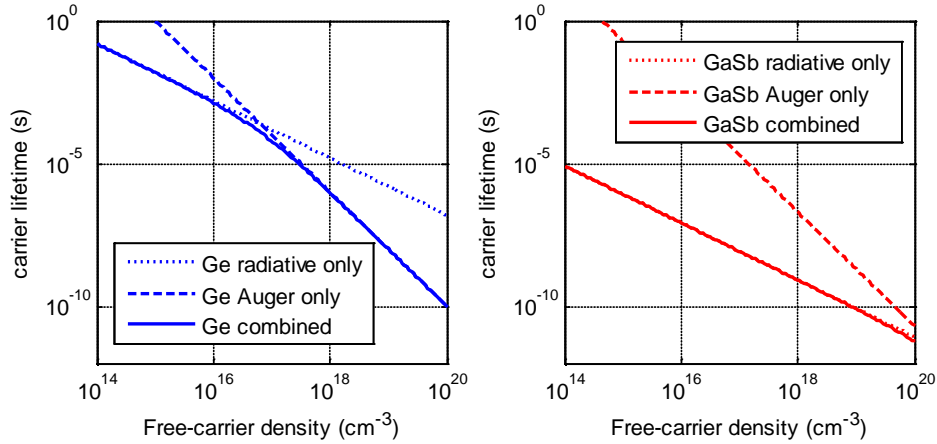
Figure 33. Carrier lifetime vs. free carrier density in Ge (left) and GaSb (right)

In order to increase transmitted energy and prevent strong internal reflections from distorting the NLA measurements, anti-reflective coatings were applied to a portion of each sample. Aluminum oxide (Al_2O_3) is the amorphous form of sapphire and was selected for the coating material as its refractive index is close to the square root of the index of GaSb and Ge, which maximizes the efficiency of the coating.

The single-layer coating thickness of 361 nm was calculated to give a quarter-wavelength optical path length in order to maximize the destructive interference of the reflection. The coating was applied to both samples at the University of Dayton using a 150-watt RF plasma sputter deposition process from a 3" aluminum oxide target. The final thicknesses of the coatings on the front and back surfaces were measured as 360.5 and 361.3 nm, respectively. The partially coated Ge sample is shown in Figure 34 and spectra before coating and after coating for both samples are given in Figure 35.

55
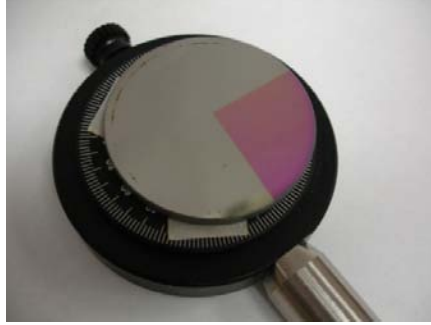
Figure 34.   Ge sample showing the coating on the bottom right quadrant
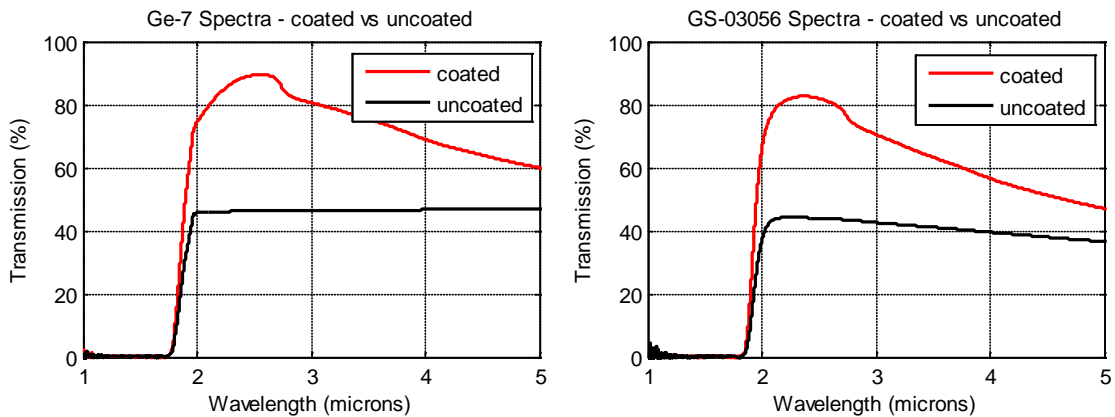
Figure 35.   Transmission improvement with coated sample: Ge (left), GaSb (right)

The spectra show that the index match was imperfect, as 95% transmission was predicted and 80% - 90% transmission was achieved. However, this was a significant improvement over the uncoated samples and deemed acceptable for NLA testing.

Pre-test inspection

As specified in ISO standard 11254-1 [44], surface inspections before damage testing were performed on a Hitachi S-4700 Scanning Electron Microscope (SEM) and a Veeco NanoScope V atomic force microscope (AFM) at the AFIT cleanroom. For the SEM, the reflective sample surfaces initially caused a lack of contrast but increasing the voltage to 18 kV improved the images.

Figure 36 shows SEM imagery for the Ge and GaSb samples and the scale is given in the lower right corner.
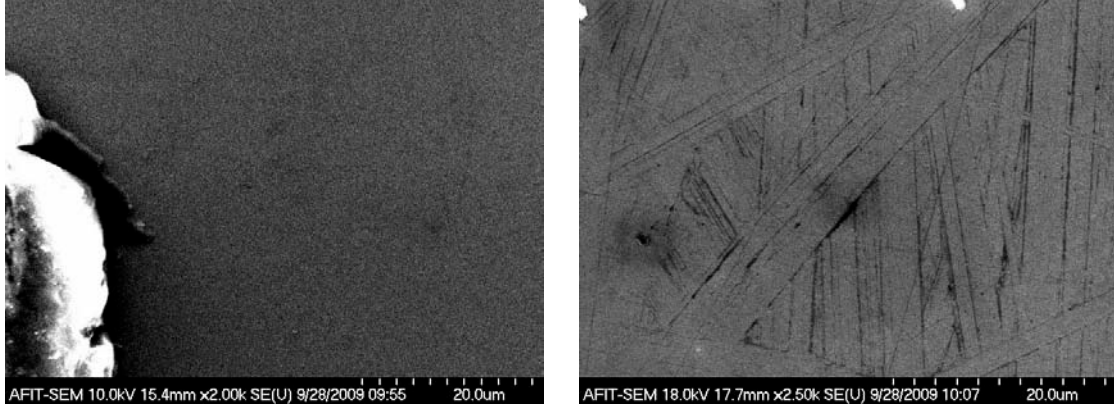
Figure 36.   Pre-test SEM imagery of samples. (left) Ge 2000x view of the general surface. (right) GaSb 2,500x view of the general surface

AFM surface roughness measurements of the samples were also performed. The two parameters that describe surface roughness are the *arithmetic* average (R_a) of a number N of surface height deviations Z_j and the root mean squared average of these deviations (R_q) [82]:

$$R_a = \frac{1}{N}\sum_{j=1}^{N}|Z_j| \qquad R_q = \sqrt{\frac{\sum_{j=1}^{N}|Z_j|}{N}} \qquad (27/28)$$

The results from the AFM measurement are presented in Table 8 and show that GaSb has slightly lower roughness despite the scratches visible in Figure 36. However, both samples have an optical-grade finish – for example R_a = 2 nm is the 'precision' fabrication tolerance from CVI Melles Griot. Optical, electrical and thermal properties

57

for these materials that are used in NLA and damage threshold modeling are presented in

Table 8 for Ge and GaSb.

Table 8. Material properties for Ge and GaSb samples

Property	Ge	Ref	GaSb	Ref
Thickness (mm)	3.05	M	1.06	M
Index of refraction at 2.5 μm	4.06	[78]	3.749	[78]
Fresnel loss per surface (%)	37	C	34	C
Bandgap (eV)	0.8[*]	[78]	0.726	[78]
Surface roughness R_a parameter (nm)	1.73	M	1.46	M
Surface roughness R_q parameter (nm)	2.21	M	1.87	M
Melting temperature (°K)	1210	[78]	985	[78]
Thermal conductivity (W/cm°C)	0.58	[78]	0.32	[78]
Density (g/cm^3)	5.32	[78]	5.61	[78]
Specific heat (J g^{-1}K^{-1})	0.31	[78]	0.25	[78]
Thermal diffusivity (cm^2/s)	0.352	[78]	0.228	[78]
Free carrier diffusivity (cm^2/s)	44	[85]	77	[86]
Resistivity (Ωcm)	1865	M	2717	M
Electron mobility μ_n (cm^2/Vs)	3900	[78]	3000	[78]
Hole mobility μ_p (cm^2/Vs)	1900	[78]	1000	[78]
Ionizing potential (eV)	7.9	[43]	5.03	[42]
Intrinsic free carrier density (cm^{-3})	~10^{12}	C	~10^{12}	C
Radiative recombination coefficient (cm^3/s)	6.4×10^{-14}	[78]	1.2×10^{-9}	M
Auger recombination coefficient (cm^6/s)	1×10^{-30}	[78]	5×10^{-30}	[33]
2.05 μm linear transmission from FTIR / spectrophotometer (%)	77.1 / 76.5	M	73.8 / 77.0	M
2.05 μm transmission indicated by data (%)	72	M	71.5	M
2.5 μm linear transmission from FTIR / spectrophotometer (%)	89.4 /89.3	M	82.1 / 85.6	M
2.5 μm transmission indicated by data (%)	87	M	87	M

Legend: M = measured, C = calculated, * = effective gap

The last four rows of Table 8 present linear transmission measurements on the coated portions of the samples. The FTIR values are taken from the same data as Figure 35, and the 'indicated by data' values are the transmissions at the lowest irradiances in the NLA experiments. There is a small difference between the FTIR and indicated values. The tests were performed at different locations on the samples, and it is possible that the coating thickness (and therefore transmission) varied slightly across the surface. Additionally, periodic surface cleaning may have slightly degraded coating quality between sites.

Nonlinear Study

The calculations, analysis and design work that support the nonlinear absorption testing are presented here. There are several factors that could possibly contribute to nonlinear absorption, and accurate measurement of nonlinear coefficients requires careful test design to avoid the effects that cannot easily be modeled. In this section these effects are described, a sensitivity analysis of NLA parameters is presented and experimental procedures are outlined.

Design of experiments

Several factors are described here that could possibly contribute to nonlinear absorption. Awareness of these factors is needed to either rule them out, create a test designed to avoid them or understand the process well enough to model the effect.

Thermal diffusion: Heat generated by the incident pulse influences absorption by changing the level of linear absorption, as reported in the *Samples* section. Test results could be distorted if heat escapes during the pulse width or if residual heat builds

up in the spot area over repeated pulses. To avoid these effects, test constraints for spot
size and maximum laser PRF are calculated. The distance that heat will diffuse within
the time of the laser pulse is the definition of the diffusion length L in Eq. 29 [83]:

$$L^2 = 4D\tau_p \qquad \text{where} \qquad D = \kappa/\rho C \qquad (29)$$

In Eq. 29, D is diffusivity, κ is conductivity, ρ is density and C is heat capacity
and Table 9 shows the calculations of the diffusion length for various pulse widths.

Table 9. Values used to determine thermal diffusion length in Ge and GaSb samples, using
materials data from [78]

	pulse width	conductivity κ (W/cm°C)	density σ (g/cm^3)	specific heat C (J/g°C)	diffusivity D (cm^2/s)	diffusion length L (μm)
Ge	10 ps	0.58	5.32	0.31	0.352	0.03
Ge	100 ns	0.58	5.32	0.31	0.352	3.8
Ge	5 μs	0.58	5.32	0.31	0.352	27
GaSb	10 ps	0.32	5.61	0.25	0.228	0.03
GaSb	100 ns	0.32	5.61	0.25	0.228	3.0
GaSb	5 μs	0.32	5.61	0.25	0.228	21

If the spot size is much larger than L, there is negligible spread of heat in the pulse
duration and the test will not be affected. Table 9 shows that thermal diffusion can be
ignored for the ps and ns pulses used in these experiments, but may need to be taken into
account for μs and longer pulses, depending on the spot size.

If testing is accomplished using a train of pulses, thermal diffusion dictates a
maximum PRF that will allow heat to dissipate out of the spot area in between pulses.

60

This PRF is calculated in Table 10, using the spot radius r_o, diffusivity D and diffusion time τ_d, which are related by the expression: $\tau_d = \left(\frac{r_o^2}{4}\right)\frac{1}{D}$ [84].

Table 10. Values used to determine maximum PRF in Ge and GaSb samples

	$1/e^2$ spot radius (μm)	diffusivity D (cm^2/s)	diffusion time τ_d	max PRF to have period > 10x τ_d (Hz)
Ge	100	0.352	71 μs	1407
Ge	700	0.352	3.5 ms	29
GaSb	100	0.228	110 μs	913
GaSb	700	0.228	5.4 ms	19

The maximum PRF is calculated as a repetition rate whose period is ten times the thermal diffusion time, so that any heat generated can escape the area in between pulses. The spot sizes for the 3 Hz and 10 Hz experiments in this work were selected to allow a large safety margin with respect to thermal diffusion.

Free-carrier diffusion: In addition to recombining, free carriers generated by the incident pulse can diffuse out of the spot area, which would reduce FCA and therefore alter the test results. Using the same method as thermal diffusion, a free carrier diffusion length L can be calculated as $L^2 = 4D\tau_p$ where a Ge value of D=44 cm^2/s was used from [85] and D=77 cm^2/s was reported in [86] for GaSb.

Table 11 shows that free carrier diffusion is much faster than thermal diffusion, and while it results in a larger diffusion length, it will still be insignificant for ps pulses. However, it may affect ns and longer pulses so care was taken to choose a spot size larger than the free carrier diffusion length.

Table 11. Values used to determine free-carrier diffusion length in Ge and GaSb samples

	pulse width	free carrier diffusivity (cm^2/s)	diffusion length L (μm)
Ge	10 ps	44	0.4
Ge	100 ns	44	42
Ge	5 μs	44	297
GaSb	10 ps	77	0.5
GaSb	100 ns	77	56
GaSb	5 μs	77	392

Intrinsic free carrier absorption: Modeling indicated that changes to absorption could occur due to intrinsic free carriers N_0 if their density levels became greater than 10^{15} cm^{-3}, which could be possible if the sample is heavily doped. The intrinsic carrier concentration is measured in this section to rule out this effect.

Resistivity ρ of the samples was measured using a Fluke 81438 multimeter, a probe area A, sample thickness L, resistance R and the expression $R = \rho \frac{L}{A}$. Conductivity σ and electron/hole carrier concentration (n/p) are related by $\sigma = \frac{1}{\rho} = e(\mu_n * n + \mu_p * p)$ where μ_n is the electron mobility and μ_p is the hole mobility. If the type of carriers is unknown, $\sigma = e(\mu * N_0)$ which results in $N_0 = \sigma/e\mu$. Calculations for the samples are shown in Table 12 for both *n*-doping and *p*-doping.

The results from Table 12 show that the samples are of high purity with intrinsic carriers ~ 10^{12} cm^{-3}. The intrinsic carrier density could be used in the finite difference model to add accuracy to the nonlinear coefficient measurements. However, a level $< 10^{15}$ cm^{-3} will not affect the results as it is insignificant compared to the density of carriers generated by the pulse, which can reach 10^{20} cm^{-3}.

Table 12. Intrinsic carrier concentration calculation in Ge and GaSb samples

if n-type

	path length (cm)	probe area (cm^2)	resistance (Ω)	resistivity (Ωcm)	conductivity (Ωcm)$^{-1}$	electron mobility μ_n (cm^2/V*S)	carrier concentration (cm^{-3})
Ge	0.305	0.36	1580	1865	5.36x10^{-4}	3900	(9±2)x10^{11}
GaSb	0.106	0.36	800	2717	3.68x10^{-4}	3000	(8±2)x10^{11}

if p-type

	path length (cm)	probe area (cm^2)	resistance (Ω)	resistivity (Ωcm)	conductivity (Ωcm)$^{-1}$	hole mobility μ_p (cm^2/V*s)	carrier conc (cm^{-3})
Ge	0.305	0.36	1580	1865	5.36x10^{-4}	1900	(2±0.5)x10^{12}
GaSb	0.106	0.36	800	2717	3.68x10^{-4}	1000	(2.5±0.7)x10^{12}

Nonlinear refraction: There are two ways that nonlinear refraction could affect the nonlinear measurements. The first is that induced refraction could cause the beam to be defocused to the point that some of the pulse energy misses the detector, resulting in an inaccurate energy measurement. This potential problem is alleviated by placing the energy head close to the sample exit surface in order to collect all transmitted energy. The second issue is that nonlinear refraction could focus or defocus the beam within the sample, varying the irradiance and therefore the level of nonlinear absorption.

Refraction would have the greatest effect on the Ge sample as it was three times thicker than the GaSb sample. Modeling was performed on the 2.05 μm Ge NLA data to rule out refractive effects, using nominal Ge values of nonlinear refraction n_2=7x10^{-13} cm^2/W, thermal lensing dn/dT=396x10^{-6} K^{-1} and free carrier refraction σ_{FCR}=7x10^{-21} cm^3. The data points with the highest absorption in both the ns and ps data sets were first modeled without refractive effects, resulting in transmission of 33.3% and

63

31.3%, and temperature rise of 4 K and 0.04 K, respectively. Then n_2 and σ_{FCR} were modeled using the values above, and also after being increased by two orders of magnitude to account for any error in reported values. Both data points changed by less than 0.1% transmission due to these variations. dn/dT is a well known quantity and its addition changed the ns data set by 0.03% T and the ps data point was unchanged.

Three-photon absorption: At 2.5 μm it is possible for three photons to combine to bridge the bandgap of these materials. However, three photon absorption (3PA) is assumed to be negligible at the irradiances used in this study as there is a much lower probability associated with 3PA in a regime where TPA is possible [87].

Measurement method: There are many ways to extract nonlinear coefficients, including measuring transmittance changes, sensing energy absorbed in a material, measuring focusing and defocusing as a function of irradiance, pump probe methods, two-photon fluorescence and finally photoacoustic, optoacuostic and calorimetric methods [88]. An irradiance scan method [47] that measures transmittance change was selected in order to accurately measure two coefficients (β and σ) by fitting the NLA data from two different pulse widths using the single-pulse FD model.

Sensitivity Analysis

The sensitivity of β to variations in pulse width and free-carrier recombination parameters is now discussed, which highlights the need for a dual β/σ fit. β is sensitive to pulse width, as shown from simulations compiled in Table 13. In the table, the β values given are fits to the same data set and the only variation is the pulse width, which varies the peak irradiance level used to fit β.

64

Table 13. β sensitivity to pulse width variation at 2.5 μm

Pulse width	β fit for Ge	β fit for GaSb
8 ps (not a measured value)	-22%	-15%
9.25 ps	-8%	-9%
10.08 ps	0%	0%
10.2 ps	1%	2%
10.9 ps	8%	8%

A sensitivity analysis for free carrier recombination time (τ_R) is now explored. Modeling indicates that changes in τ_R are insignificant at ps timescales, which is expected as $\tau_R \gg \tau_p$ for these materials in this case. However, the variation could be significant for a nanosecond pulse as shown in Figure 37. A 20% change in nonlinear transmission due to a 10x variation in τ_R could cause β to change by a factor of two or more, requiring accurate knowledge of this parameter for accurate ns testing. In Figure 37, τ_p is 65 ns and the black line shows predicted transmission if $\tau_R = 10$ ns. The blue line shows that the absorption increases substantially if τ_R is greater than the pulse width at $\tau_R = 100$ ns.
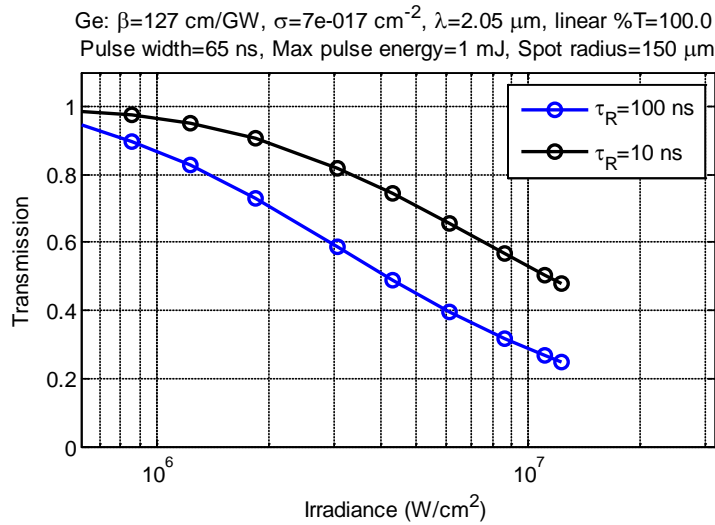
Figure 37. Sensitivity analysis to variations in τ_R for ns NLA testing

65

Finally, a sensitivity analysis was performed to predict β variation with changes in free carrier absorption cross section, as σ is not well known for Ge and GaSb. As shown in Figure 38, β is sensitive to changes in σ at ps timescales.

Ge: β=131 cm/GW, σ=1.6e-016 cm^{-2}, λ=2.50 μm, linear %T=89.4
Pulse width=10.08 ps, Max pulse energy=35 μJ, Spot radius=734 μm
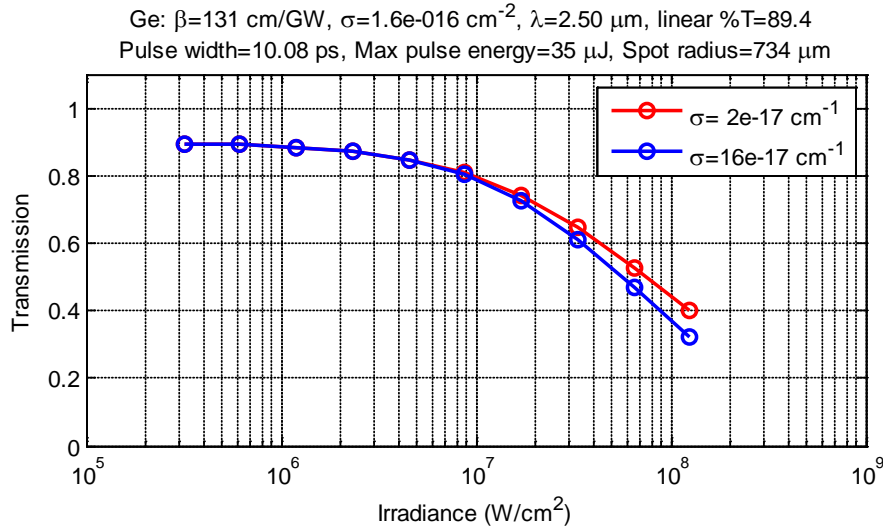
Figure 38. Sensitivity analysis to variations in σ for ps NLA testing

While Figure 38 shows a theoretical variation for Ge, an observation from measured GaSb ps data is that β = 144 cm/GW if σ is estimated as $2\text{x}10^{-17}$ cm^2. β is reduced by 50% when the data is refit with σ increased by 8x, i.e. $16\text{x}10^{-17}$ cm^2, which highlights the need for a simultaneous technique to measure β and σ.

Experimental procedure

As shown in the *sensitivity analysis* section, any inaccuracy in laser beam measurement is magnified when fitting NLA coefficients. As a result, the irradiance-scan apparatus was carefully aligned, calibrated and used according to the following procedures, referencing the experimental setup in Figure 39:

66

- Optimize the laser cavity to provide stable pulse energy
- Measure the pulse width
- The Labview GUI records pulse energy using an external trigger, which can give inaccurate results if the trigger delay is wrong. Make sure the pulse energy does not change in external trigger mode
- Use an IR focal plane array (FPA) to view the spatial profile, make sure the beam is Gaussian throughout the attenuator range of motion
- Perform calibration scans in pulse energy with all combinations of ND filters
- Using pinhole x & y scans, find the focal point and measure spatial profile
- Translate the pinhole to the focal point and measure the $1/e$ spot radius
- If the Rayleigh range is short, focus an IR FPA on the pinhole, remove the pinhole, then install sample and move until the sample is in focus.
- *Perform irradiance scans*
- Check sample transmission at low irradiance to make sure there is no damage resulting from the measurement
- Make sure the laser has not changed during the test
  - Recheck time profile
  - Remove sample and perform calibration scans again
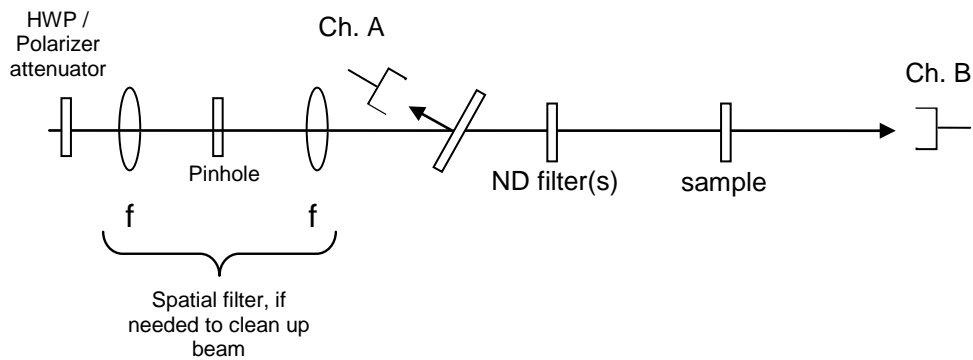
Figure 39. NLA and damage testing experimental setup

As discussed in the literature review, there is a wide variation in reported β values. While the majority of the variation is due to the exclusion of FCA effects, some variation could be attributed to imprecise definitions of peak irradiance, pulse width and

spot size. These parameters are carefully defined here and these definitions are used for all calculations regarding Gaussian beams in this work.

The energy contained in a laser pulse with Gaussian spatial and temporal profiles is defined as the integral of the irradiance profile over time and space in Eq. 30. In Eq. 30, I_0, x_0, y_0, t_0 are defined as the peak irradiance, spot radius in the x dimension, spot radius in the y dimension and pulse half-width, respectively.

$$E = \int_{-\infty}^{\infty} \int_{-\infty}^{\infty} \int_{-\infty}^{\infty} I_0 e^{-\left(\frac{x}{x_0}\right)^2} e^{-\left(\frac{y}{y_0}\right)^2} e^{-\left(\frac{t}{t_0}\right)^2} dxdydt \tag{30}$$

If x_0 and y_0 are equal to a radius r_0 defined at the $1/e$ level of peak irradiance I_0, the integral relationship $\int_0^{\infty} e^{-a^2r^2} dx = \frac{1}{2a}\sqrt{\pi}$ can be used [90]. In this expression, a is defined as either $1/r_0$ or $1/t_0$ and the result is doubled to account for energy in the range -∞ to ∞. The energy in the laser pulse is now solved in Eq. 31.

$$E = I_0 * r_0\sqrt{\pi} * r_0\sqrt{\pi} * t_0\sqrt{\pi}$$
$$= I_0 * \pi r_0{}^2 * t_0\sqrt{\pi} \tag{31}$$

The peak pulse irradiance can then be calculated from the pulse energy, $1/e$ radius of the spot size and $1/e$ radius of the pulse width using Eq. 32.

$$I_0 = \frac{E}{\sqrt{\pi}\tau_p \pi r_o^2} \tag{32}$$

A 10 μm molybdenum pinhole was used to measure the beam radius (r_o) using raster scans along x and y dimensions in all experiments in this work. Pulse width was measured using an autocorrelator for the ps laser source, and mid-IR fast photodetectors for the ns laser sources.

68

Chapter 4.   Experiment and Results

This chapter describes six experiments and their results which have advanced the state of the art in the modeling and measurement of nonlinear optical absorption leading to damage in semiconductors. First, nonlinear absorption coefficients were measured for an indirect bandgap semiconductor (Ge) and a direct bandgap semiconductor (GaSb). Then, as nonlinear absorption is the primary damage mechanism at 2.5 μm, laser-induced damage thresholds due to nonlinear absorption are measured at two pulse widths. Finally, damage threshold modeling is performed to compare theory to experiment and also explore the pulse width dependence of the measured LIDT.

Nonlinear Absorption Investigation

In this section, four experiments and their results are presented which measure NLA coefficients in Ge and GaSb at two wavelengths in the mid-IR region for the first time. In the pages below, the experimental setup, beam characterization, calibration and nonlinear absorption data are presented for both the picosecond and nanosecond NLA tests on Ge and GaSb. An uncertainty analysis follows after β and σ are measured using a simultaneous fit method.

Picosecond NLA experiment

Two nonlinear absorption experiments were conducted on Ge and GaSb at both $\lambda = 2.5$ μm and $\lambda = 2.05$ μm using picosecond pulses. The laser source was a 10 Hz Ekspla model PL2143 that produced 532 nm and 1064 nm wavelengths separately in two arms. This output was sent to an Ekspla PG501 DFG2-10P frequency converter.

69

The $AgGaS_2$ crystal in the frequency converter is pumped with simultaneous 532 nm and 1064 nm pulses from the PL2143. The 532 nm light is passed through a variable optical parametric generator stage (OPG) to down-convert the light which is then mixed with the 1064 nm pump in an angle-tuned difference frequency generation stage to achieve a 2.5 µm or 2.05 µm idler. The overall experimental setup is shown in Figure 40.
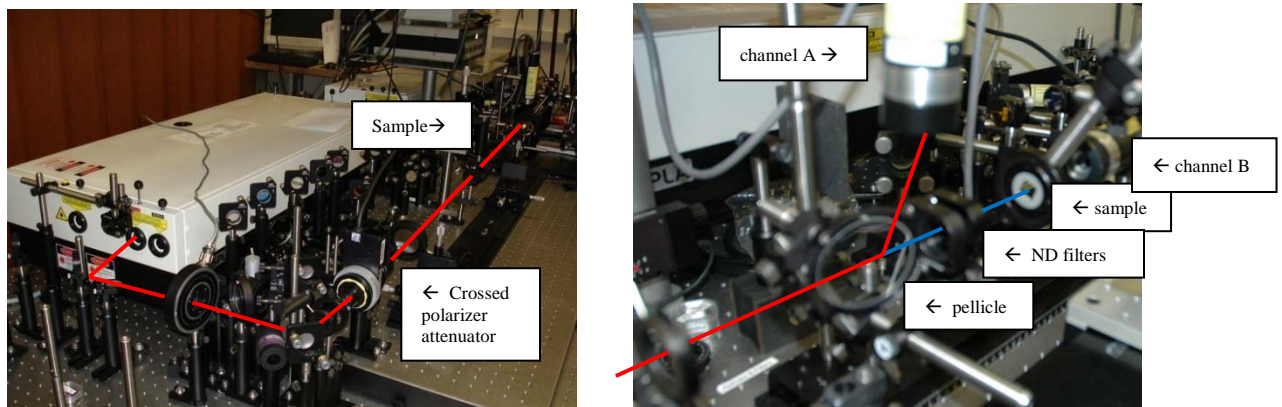
Figure 40. (left) Overall nonlinear experimental setup. (right) close-up showing sample, channel A and channel B

The beam was spatially filtered through a 500 µm pinhole to achieve a Gaussian profile and no focusing of the beam was required to see significant nonlinear absorption. The maximum pulse energy incident on the samples after spatial filtering was 30-35 µJ. Attenuation to achieve a range of irradiances across two orders of magnitude was accomplished with two neutral density filters that were flipped in and out of the beam for large increments and a computer controlled attenuator for fine control. The optical densities of the two filters were 0.3 and 0.6.

The computer controlled attenuator consisted of two optics; the first was either a polarizer for the 2.5 µm tests or a half wave plate for the 2.05 µm tests, and the second

optic was a polarizer oriented to pass only horizontally polarized light. 100% horizontal polarization was maintained throughout the optical path to prevent polarization-dependent reflections from skewing the results. This was important with the Thor labs BP208 8% reflective pellicle that was used to sample the pulse energy, which would only reflect if the incident beam was polarized perpendicular to the plane of reflection.

Beam characterization

Pulse width was measured using an autocorrelator, and beams were spatially characterized using a Boston Electronics IR photodetector mounted behind a 10 µm pinhole. Pinhole scans along x and y axes were taken to measure the spatial profile. Measurements showing the pulse width and spot size at 2.5 and 2.05 µm are given in Figure 41 and Figure 42, respectively.

The Ekspla laser output has a 11.5±0.6 ps pulse width based on a Gaussian fit to its autocorrelation [91], and the 2.05 µm and 2.5 µm output pulse widths are further reduced due to nonlinear conversion. Using an Ekspla non-collinear autocorrelator, pulse width was measured using two-photon absorption in a Ge detector. An autocorrelation will always be symmetric as it is the convolution of a pulse with itself – so this measurement will give an accurate pulse width but does not give a true temporal pulse shape.

Assuming a Gaussian temporal profile, a deconvolution factor of $\sqrt{2}$ was used and the 2.5 µm pulse width was measured as 10.1±0.83 ps. The same technique was used to measure the 2.05 µm pulse as 10.2±0.8 ps, as shown in Figure 41.

71
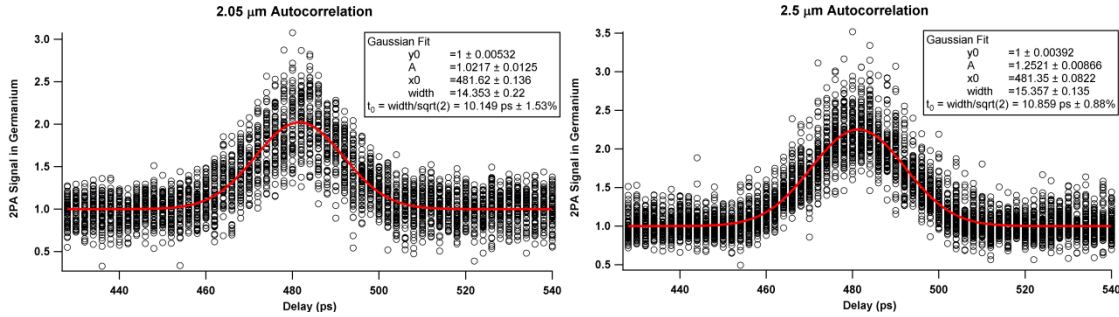
Figure 41.   Pulse width autocorrelations of 2.05 µm output (left) and 2.5 µm (right) [91]

The beams had near-Gaussian spatial profiles, as shown in Figure 42. For the 2.5 µm NLA tests, a 734 µm spot radius at $1/e$ irradiance was measured, and a 584 µm spot radius was measured for the 2.05 µm NLA tests.
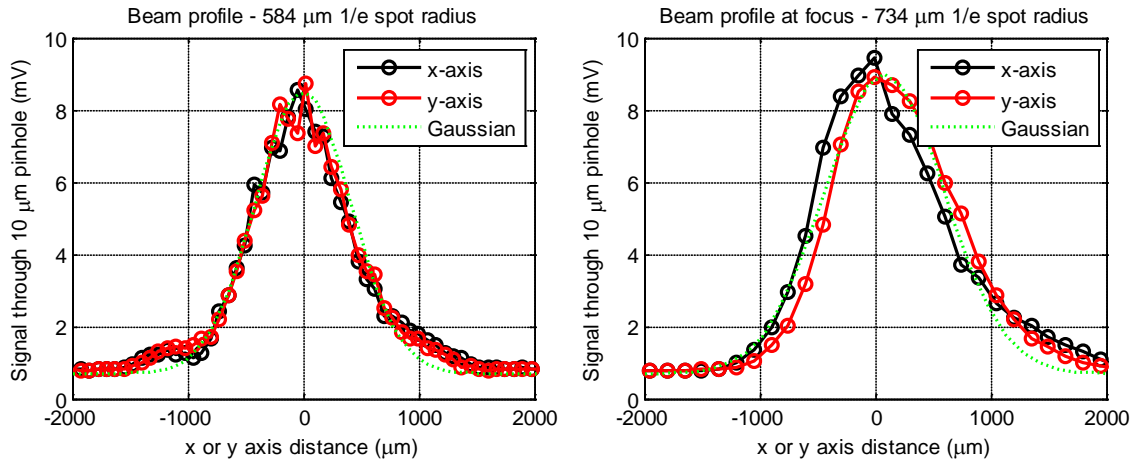
Figure 42.   Beam characterization for the NLA tests showing x and y profiles, overlaid with a Gaussian profile. (left) 2.05 µm beam with a 584 µm spot. (right) 2.5 µm, 734 µm spot

Pulse energy was calibrated using the reflection from a Thor labs BP208 pellicle beamsplitter to measure the total pulse energy that was incident on the sample. With the sample removed, calibration data was taken at 2.05 µm and 2.5 µm for the four possible combinations of ND filters. For each combination of ND filter and wavelength, two runs

were recorded. After the NLA tests, these calibration values were used to calculate the

percent transmission though the sample. In some experiments the calibration varied with

pulse energy, requiring a mathematical fit to the calibration curve.

2.5 μm picosecond NLA

The nonlinear absorption data collected using picosecond pulses at a wavelength

of 2.5 μm are shown in Figure 43 for Ge (left) and GaSb (right). The data consist of 16

runs, and absorption obtained from each of the four combinations of ND filters is

displayed as a different color.
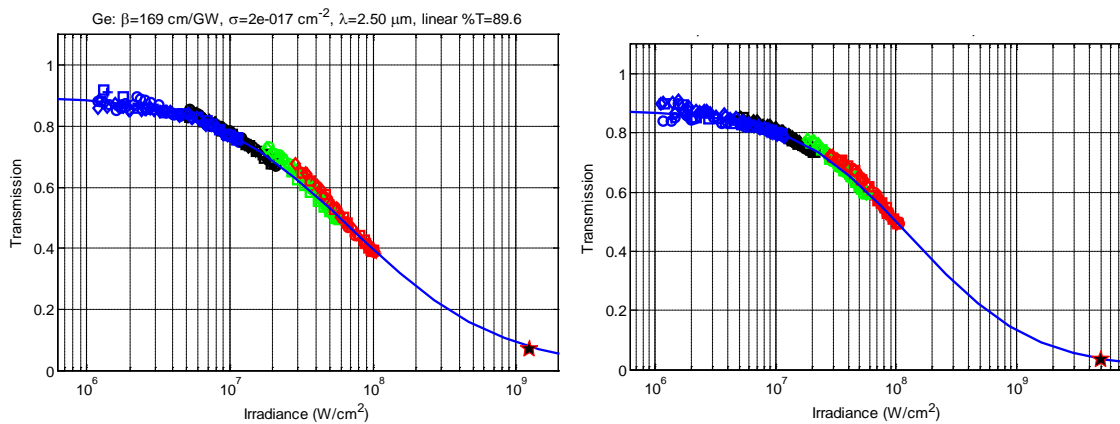
Figure 43.   NLA data and theory for Ge (left) and GaSb (right) at 2.5 µm. The blue line is theory from the FD model, and the star is irradiance at the laser-induced damage threshold

It must be noted that the nonlinear coefficients cannot be determined from data at

a single pulse width, as there are numerous combinations of β and σ that result in an

excellent fit. This is shown in the title of Figure 43 (left) where the β and σ values are

significantly different than the final ns-ps best fit.

73

The nonlinear absorption data collected using picosecond pulses at a wavelength

of 2.05 μm are shown in Figure 44 for Ge (left) and GaSb (right). There were more

losses in the optics leading to the sample at 2.05 μm, when compared to 2.5 μm. This

caused less data to be available at 2.05 μm as either channel A or channel B became

noisy at pulse energies less than 0.5 μJ.
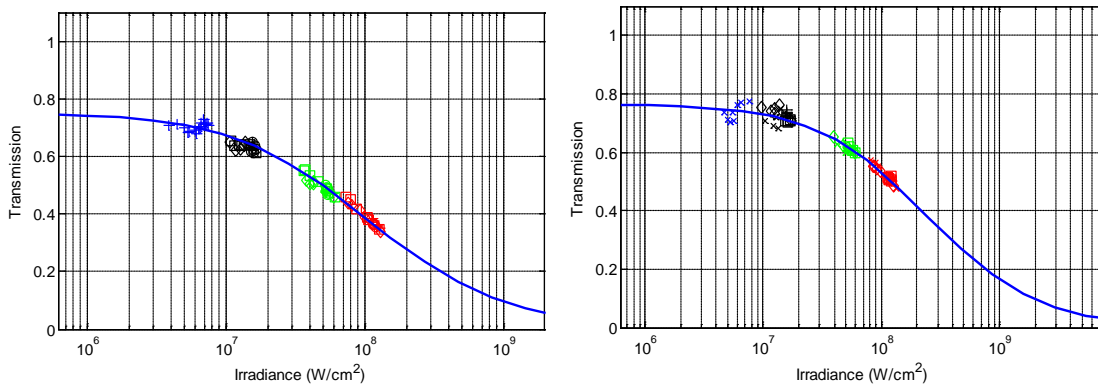
Figure 44.   2.05 μm NLA data and theory for Ge (left) and GaSb (right)

Nanosecond 2.05 μm NLA experiment

This section describes the third NLA experiment, which was conducted on Ge and

GaSb at a wavelength of 2.05 μm. The laser source was a nanosecond Tm,Ho:YLF laser,

which was modified to provide 10 Hz operation as described in Chapter 3.

Experimental setup

In the apparatus shown in Figure 45, attenuation was achieved using a half wave

plate rotated relative to a fixed polarizer orientation, maintaining horizontal polarization

throughout the optical path. As in the ps tests, a diagnostic Channel A measurement was

taken using an 8% reflection from a Thor Labs BP108 pellicle beamsplitter prior to

focusing onto the sample using a coated lens. Channel B measures transmission through the sample and the ratio of Channel B over Channel A gives the percent transmission for each pulse.

NLA measurements were automated with a LabView GUI combined with a Newport PR50PP computer controlled rotation stage that drives the attenuator. This allowed a series of 20-shot pulse energy averages to be recorded in a single run.
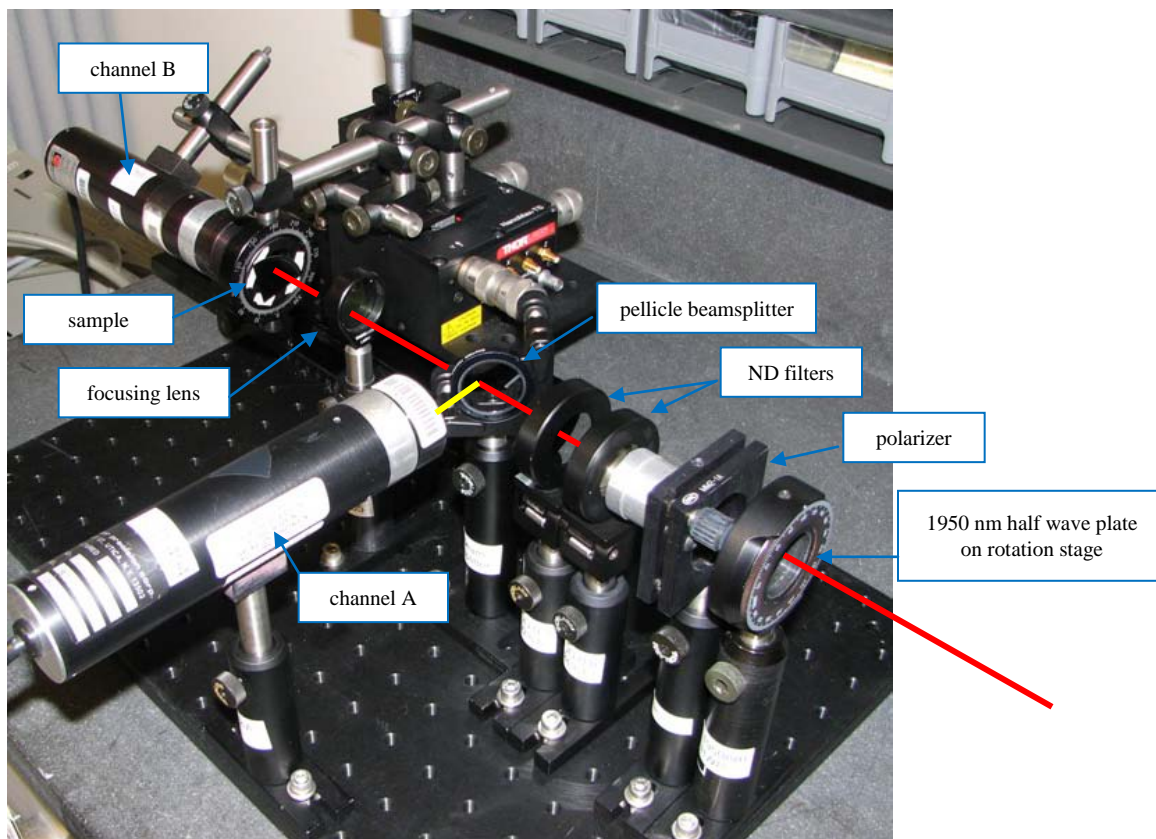
Figure 45. Portable NLA measurement apparatus. In actual testing the focusing lens was replaced with a weaker focus and was located to the right of the picture

Beam characterization

In the experiment, spot size was measured by conducting 10 μm pinhole raster scans along x and y axes, and the temporal profile was measured with an extended InGaAs detector. As shown in Figure 46, the pulses used in ns testing are very well approximated by a Gaussian 74.1 ns pulse full width at 1/*e* irradiance, and the spatial profile was a perfect Gaussian in x and y axes. The Gaussian pulse is modeled using its half-width at 1/*e* irradiance, which was 37 ns in this case.
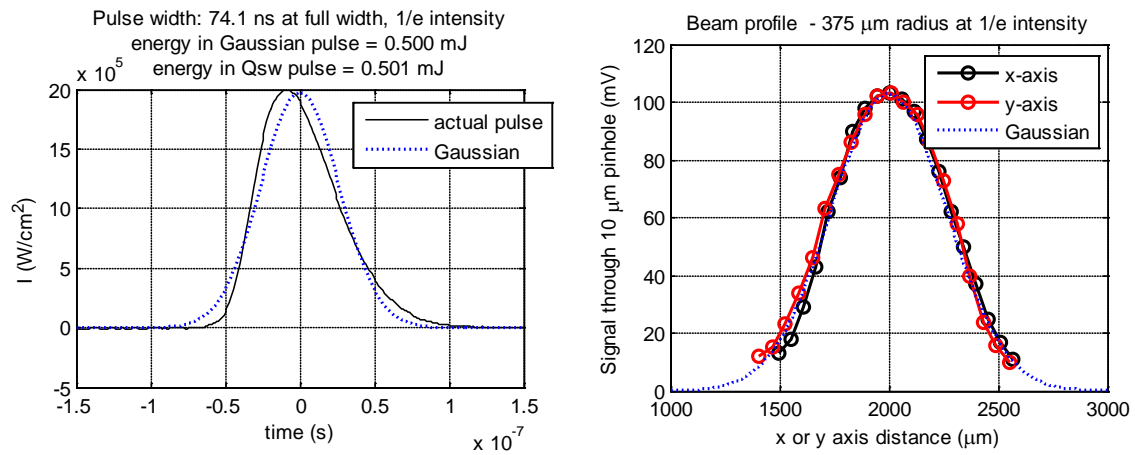
Figure 46. 2.05 μm Gaussian pulse profiles in time (left) and space (right)

2.05 μm nanosecond NLA

The nonlinear absorption data collected using nanosecond pulses at a wavelength of 2.05 μm is shown in Figure 47 for Ge (top) and GaSb (bottom). For an identical range of irradiances tested, Ge experienced a much higher level of nonlinear absorption.

76
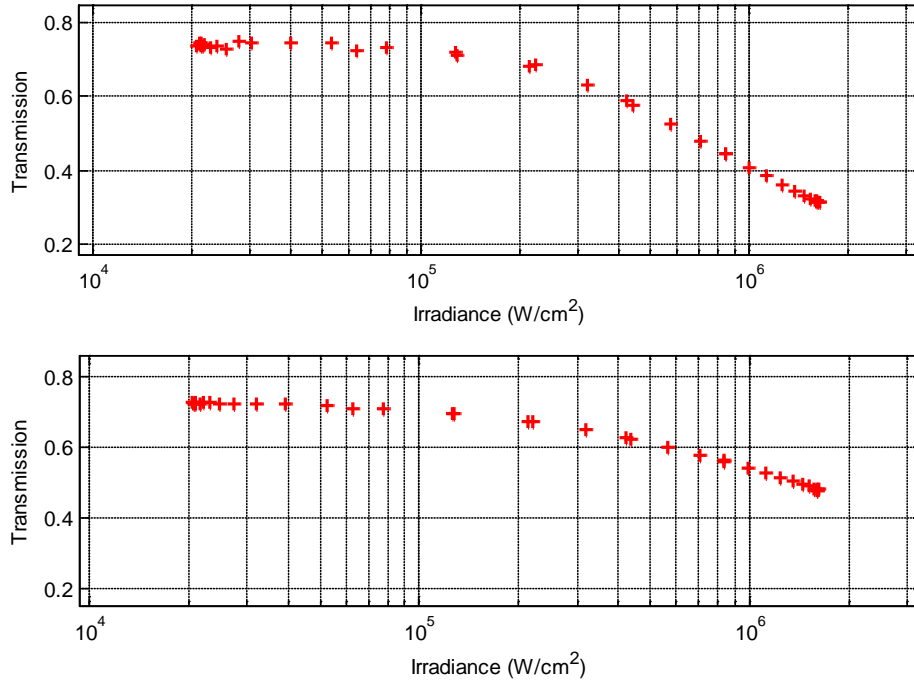
Figure 47.   2.05 μm ns NLA data for Ge (top) and GaSb (bottom)

Nanosecond 2.5 μm NLA experiment

The fourth NLA experiment was conducted on Ge and GaSb at $\lambda = 2.5$ μm using nanosecond pulses. The experimental setup was the same as the ns 2.05 μm test described above, with the exception that the gain-switched Cr^{2+}:ZnSe laser was used as the laser source. The source was characterized to a 265 μm spot radius at focus with a near-Gaussian spatial profile, as shown previously in Figure 26 (right) on page 46.

As described in the *Gain-switched* laser section, the spectral content of the pulses were measured with an ARC SpectraPro-750 three-quarter meter monochromator, yielding a 2.47 μm peak emission and 110 nm linewidth. The ps experiment was performed using 2.50 μm pulses, so there is a slight difference in wavelengths. β theoretically changes by less than 4% over the range 2.4-2.5 μm for either Ge or GaSb,

77

which is shown in Figure 48 (right). This variation is acceptable as it is less than the error bars on the final β measurements.
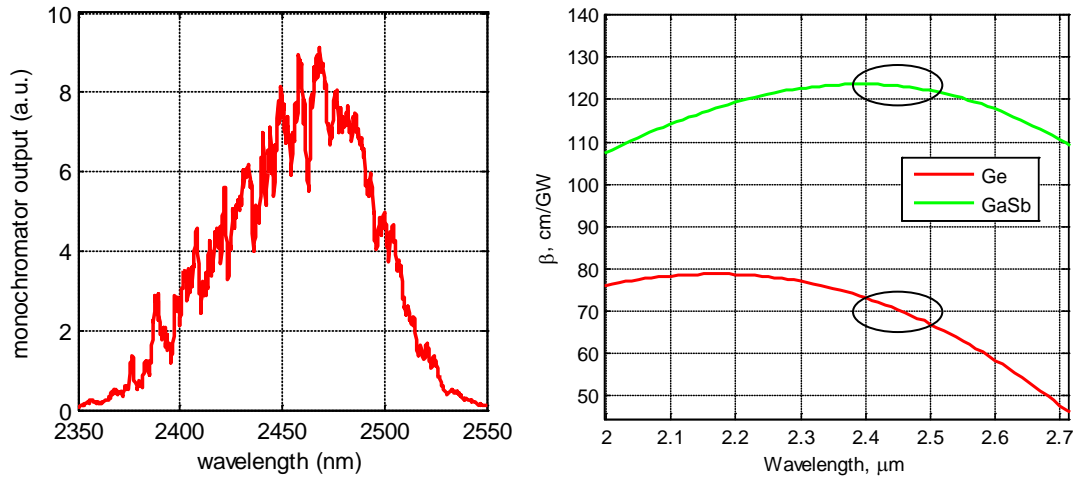
Figure 48. Spectra of gain-switched Cr^{2+}:ZnSe laser output (left), predicted β for Ge and GaSb in this range (right)

Prior to taking data, the experiment was calibrated twice with no sample in place. The first calibration used an ND filter to increase the dynamic range of the experiment, and the second calibration was performed with no ND filter in place to maximize the energy incident on the sample. The nonlinear absorption data collected using nanosecond pulses at a wavelength of 2.5 μm for Ge and GaSb is shown in Figure 49.

Simultaneous fitting of NLA coefficients to ns and ps data

The quantitative simultaneous fit method was performed on all NLA data in order to extract β and σ, which are difficult to separate using other methods. This builds on the work in [89], where β and σ are measured using a self-consistent method on dual-pulse width NLA data. In this section the fitting method is described, β and σ are measured at wavelengths of 2.05 μm and 2.5 μm, and an uncertainty analysis is conducted.

78
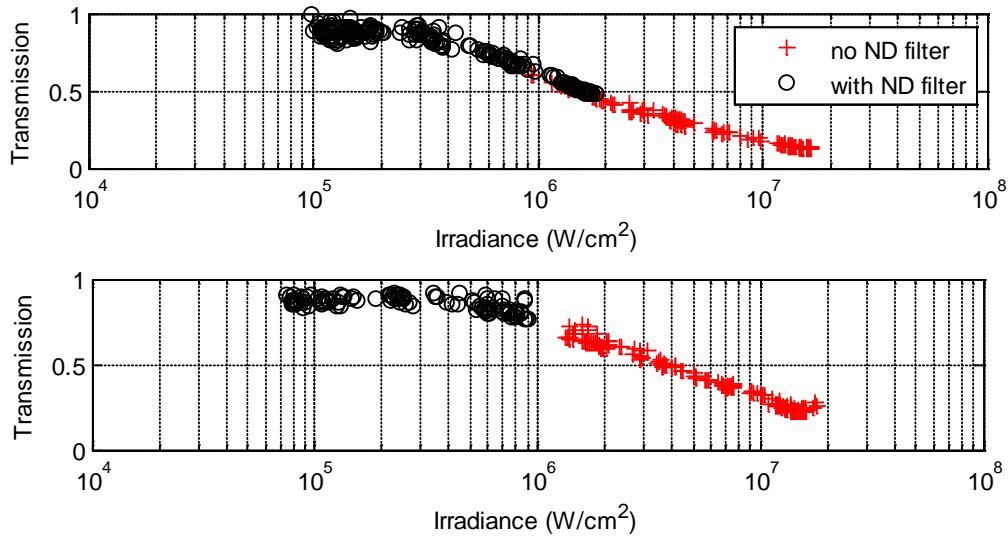
Figure 49. 2.5 μm NLA data for Ge (top) and GaSb (bottom)

Figure 50 shows the 2.05 μm Ge ns NLA data (red) and ps NLA data (blue), along with the theoretical fitting lines obtained from the quantitative best fit pair of $\beta = 71$ cm/GW and $\sigma = 4.9 \times 10^{-16}$ cm^2 values.
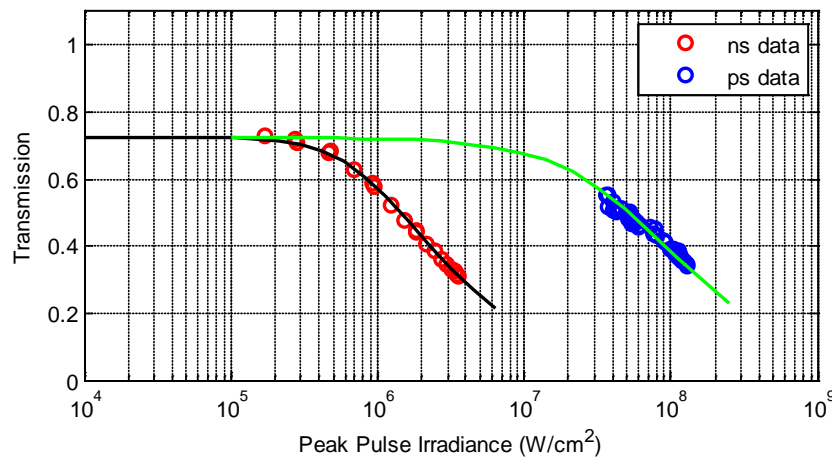
Figure 50. Ge 2.05 μm simultaneous 'best fit' of ns and ps data

The fitting method is shown in Figure 51, which contains six graphs that test for best fit over a wide range of β and σ values. The top row fits both ns and ps data simultaneously. The error metric for the middle row only considers the ns error and shows the resulting best fit for the ns data. Conversely, the bottom row only tries to fit the ps data, and in most cases gives a poor fit for the ns data.

The left column shows the resulting fit on the two data sets, and the right column shows regions where the fit is quantitatively assessed by testing roughly 100 pairs of values using the FD model. The right column plots the inverse sum of squared error (sse), where regions of best fit are shown in red and a yellow star signifies the best quantitative fit.

The ps data prefers a high β and a very small σ as shown in Figure 51 (bottom right), while the ns data cannot tolerate $\sigma < 0.2 \times 10^{-15}$ cm^2 as shown in the middle right graph. The best fit values of β and σ are revealed in the top row, showing that an excellent fit (within 1.5%) is obtained in the top left chart. The range of β and σ that is tested is then decreased in order to increase the accuracy of the fit, as shown in Figure 52.
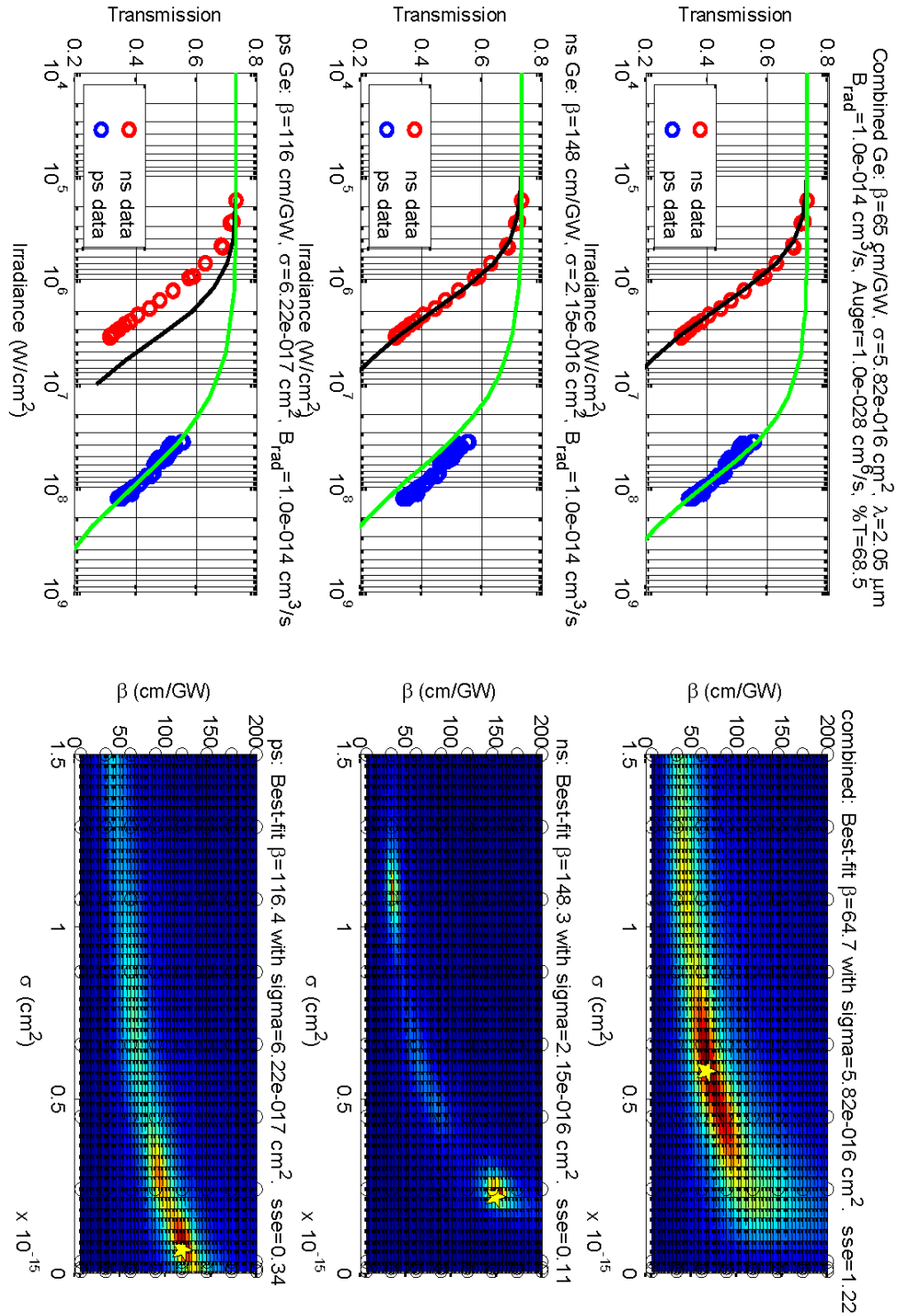
Figure 51. Ge 2.05 µm fitting routine showing best fits to combined ns/ps data (top row), ns data only (middle row) and ps data only (bottom row). In the right column, a yellow star indicates the best fit

combined: Best-fit β=71.4 with sigma=4.93e-016 cm². sse=0.79
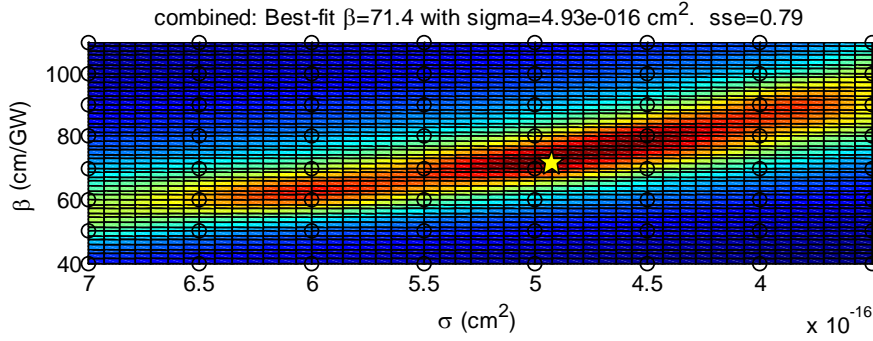
Figure 52. Ge 2.05 µm fitting routine with a tighter range to accurately determine parameters

2.05 µm GaSb simultaneous fit

Using an approach similar to the Ge case, Figure 53 shows the GaSb data taken at

a wavelength of 2.05 μm for ns pulses (red) and ps pulses (blue), along with the

theoretical fitting lines obtained from the quantitative best fit pair of β = 64 cm/GW and

σ = 3.8x10^{-16} cm^2.

GaSb: β=64 cm/GW, σ=3.80e-016 cm², B$_{rad}$=1.2e-009 cm³/s, Auger=5.0e-030 cm⁶/s
ns data: τ$_p$=37.0 ns, 1/e spot radius=375 µm, linear %T=71.5
ps data: τ$_p$=10.2 ps, 1/e spot radius=584 µm, sse=0.78, λ=2.05 µm
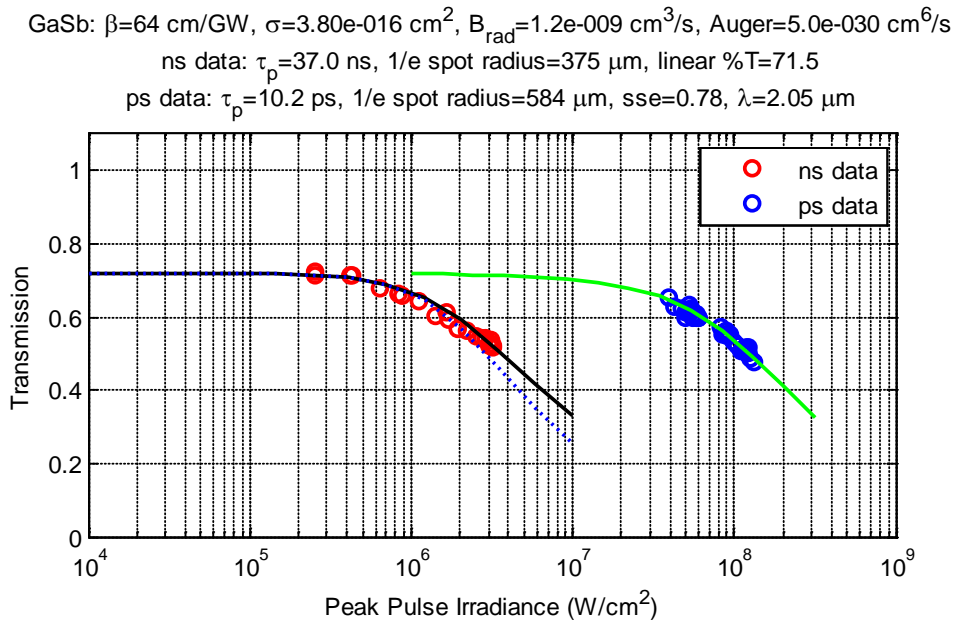
Figure 53. 2.05 µm GaSb simultaneous 'best fit' of ns and ps data. The dashed line is the ns data modeled without recombination

82

The fit was obtained using the same method as Ge, but with one important difference – the radiative recombination parameter (B_{rad}) is large enough to affect NLA, and it was varied to obtain the best fit. It is clear from Figure 53 that the slope of the transmission curve changes when B_{rad} is included, which is caused by free carrier relaxation during the pulse in Figure 53. The best fit occurred at $B_{rad} = 1.2 \times 10^{-9}$ cm^3/s, and it was noted that the best β value did not change throughout the range of B_{rad} tested.

2.5 μm Ge simultaneous fit

Using the gain-switched temporal profile and the same fitting technique as the 2.05 μm Ge data, Figure 54 shows the 2.5 μm Ge ns data (red) and ps data (blue), along with the theoretical fitting lines obtained from the quantitative best fit pair of $\beta = 68$ cm/GW and $\sigma = 9.0 \times 10^{-16}$ cm^2.

Ge: β=68 cm/GW, σ=9.00e-016 cm^2, B$_{rad}$=6.4e-014 cm^3/s, Auger=1.0e-028 cm^6/s
ns data: τ$_p$=34.0 ns, 1/e spot radius=265 μm, linear %T=87.5
ps data: τ$_p$=10.1 ps, 1/e spot radius=734 μm, sse=7.73, λ=2.50 μm
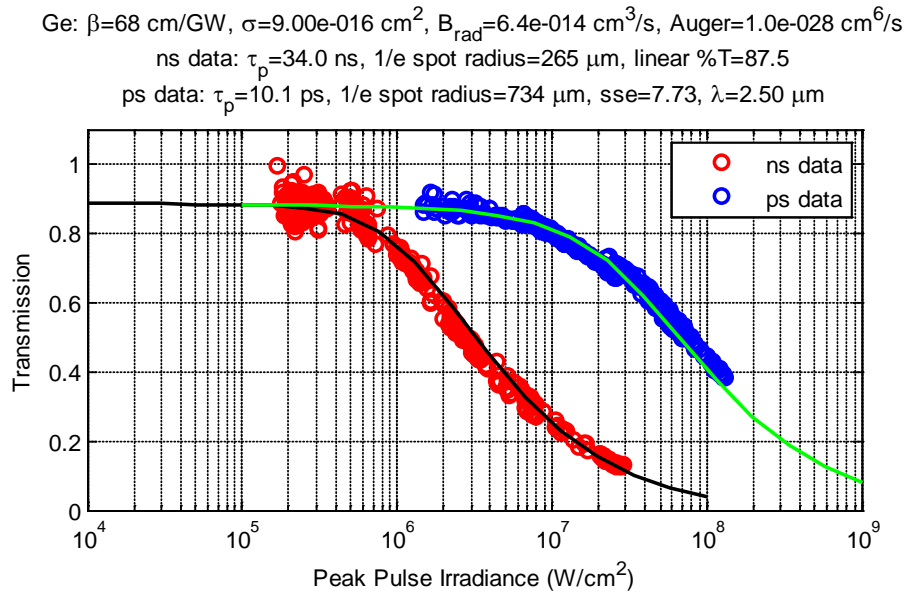
Figure 54. Ge simultaneous 'best fit' of ns and ps data

83

2.5 μm GaSb simultaneous fit

For 2.5 μm GaSb, Figure 55 shows the calculated fitting lines obtained from the quantitative best fit pair of β = 119 cm/GW and σ = 6.5x10^{-16} cm^2. The same radiative lifetime of B_{rad} = 1.2x10^{-9} cm^3/s from the 2.05 μm data yielded an excellent fit.
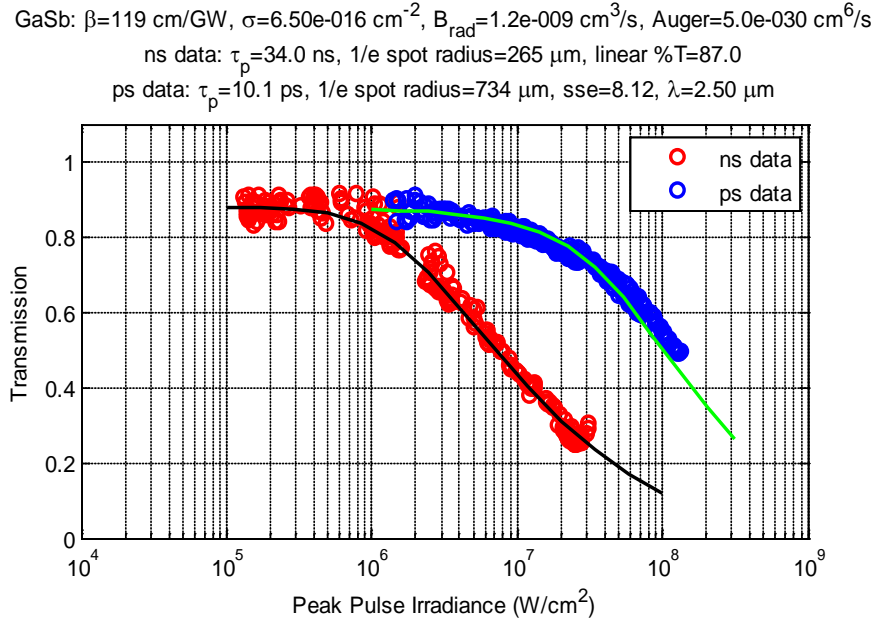
Figure 55. GaSb simultaneous 'best fit' of ns and ps data

NLA uncertainty analysis

Using a two step method, the uncertainties in reported β and σ values are calculated. The first step is to calculate the uncertainty in the peak pulse irradiance that results from inaccuracies in pulse energy, pulse width and spot size. The peak irradiance for a Gaussian pulse and gain-switched pulse are defined below, along with the general propagation of errors expression used to calculate the irradiance uncertainty ΔI:

$$I = \frac{E}{\sqrt{\pi} * \tau_p * \pi r^2} \text{ for a Gaussian pulse} \qquad I = \frac{2.3 * E}{\tau_p * \pi r^2} \text{ gain switched pulse}$$

$$\Delta I^2 = \left(\frac{dI}{dE}\right)^2 \Delta E^2 + \left(\frac{dI}{d\tau_p}\right)^2 \Delta \tau_p{}^2 + \left(\frac{dI}{dr}\right)^2 \Delta r^2$$

The peak irradiance for a Gaussian pulse was derived on page 68, and an expression for the peak irradiance of the gain-switched pulses used in these experiments was determined empirically on page 32. The uncertainty expression requires several partial derivatives for energy, pulse width and spot radius. These are given below for a Gaussian pulse in the top row, and for a gain-switched pulse in the bottom row:

$$\left(\frac{dI}{dE}\right) = \frac{1}{\sqrt{\pi} * \tau_p * \pi r^2} \qquad \left(\frac{dI}{d\tau_p}\right) = \frac{-E}{\sqrt{\pi} * \tau_p{}^2 * \pi r^2} \qquad \left(\frac{dI}{dr}\right) = \frac{-2E}{\sqrt{\pi} * \tau_p * \pi r^3}$$

$$\left(\frac{dI}{dE}\right) = \frac{2.3}{\tau_p * \pi r^2} \qquad \left(\frac{dI}{d\tau_p}\right) = \frac{-2.3E}{\tau_p{}^2 * \pi r^2} \qquad \left(\frac{dI}{dr}\right) = \frac{-2 * 2.3E}{\tau_p * \pi r^3}$$

Cross-variance is excluded as, for example, an error in pulse width will not induce an error in spot radius. As shown in Table 14, the pulse width measurement had the highest uncertainty in all tests. For example, in the ps tests, autocorrelations for 2.5 μm pulse widths performed on separate days were measured as 10.9 ps, 10.15 ps and 9.25 ps [91], yielding a pulse width of 10.1 ±0.8 ps.

The incident pulse energy was measured on Laser Precision RJ-735 heads which are calibrated to 5% accuracy and a 0.5 μJ noise level. The spatial profiles were measured with a 10 μm pinhole and the resulting error of 3-5 μm is calculated from the quality of the Gaussian fit at 1/e irradiance. Using the propagation of errors method, the uncertainty of the peak pulse irradiance is calculated for each of the four experiments and is presented in Table 14.

Table 14. Parameters used to calculate uncertainty in pulse peak irradiance

Wavelength (μm)	Pulse width	Pulse width error	Spot radius	Spot radius error	Pulse energy	Energy error	Peak irradiance (MW/cm²)	±ΔI (MW/cm²)
2.05	10.2 ps	0.8 ps	734 μm	5 μm	40.0 μJ	2.8 μJ	132	15
2.5	10.1 ps	0.8 ps	584 μm	5 μm	25.2 μJ	1.5 μJ	130	13
2.05	37 ns	3 ns	375 μm	5 μm	1030 μJ	52 μJ	3.6	0.35
2.5	68 ns	6 ns	265 μm	3 μm	2080 μJ	110 μJ	22	3.4

The second step is to determine how much the uncertainty in irradiance affects β and σ. It is not possible to apply a propagation of errors method to the rate equations governing nonlinear absorption as they are nonlinear, coupled, and are partial derivatives in other variables. The uncertainty range for β and σ is therefore measured by scaling the peak irradiance of the NLA data using the values in Table 14, and then refitting using the quantitative technique described in this section. The simultaneous fit is sensitive to errors in the ns and ps data, yielding four combinations of errors that require testing: $\pm$ ns I and $\pm$ ps I. The re-fit for two of these combinations is shown in Figure 56.

Figure 56 (left) shows an expected trend, as higher NLA coefficients (β and σ) result if the same absorption occurs at 90% of the original irradiance. Finally, each quadrant of Table 15 gives the best-fit β and σ that result from scaling the NLA data across all four combinations of $\pm$ ns I and $\pm$ ps I for each experiment.

86
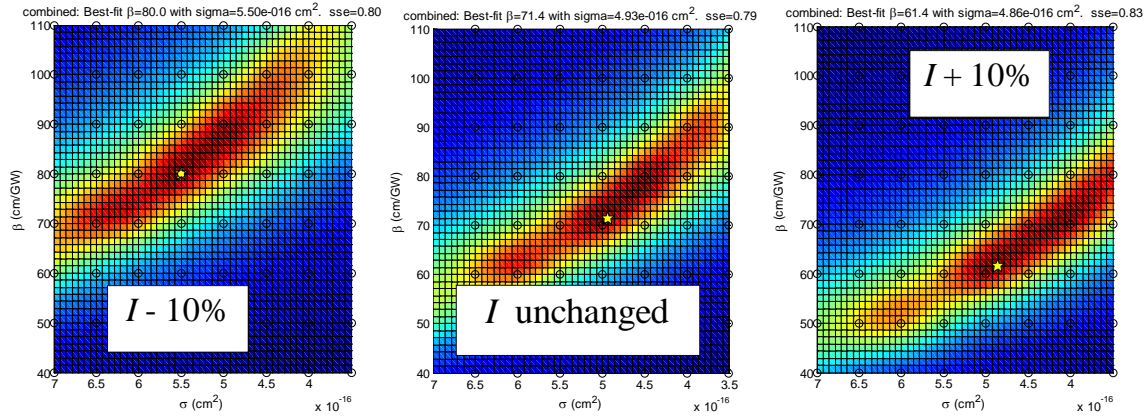
Figure 56. NLA uncertainty analysis – refitting results after scaling NLA data over the error range. (left) the irradiance for both ns and ps data sets is multiplied by 0.9, (middle) no variation, (right) irradiance for both data sets multiplied by 1.1

The red values show little variation when ns and ps data are scaled at the same time, however the blue values show there is greater variation when one data set is scaled with the opposite sign.

Table 15. Results of uncertainty analysis for Ge and GaSb at 2.05 µm and 2.5 µm

GaSb 2.05 µm	ns I = -10%	ns I = 0%	ns I = +10%	GaSb 2.5 µm	ns I = -15.5%	ns I = 0%	ns I = +15.5%
ps I = -11%	70/4.3	β / σ	90/2.5	ps I = -10%	129/7.6	β / σ	148/5.0
ps I = 0%	-	64/3.8	-	ps I = 0%	-	119/6.5	-
ps I = +11%	49/5.4	-	61/3.3	ps I = +10%	86/9.8	-	109/5.9
Ge 2.05 µm	ns I = -10%	ns I = 0%	ns I = +10%	Ge 2.5 µm	ns I = -15.5%	ns I = 0%	ns I = +15.5%
ps I = -11%	80/5.5	β / σ	45.7/9.4	ps I = -10%	69/12.4	β / σ	95/5.7
ps I = 0%	-	71/4.9	-	ps I = 0%	-	68/8.96	-
ps I = +11%	96/3.0	-	61/4.9	ps I = +10%	60/12.5	-	57/9.6

It was noted that the error range for the coefficients presented here is not symmetric, which is expected due to the nonlinear processes involved. Comparisons of β and σ are made to literature values and theoretical trends in Chapter 5 *Conclusion*s.

Laser-Induced Damage Study

The culmination of this research was the measurement and modeling of single-pulse laser-induced damage thresholds in these materials at 2.5 μm for the first time. In this section, the experimental setup, characterization, calibration, damage morphologies and measured thresholds are presented for the damage tests on Ge and GaSb. An uncertainty analysis is conducted on reported LIDT values, and finally pulse width dependent LIDT modeling is performed.

The two experiments described below are performed at picosecond and nanosecond pulse widths. The source for the ps experiment is the tunable Ekspla DFG which was also used in the NLA testing, and the source for the ns experiment is the gain-switched Cr^{2+}:ZnSe laser developed in this work. While the coatings were applied for the nonlinear measurements, the damage threshold of the coating on the Ge sample was measured as an additional data point. The LIDT of the GaSb coating was not measured as the sample possessed insufficient area to allow ps and ns damage grids while still leaving an undamaged portion for the NLA experiments.

Picosecond damage experiment

This section describes single-pulse surface LIDT tests that were conducted on GaSb, Ge and coated Ge at 2.5 μm using 10 ps pulses. In the experiments at the AFRL/RXPJ IR Lab facility, the apparatus used to measure laser-induced damage thresholds is shown in Figure 57.
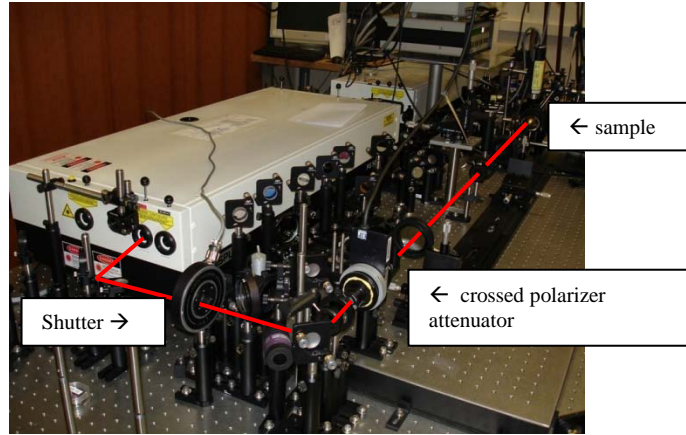
Figure 57.   (left) Overall LIDT setup

The only difference from the NLA setup was that the laser output was passed through a Uniblitz VS25 shutter to allow single shot per site damage testing. The beam was focused onto the sample using a 2.5" focal length coated ZnSe lens. The lens had a tight focus and the spot radius was highly dependent on z position. Accurate placement of the sample surface at focus was achieved by leveraging the power of the lens to image the sample on an IR focal plane array (FPA), as shown in Figure 58.
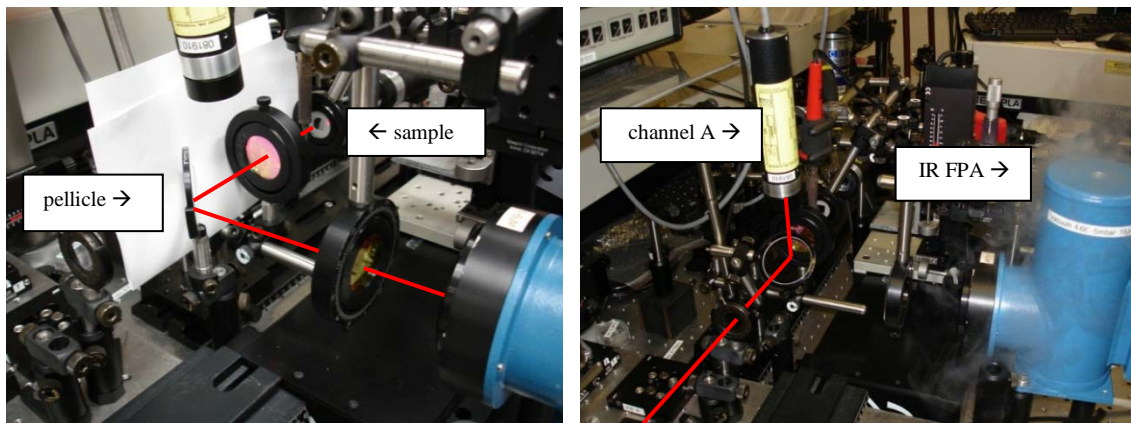
Figure 58.   (left) Imaging sample onto IR FPA using pellicle to accurately position the sample at focus. (right) Setup used during testing – the pellicle is flipped to reflect ~10% of the pulse energy to Channel A as a diagnostic

89

First, the pinhole was located at the beam waist using a series of raster scans and the pinhole was imaged on the FPA. Then, the pinhole would be swapped with the sample and the sample z position would be altered until the sample was in focus. The sample would become in or out of focus at a Δz of 100 μm (0.1 mm), allowing very accurate placement. The process was aided using a soldering iron as a 'thermal flashlight' to bring out details on the pinhole or sample surface on which to focus.

Beam characterization and calibration

The pulse width was previously autocorrelated at 2.5 μm to be 10.1±0.8 ps, as shown in Figure 41 of the NLA section. While the NLA tests used an unfocused beam, a higher energy density is required to induce surface damage and the beam in this test was focused using a 2.5" focal length lens. The beam was spatially characterized using a 10 μm pinhole scans along x and y axes (and various z positions) to measure beam quality, focus point and spot radius. For the GaSb LIDT test, a 44 μm 1/e waist radius was achieved, the beam was slightly astigmatic, beam quality was $M^2 = 1.7$ and it possessed a near-perfect Gaussian spatial profile, as shown in Figure 59.
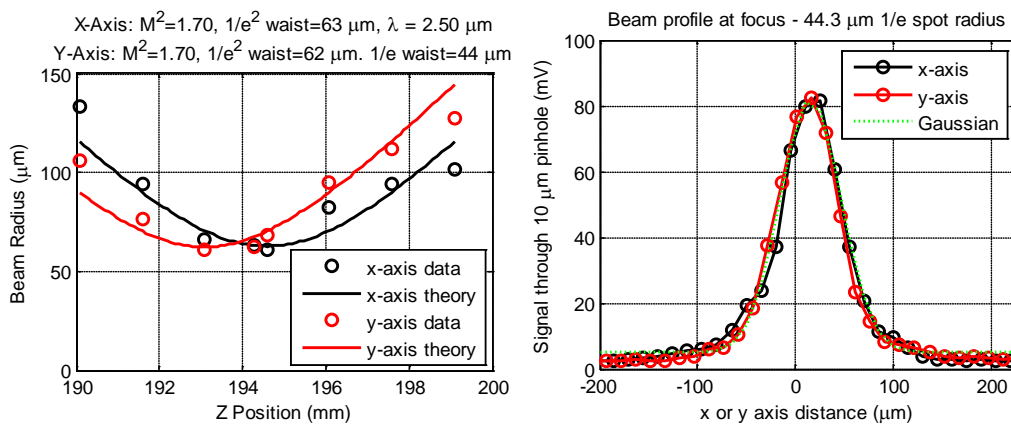
Figure 59.   Beam characterization for GaSb damage test: (left) M^2 data, (right) beam profile measured in x and y axes

For the Ge test, a larger spot was desired. An 8" focal length lens was substituted, characterized to a 150 μm spot and a test was attempted. Unfortunately single shot damage was not achievable, so the 2.5" lens was replaced. The lens was slightly misaligned when installed, which caused the spot radius to increase from 44 to 98 μm and beam quality to change. However this was acceptable as the beam profile at focus was a near-perfect Gaussian and a larger spot radius was obtained, as shown in Figure 60.
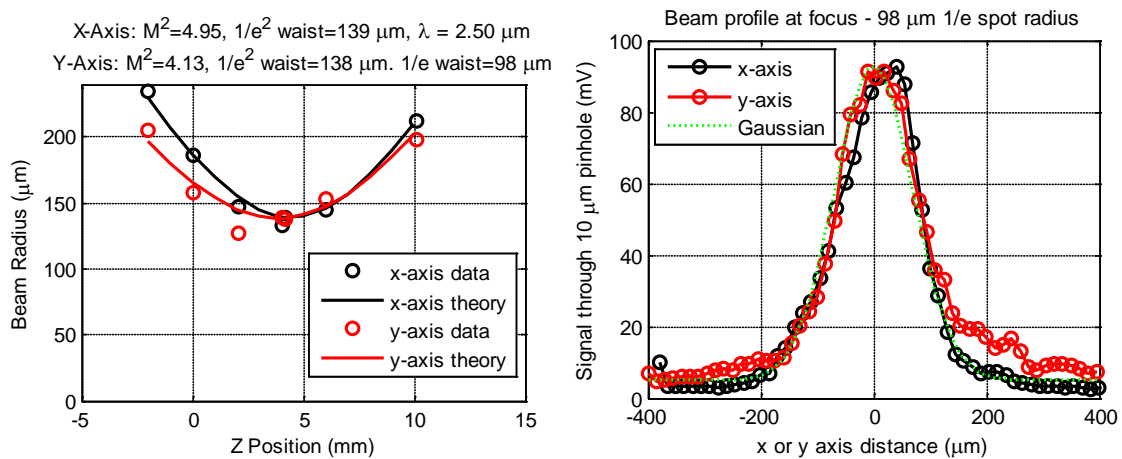
Figure 60.   Beam characterization for Ge damage test: (left) M^2 data, (right) beam profile measured in x and y axes

The relationship between the energy reflected off the pellicle and the energy delivered to the sample was calibrated by rotating the attenuator through its range of motion while recording the angle and pulse energies on Channel A and Channel B with no sample in place.

The damage spot size, site spacing and number of sites tested per fluence level were guided by ISO 11254-1 [44]. In the figures below, the damage test plans and their resulting damage grids are presented. In the test plan graphs, each circle is a damage site and the number inside indicates how many pulses were tested per site. The fluence level

91

is constant for each row and the number of pulses is constant for each column. For each

sample a rough test was conducted to find the approximate LIDT; then a final test at a

higher fluence resolution was conducted. For the germanium test, the final test plan is

given in Figure 61, and photographs of the resulting damage grid for uncoated and coated

samples are shown in Figure 62. For the GaSb test, the test plan and a photograph of the

resulting damage grid are shown in Figure 63.
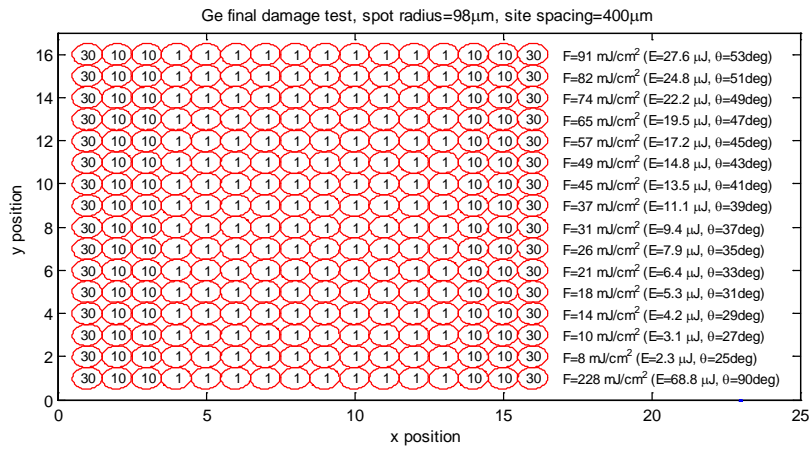
Figure 61. Ge LIDT final test plan used for tests on the uncoated and coated Ge samples
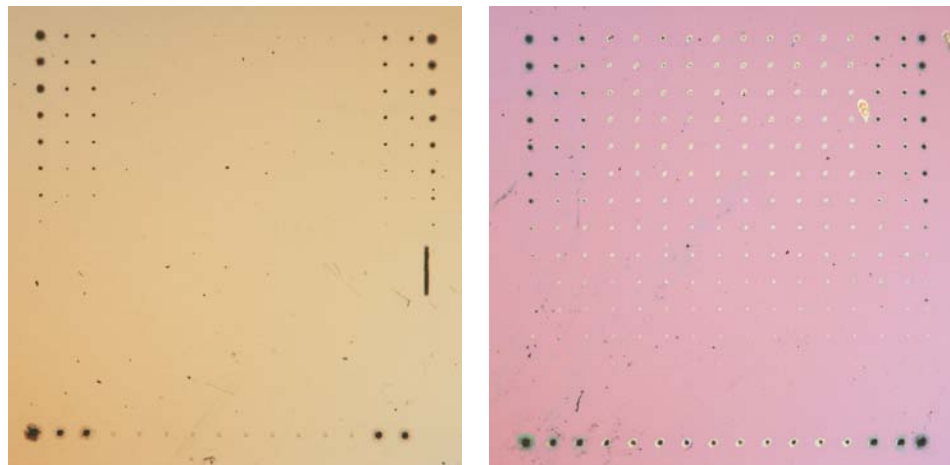
Figure 62. Ge LIDT damage grids on uncoated (left) and coated (right) surfaces

92
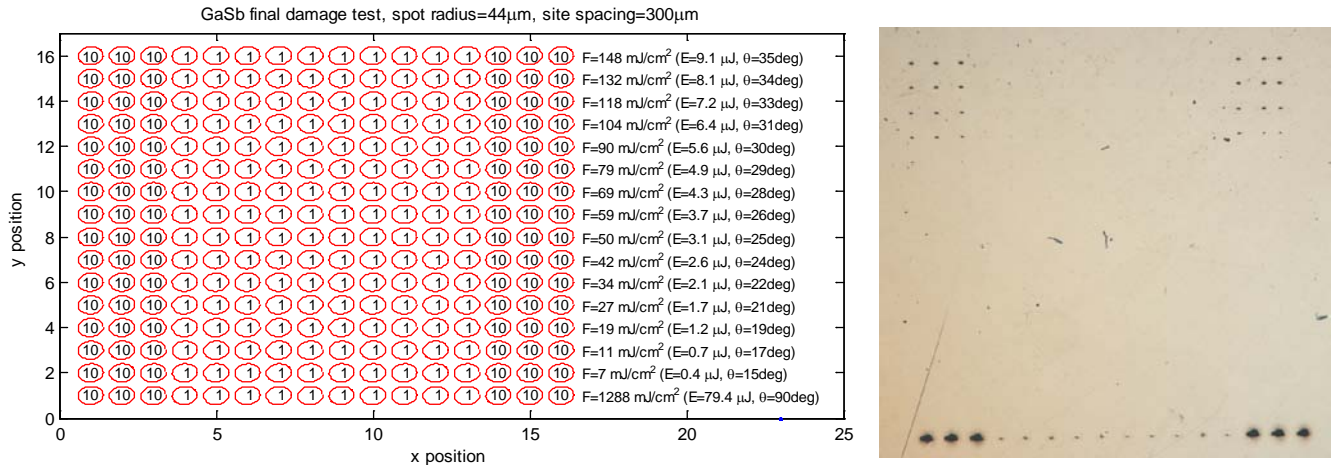
Figure 63. GaSb LIDT final test plan with higher fluence resolution and photograph of the damage grid

Damage morphologies

Damage was defined as any surface modification visible with a Nikon AZ100 bright-field optical microscope. During testing, white-light sparking indicated damage at higher fluence levels, but damage also occurred at lower fluences without visible emission. A strong dependence of damage morphology with fluence level was observed in all samples. For the 10 and 30 shot (per site) tests, evidence of significant sputtering and boiling is seen surrounding the damage site. This indicates that a thermal process is dominant in the multi-shot tests, not dielectric breakdown or ablation where the surrounding area would be clean. However, the single-shot morphologies were not conclusive.

For some multi-shot sites (Figure 64b and Figure 70c/d), horizontal streaking is noted in the damage site. This is thought to be a result of jitter in the y-axis between shots. Each site was inspected for damage, and damage statistics were collected for each fluence level (F) and number of shots (N), and these statistics were used to build the

threshold charts. The incident beam is horizontally polarized and corresponds to a left-right orientation in all photographs.

Ge uncoated damage morphologies

a) F=26 mJ/cm^2, N=30   b) F=40 mJ/cm^2, N=30   c) F=228 mJ/cm^2, N=30
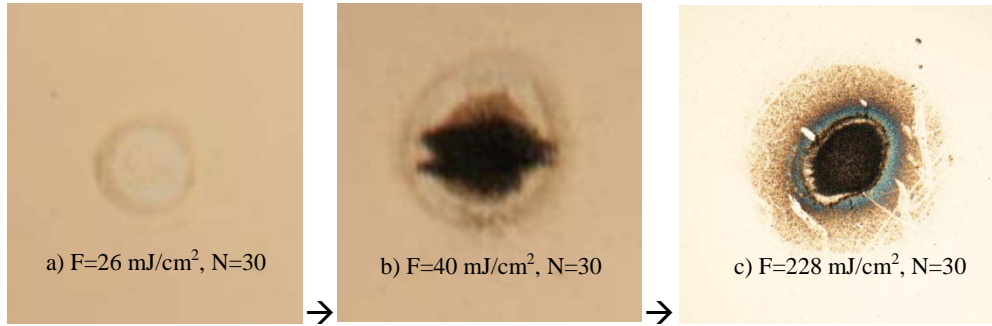
Figure 64.   Evolution of 30 shot damage threshold in uncoated germanium

a) F=26 mJ/cm^2, N=10   b) F=40 mJ/cm^2, N=10   c) F=228 mJ/cm^2, N=10
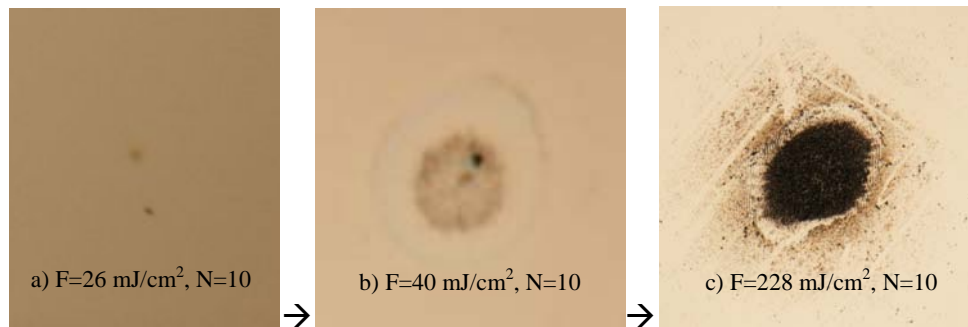
Figure 65.   Evolution of 10 shot damage threshold in uncoated germanium

a) F=37 mJ/cm^2, N=1   b) F=57 mJ/cm^2, N=1   c) F=105 mJ/cm^2, N=1   d) F=228 mJ/cm^2, N=1
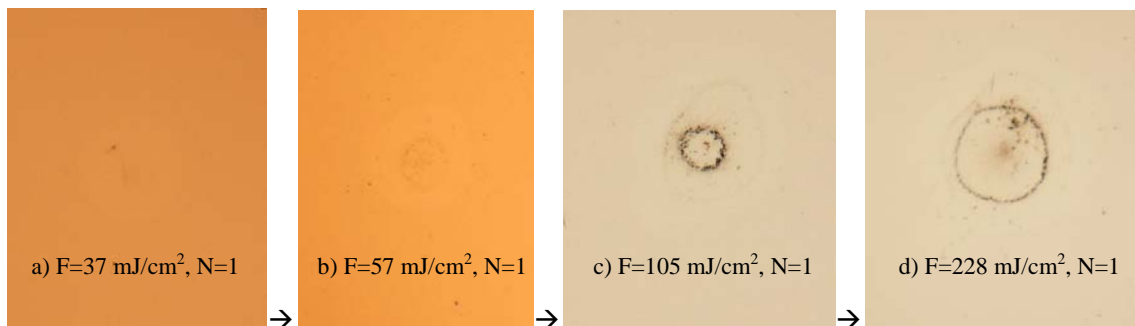
Figure 66.   Evolution of single shot damage in uncoated germanium

94

In Figure 66a, which is near the Ge single-shot LIDT of 24 mJ/cm^2, a single vertical crack is noted in all of the damage sites. It is thought to be a result of thermal stresses on the surface, and would lead to further damage with each pulse.

Ge coated damage morphologies

a) F=31 mJ/cm^2, N=30   b) F=37 mJ/cm^2, N=30   c) F=45 mJ/cm^2, N=30   d) F=82 mJ/cm^2, N=30
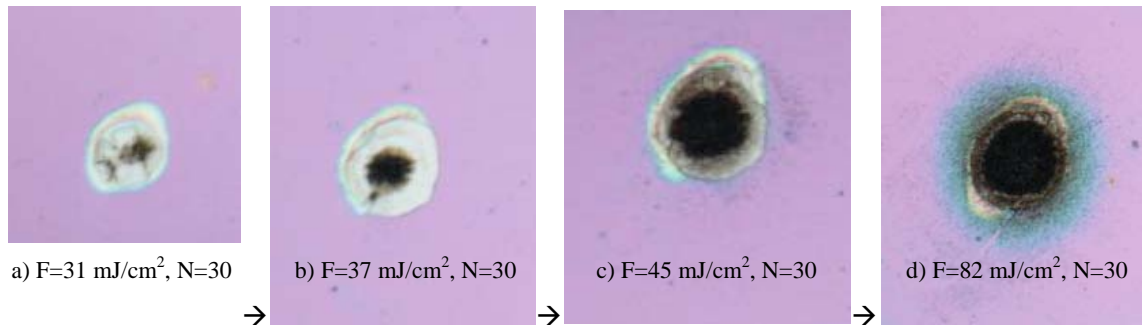
Figure 67.   Evolution of 30 shot damage in coated germanium

a) F=21 mJ/cm^2, N=10   b) F=31 mJ/cm^2, N=10   c) F=37 mJ/cm^2, N=10   d) F=82mJ/cm^2, N=10
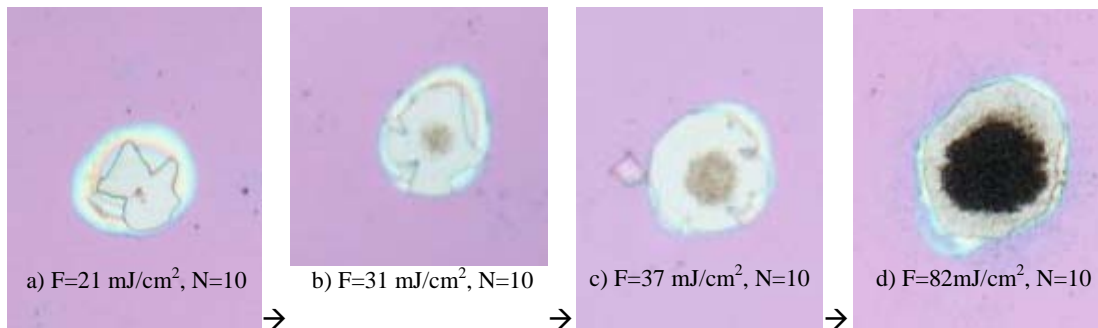
Figure 68.   Evolution of 10 shot damage in coated germanium

a) F=14 mJ/cm^2, N=1   b) F=14 mJ/cm^2, N=10
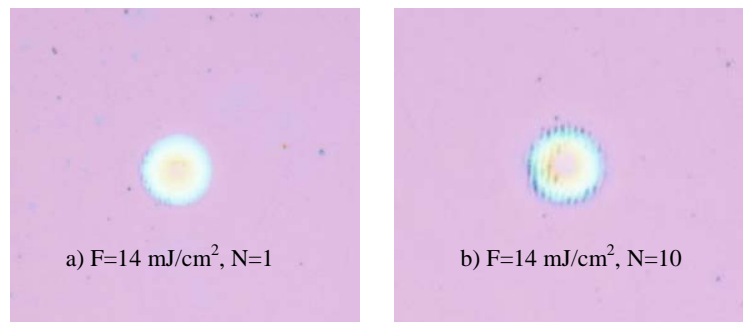
Figure 69.   Morphology near single (a) and ten (b) shot damage threshold in coated Ge

The coated Ge morphologies show a progression from both surface and coating damage to only coating damage at lower fluence/shot levels, with ejected fragments of coating visible in Figure 68c. Very close to threshold (Figure 69), the coating was ablated slightly but did not crack or fracture. This is a significant finding – that the coating has a lower damage threshold than the Ge surface. The coating reduced the Fresnel reflection from the surface to 5% from 37%, allowing a greater irradiance to be absorbed in the skin depth of the sample, which could possibly lower the surface LIDT. However, as the coating could damage without underlying surface damage, it is clear that the coating has a lower damage threshold.

GaSb damage morphology is similar to Ge, except that it requires a higher fluence level to achieve damage.

a) $F=79mJ/cm^2$, N=10 →   b) $F=90 mJ/cm^2$, N=10 →   c) $F=148 mJ/cm^2$, N=10 →   d) $F=1288 mJ/cm^2$, N=10
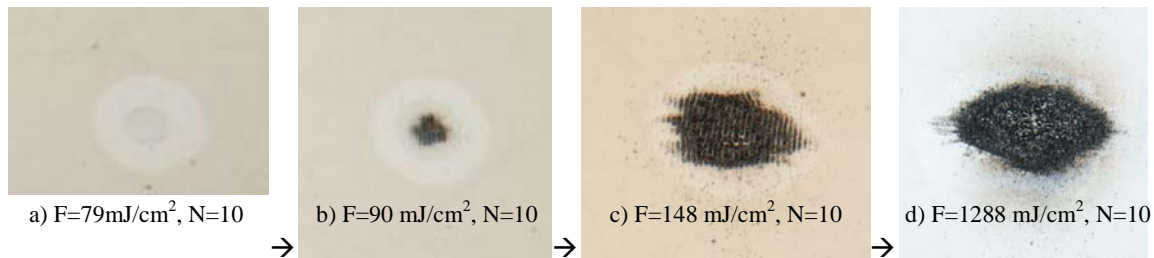
Figure 70.   Evolution of 10 shot damage in uncoated GaSb

$F=148 mJ/cm^2$, N=1
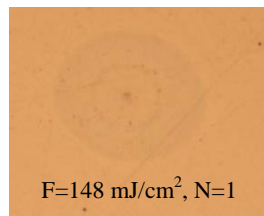
Figure 71.   Example of single shot damage in uncoated GaSb

Post-damage SEM inspection

A post-damage inspection for the picosecond damage tests was conducted on a Hitachi S-4700 Scanning Electron Microscope (SEM). Single shot damage sites were not visible on the SEM, as there was not enough surface scarring to create a charge differential. However, excellent images of the multiple shot damage sites were obtained.

Fringing oriented perpendicular to the direction of polarization was noted in the 30-shot damage sites. Using the SEM imagery, the period of fringing was measured as 2.3 μm in both Ge and GaSb, which nearly corresponds to the incident wavelength of 2.5 μm. This structure has been observed in the literature [92], and is likely a result of an interference pattern generated between the incident beam and a surface scattered wave. In this case, the surface scattered wave would originate from the reflection of the incident pulse with damage from prior shots, which reinforces the structure with each pulse.

Figure 72 shows the periodic structure in a GaSb 30 shot damage site, which shows clear evidence of melting – there are no jagged edges from thermo-mechanical stress and also no evidence of ablation.

AFIT-SEM 20.0kV 16.3mm x1.80k SE(M,0) 12/18/2009 09:29 30.0um AFIT-SEM 20.0kV 16.4mm x13.0k SE(M,0) 12/18/2009 09:33 4.00um
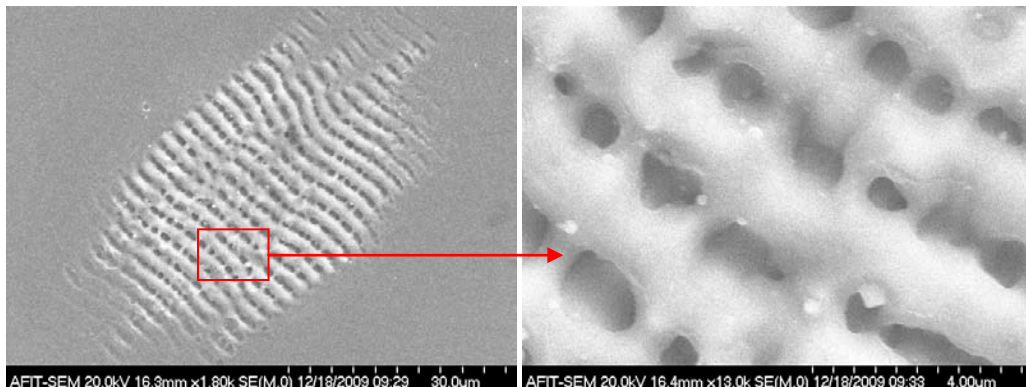
**Figure 72. SEM imagery for the GaSb sample – 30 shot damage morphology.
(left) 1800x view of the site. (right) 13,000x view showing detail of the periodic structure**

97

A 30-shot coated Ge damage site is shown in Figure 73. The inset shows jagged edges where the coating has fractured, and also the periodic structure. In the final 15,000x zoom image, 200 nm diameter molten sputter ejected from the damage site is visible – more evidence the multi-shot damage was dominated by thermal mechanisms.
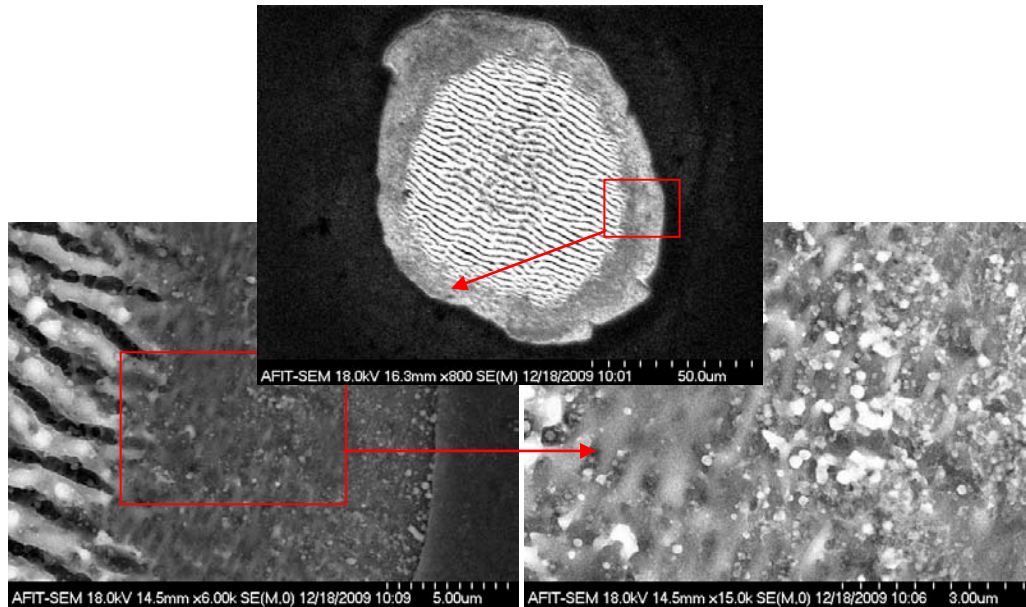
Figure 73. SEM imagery for the Ge coated sample – 30 shot damage morphology. (inset) 800x view of entire damage site. (left) 6000x view of the damage site edge showing periodic structure, molten sputter and clean line where coating is removed. (right) 15,000x view showing detail of molten sputter surrounding the damage site

Figure 74 shows an uncoated Ge sample, with a 100 μm radius circle drawn in black and offset from the site to show the damage spot size. This is nearly an identical match to the 98 μm 1/e radius of the incident beam.
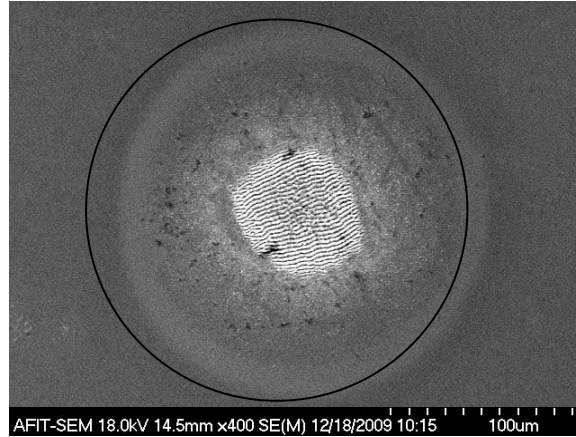
Figure 74. SEM imagery for the Ge uncoated sample – 400x view of 30 shot morphology

Picosecond damage thresholds

Picosecond damage threshold measurements are presented in this section for

uncoated GaSb, uncoated Ge and coated Ge. Using the ISO-11254 method shown in

Figure 9, the single shot threshold for GaSb is 93 mJ/cm^2 and the ten shot threshold is

65 mJ/cm^2 as measured in Figure 75.
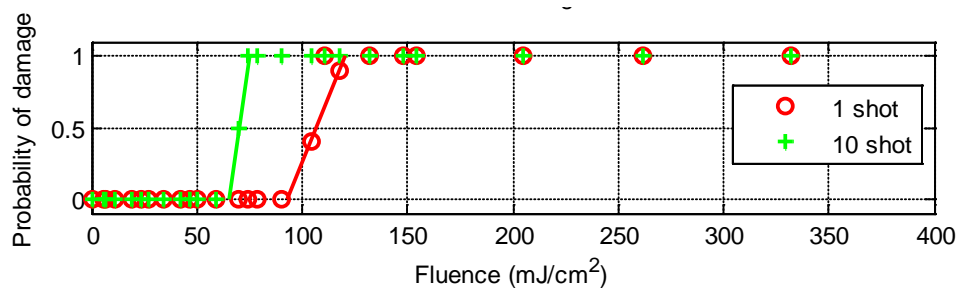
Figure 75. ps LIDT's for uncoated GaSb

The uncoated Ge single shot LIDT is 24 mJ/cm^2, the ten shot LIDT is 18 mJ/cm^2

and the 30 shot LIDT is 15 mJ/cm^2 as shown in Figure 76 (top). Finally, for the

99

aluminum oxide coating on the Ge sample, the single shot LIDT is reduced to 11 mJ/cm^2, while the ten and thirty shot LIDT coincide at 10 mJ/cm^2 as shown in Figure 76 (bottom).
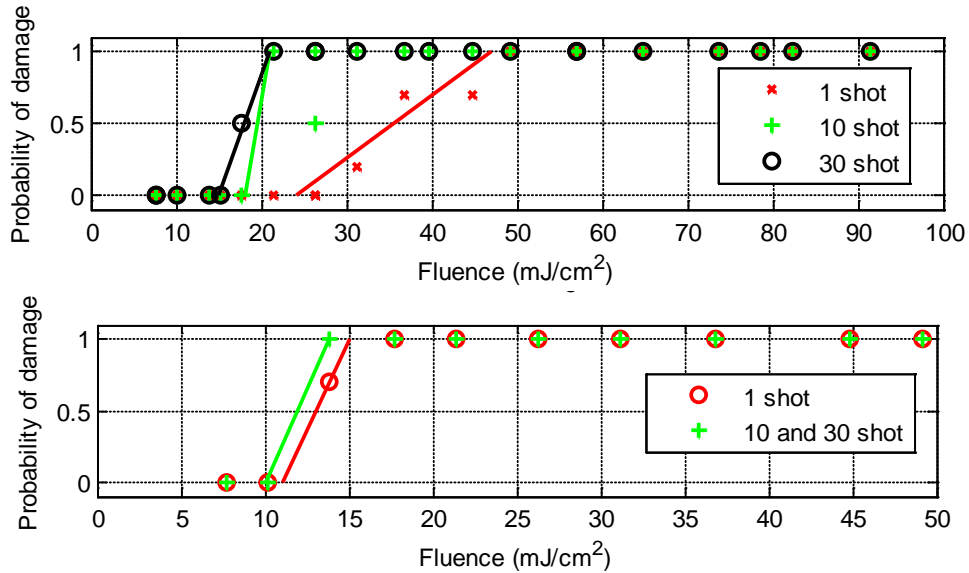
Figure 76.   ps LIDT's for uncoated Ge (top) and coated Ge (bottom)

As expected, the damage threshold decreases with an increased number of shots, as undetectable fractures from previous shots will absorb increasing amounts of energy, causing the damage to become visible. In the ps experiment, eight ps LIDT's were measured, and an LIDT uncertainty analysis follows after the ns damage test section.

Nanosecond damage experiment

In this experiment, single-pulse surface LIDT tests were conducted on GaSb, Ge and coated Ge at 2.5 μm using ns pulses from the gain-switched Cr^{2+}:ZnSe laser. The method used for the ps damage testing was followed, with an important exception. The pulse-to-pulse energy from the Schwartz Cr,Th,Ho:YAG pump laser has a ±30%

100

variation, which means the gain-switched laser has a similar variation. Therefore, the experiment was calibrated using a different method than the ps damage tests, and also ten-shot and thirty-shot damage thresholds would not be possible to assess due to this variability.

In order to accurately measure the LIDT, the pulse energy of every incident pulse was recorded using the pellicle beam splitter and an energy head. Pinhole scans along x and y axes were taken to measure a perfect Gaussian 136 μm spatial profile of the beam after focusing with a coated f = 15 cm lens.

For each sample tested, the test plan and photograph of all test sites are shown in Figure 77 through Figure 79. In the test plans, a red circle indicates that the site was found to be damaged, while a black circle shows that no damage was present. The text inside the circles is either the fluence from a single pulse (J/cm^2), or '20x' which indicates that 20 pulses at maximum fluence were incident to delineate the test grid.
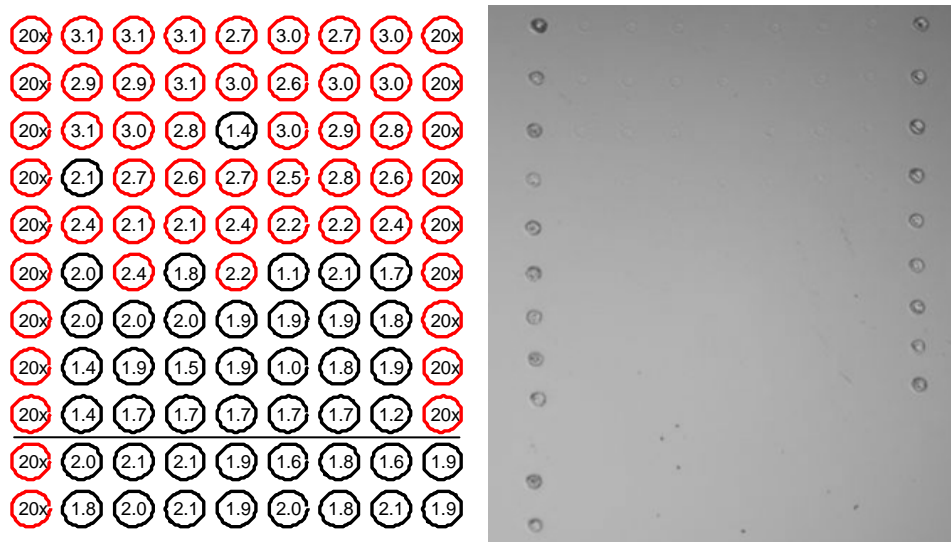
Figure 77. Uncoated Ge test plan (left) and photograph of damage test (right). The number inside the test plan circles is the single pulse incident fluence in J/cm^2
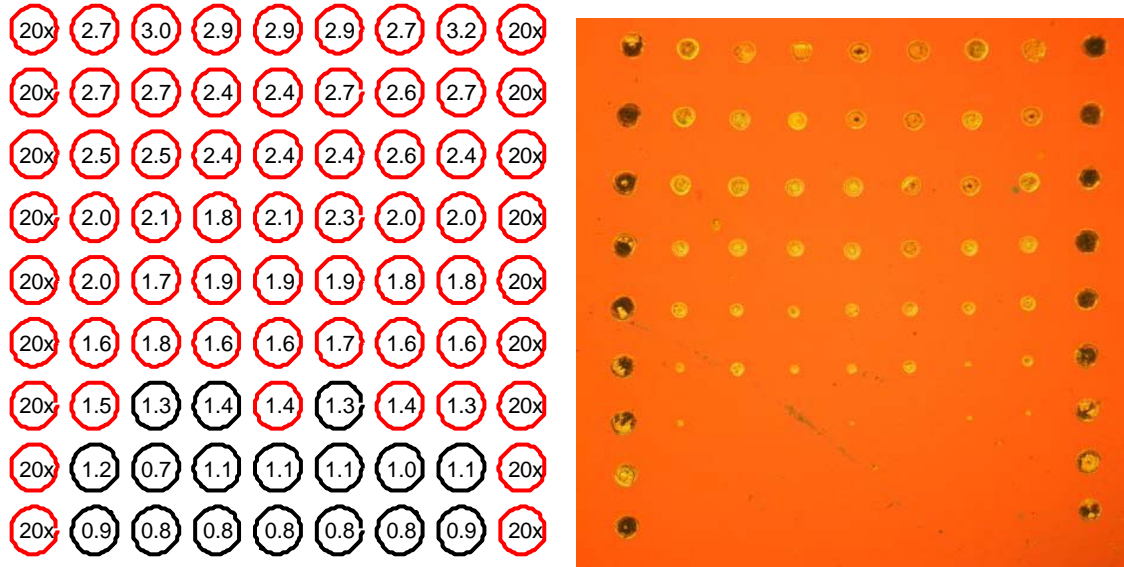
Figure 78. Coated Ge test plan and photograph of damage test
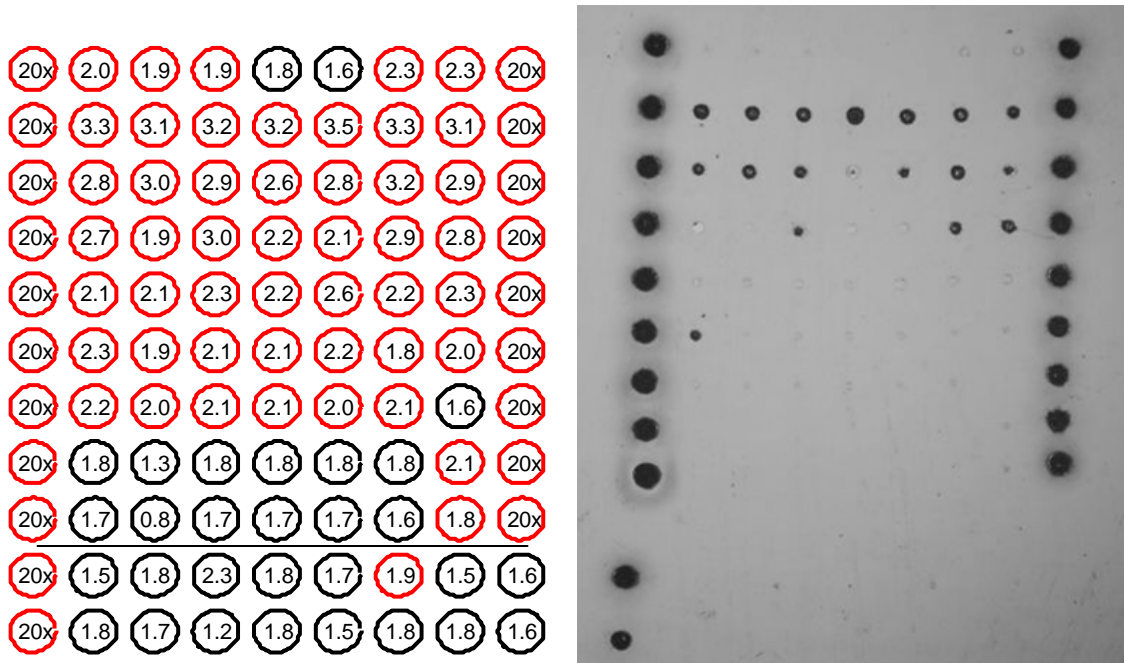
Figure 79. GaSb test plan and photograph of damage test

In contrast with the ps damage tests, GaSb damaged at a lower fluence with ns

pulses, which will be further discussed in Chapter 5.

Ge damage morphology

As in the ps damage tests, damage was defined as any visible surface modification visible using a Nikon AZ100 bright-field optical microscope. In the morphology examination, damage statistics were collected for each fluence level (F) and number of shots (N). In the ns tests, the Ge damage morphology did not exhibit dramatic scarring or boiling, only surface melting that does not have good contrast on the microscope capture images, as shown in Figure 80a. Melting was easily detected by varying the fine z-axis control on the microscope as any surface modification would defocus at a different point than the sample surface.

a) F=3.1 mJ/cm^2, N=1   b) F=3.1 J/cm^2, N=20
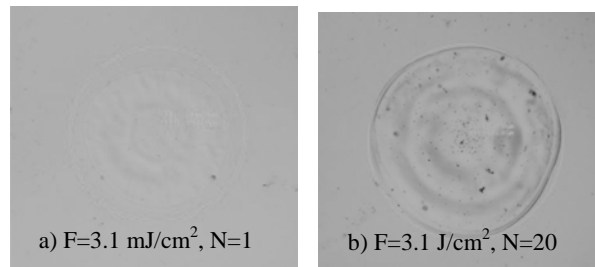
Figure 80.   Examples of single and multiple shot damage in uncoated germanium

For coated Ge, the damage sites in Figure 81 show a progression from both surface and coating damage to only coating damage at lower fluence levels. At fluences very close to the threshold of 1.25 J/cm^2 (Figure 81a), the coating would be ablated slightly but not crack or fracture. This confirms the observation from the ps coated damage test that the coating has a lower damage threshold than the material surface.

103
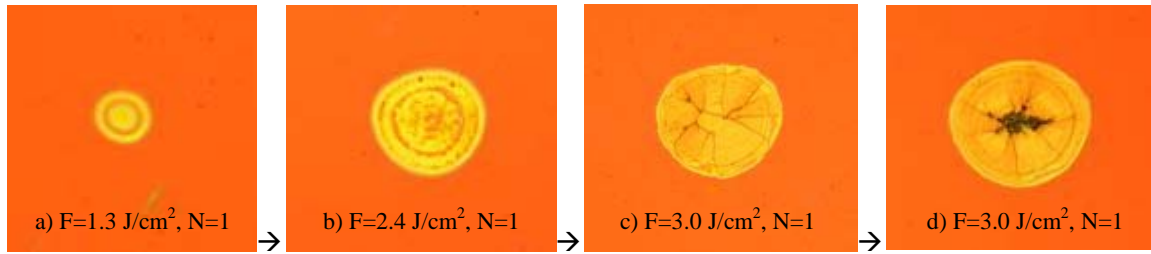
Figure 81.   Evolution of single shot damage in coated germanium

GaSb damage morphology

The lower melting point of GaSb caused greater surface modifications than found in Ge, as shown in Figure 82 for single shot damage sites. At a fluence near the threshold of 1.75 J/cm^2, a series of thermal fractures was visible in Figure 82a which then proceed to smoothly melt at higher fluences.
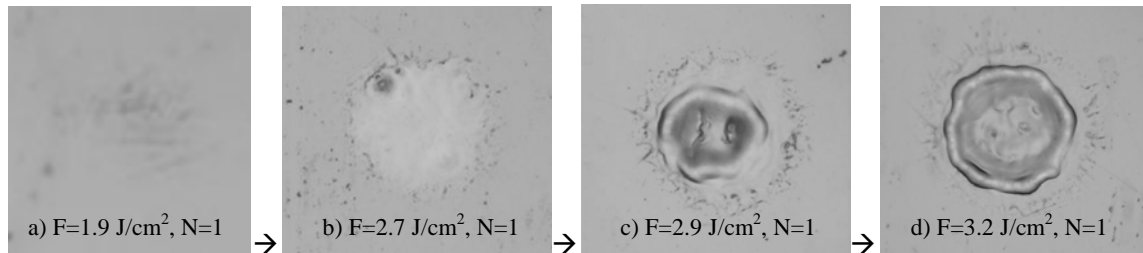
Figure 82.   Evolution of single shot damage in uncoated GaSb

Nanosecond damage thresholds

Nanosecond damage threshold measurements are presented in this section for uncoated GaSb, uncoated Ge and coated Ge. For uncoated GaSb, Figure 83 (top) displays the actual binary damage data (clean or damaged) for each incident pulse fluence. In the bottom of the figure the shots are binned into 90 mJ divisions to allow a damage probability to be assigned to each division. Using the ISO 11254-1 method, the GaSb single shot LIDT for 68 ns pulses is determined to be 1.75 J/cm^2.

104
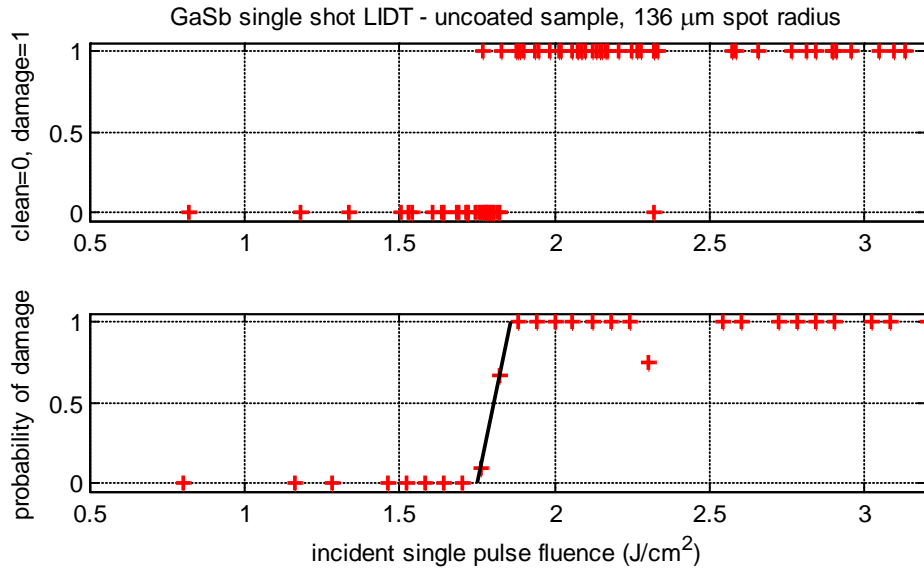
Figure 83. ns LIDT for GaSb

Figure 84 (top) shows the single shot LIDT for uncoated Ge to be 1.94 J/cm^2, and the bottom graph measures the single shot LIDT for the aluminum oxide coating on Ge as 1.25 J/cm^2.
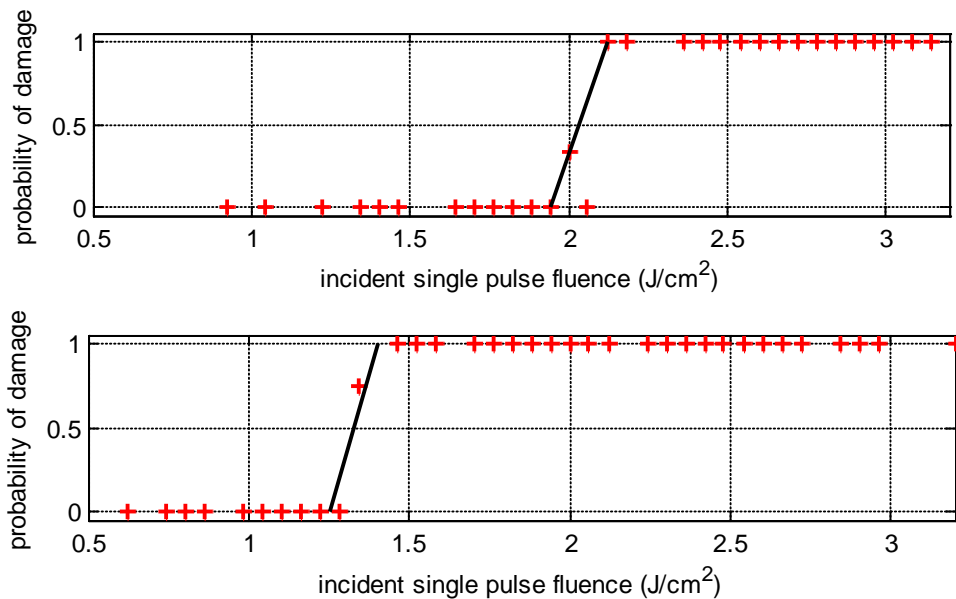
Figure 84. Ge ns LIDT for uncoated surface (top) and coated surface (bottom)

Uncertainty analysis

The uncertainty in reported LIDT fluence is calculated using the same propagation of errors method as the NLA coefficients. The fluence F of a laser pulse is defined as $F = E/\pi r^2$ and will have uncertainties in pulse energy and measured spot radius. The incident pulse energy is measured on Laser Precision RJ-735 heads which are calibrated to 5% accuracy and a 0.5 µJ noise level. The spatial profiles were measured with a 10 µm pinhole and the resulting error of 3-6 µm is calculated from the quality of the Gaussian fit at $1/e$ irradiance. The expression for uncertainty in fluence ΔF that results from these errors is defined below, along with the required partial derivatives for energy and spot radius:

$$\Delta F^2 = \left(\frac{dF}{dE}\right)^2 \Delta E^2 + \left(\frac{dF}{dr}\right)^2 \Delta r^2 \quad \Rightarrow \quad \left(\frac{dF}{dE}\right) = \frac{1}{\pi r^2} \quad \left(\frac{dF}{dr}\right) = \frac{-2E}{\pi r^3}$$

As in the NLA analysis, cross-variance is excluded as an error in pulse energy will not induce an error in spot radius. Using the propagation of errors method, the fluence uncertainty ΔF is calculated for each experiment and is presented in Table 16.

Table 16. Parameters used to calculate uncertainty in LIDT fluence

Material / Pulse width	Spot radius	Spot radius error	LIDT pulse energy	Energy error	LIDT Fluence F	± ΔF
Ge / 10.1 ps	98 µm	6 µm	7 µJ	0.5 µJ	24 mJ/cm^2	**3.3 mJ/cm^2**
GaSb / 10.1 ps	44 µm	3 µm	6 µJ	0.5 µJ	93 mJ/cm^2	**16 mJ/cm^2**
Ge / 68 ns	136 µm	5 µm	1.13 mJ	62 µJ	1.94 J/cm^2	**0.18 J/cm^2**
GaSb / 68 ns	136 µm	5 µm	1.02 mJ	58 µJ	1.75 J/cm^2	**0.17 J/cm^2**

Modeling of damage thresholds

       In this section, the scaling of LIDT with pulse width is explored along with the prediction of temperature rise from absorption leading to surface melting. The FD model is used to predict single pulse LIDT due to linear and nonlinear absorption, and the variation due to $\alpha(T)$ is also studied.

Pulse width scaling

       Pulse width (τ_p) scaling of laser-induced damage thresholds (LIDT) typically possess a τ_p^x dependence where *x* ranges from 0.4 – 0.5 [35]. When using a $\tau_p^{0.5}$ value of pulse width scaling, the Ge $\tau_p = 10$ ps LIDT measurement (0.024 J/cm^2) is in excellent agreement with the $\tau_p = 68$ ns LIDT (1.94 J/cm^2 vs. 1.85 J/cm^2 predicted). Using this method, GaSb had a $\tau_p^{0.34}$ dependence on pulse width. When using damage thresholds, this relationship shows why the LIDT pulse width is a critical detail, as scaling effects could be detrimental to a design. Pulse width scaling of laser-induced damage is modeled from linear and nonlinear absorption in the next two sections, which show significant differences between the two mechanisms.

FD modeling of linear absorption leading to damage

       In order to compare the effects of linear and nonlinear absorption, LIDT are first modeled where linear absorption is the only source of free carriers that induce a temperature rise. This case is not experimentally tested. An iteration routine was used with the FD model to find the pulse fluence that will cause surface melting. The pulse width was varied from fs to μs, and the laser-induced damage threshold (LIDT) predicted from linear absorption is graphed in Figure 85. The threshold curve is dominated by the free carrier relaxation time of $\tau_R = 10$ ns (10^{-8} s) in this case. The inset of Figure 85

illustrates this recombination effect for fused silica, where the dominant τ_R is much

shorter at 0.5 ps.
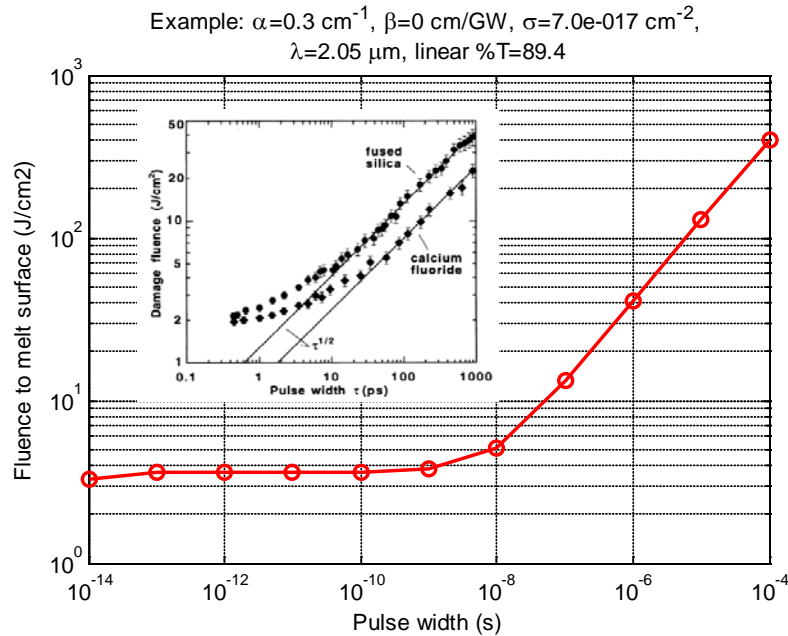
Figure 85. Predicted LIDT fluence from FD model for linear absorption. Inset shows LIDT variation for Si [35] where the dominant recombination time is 0.5 ps [36]

For pulse widths shorter than τ_R, no carriers can relax during the pulse and the

surface melts at a constant energy level, according to *energy = mass * specific heat * ΔT*.

If the pulse width is greater than τ_R, free carriers can relax during the pulse, requiring

more energy to melt the surface as the pulse width increases.

FD modeling of nonlinear absorption leading to damage

The LIDTs from nonlinear absorption are graphed in Figure 86 over the same

range of pulse widths. There are three factors explored below which cause the LIDT due

to nonlinear absorption to vary substantially from the linear absorption graph.

108

The first factor is based on nonlinear vs. linear absorption. For a given fluence level, peak irradiance rises as the pulse becomes shorter, and NLA $\sim I^2$ while $\alpha \sim I$. This allows the LIDT to continue to decrease with shorter pulse width, while LIDT due to linear absorption remains constant if τ_p is shorter than the dominant recombination time.
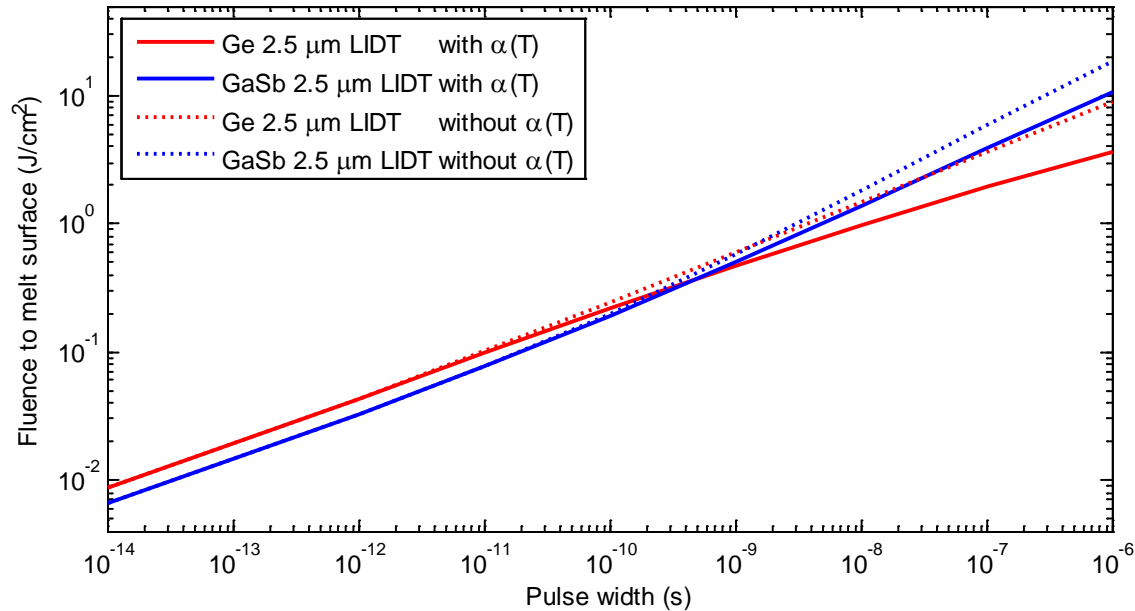
Figure 86. Nonlinear absorption - predicted LIDT fluence for Ge and GaSb using
*N***-dependent carrier recombination. Dashed lines = no** *α(T)***, solid lines =** *α(T)* **included**

The second factor is that free carrier dependent τ_R values are implemented, which eliminates the sharp bend in the curve from Figure 85 as the impact of τ_R gradually becomes significant. The third factor is the implementation of temperature dependent linear absorption. The variation due to $\alpha(T)$ is shown in Figure 86 where the solid lines include the effect and the dashed lines do not. It is predicted that $\alpha(T)$ reduces the LIDT only for pulses greater than 100 ps in duration, and can reduce the LIDT by a factor of two for a µs pulse width. As shown in Figure 85, the effect of linear absorption decreases

109

with longer pulse widths as recombination reduces the number of free carriers. When $α(T)$ is modeled, this trend is countered as ever-increasing numbers of free carriers are generated from $α(T)$ as the temperature rises. Pulse width scaling of LIDT using the NLA coefficients measured in this work are presented along with experimentally determined ns and ps thresholds in Chapter 5.

Chapter 5.   Conclusions

This chapter summarizes the main results of this research effort, draws general conclusions in the areas of mid-IR laser design and effects analysis, and provides recommendations for future work in these fields.

Research Summary

This research measured the nonlinear absorption coefficients and laser-induced damage thresholds (LIDT) of Ge and GaSb. Additionally, it was necessary to develop a pulsed Cr^{2+}:ZnSe 2.5 μm wavelength laser to conduct these measurements, as prior lasers at this wavelength possessed insufficient pulse energy to induce nonlinear absorption or damage these materials. Using a Brewster-cut gain medium, a ns pulse width, 3.1 mJ pulse energy laser was created with record peak power. For the first time, NLA coefficients in Ge and GaSb at 2.05 μm and 2.5 μm were measured and modeled using the single-pulse finite difference model developed in this work. Finally, those NLA coefficients were used to predict damage thresholds, which were experimentally tested at 2.5 μm, also for the first time. The experimental results from this research are given in Table 17 and Table 18. In Table 17, the uncertainty bounds are the maximum variation in β and σ that resulted from the uncertainty analysis that was presented in Table 15.

Table 17. NLA coefficients measured in Ge and GaSb at two mid-IR wavelengths

	Ge		GaSb	
Wavelength (nm)	2050	2500	2050	2500
β (cm/GW) value *(lower bound – upper bound)*	71 *(45-96)*	68 *(57-95)*	64 *(49-90)*	119 *(86-148)*
σ (x10^{-16} cm^2) value *(lower bound – upper bound)*	4.9 *(3.0-9.4)*	9.0 *(5.7-12.5)*	3.8 *(2.5-5.4)*	6.5 *(5.0-9.8)*

111

www.manaraa.com

Table 18. Single-shot and multiple-shot LIDT measured in Ge and GaSb at a wavelength of 2.5 µm, including key parameters

Sample	Pulse width	Number of shots (N)	LIDT (mJ/cm^2)	spot radius at 1/e (µm)	Peak irradiance at LIDT (GW/cm^2)	Pulse energy at LIDT (µJ)
GaSb uncoated	10.1 ps	1	93 ± 16	44	4.97	5.5
GaSb uncoated	10.1 ps	10	65 ± 16	44	3.36	3.7
Ge uncoated	10.1 ps	1	24 ± 3.3	98	1.24	6.8
Ge uncoated	10.1 ps	10	18 ± 3.3	98	0.932	5.1
Ge uncoated	10.1 ps	30	15 ± 3.3	98	0.776	4.2
Al$_2$O$_3$ coating on Ge	10.1 ps	1	11 ± 3.3	98	0.569	3.1
Al$_2$O$_3$ coating on Ge	10.1 ps	10 & 30	10 ± 3.3	98	0.517	2.8
GaSb uncoated	68 ns*	1	1750 ± 170	136	0.015	1020
Ge uncoated	68 ns*	1	1940 ± 180	136	0.017	1130
Al$_2$O$_3$ coating on Ge	68 ns*	1	1250 ± 180	136	0.011	730

* gain-switched pulse

Nonlinear Absorption Conclusions

The NLA coefficients reported in Table 17 are now compared to literature values and theoretical predictions. Figure 87 compares experimentally measured Ge two-photon absorption coefficients with literature values, and the Van Stryland prediction is overlaid as the green curve. The values from this work are in excellent agreement with the prediction and are in reasonable agreement with the only literature value that also used free-carrier absorption in their NLA fit (Rauscher 1997).

112
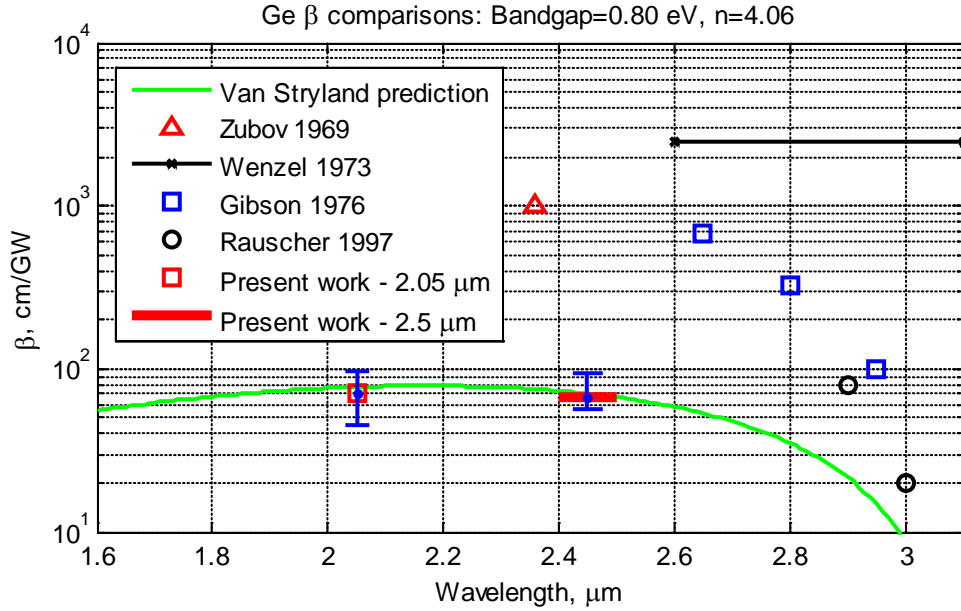
Figure 87. **Ge dispersion of β in present work and literature values, with a theoretical overlay presented in green**

For GaSb, the two photon absorption coefficients are compared in Figure 88, and the 2.5 μm value is in excellent agreement with the Van Stryland prediction. There is a discrepancy between the GaSb 2.05 μm value of $\beta = 64$ cm/GW and the Van Stryland prediction of 111 cm/GW. This variation may be explained with a GaSb full band-structure prediction created by SRI International which predicts a 2.05 μm β of 41 cm/GW, which is closer to the value reported in this work. This model is overlaid as the blue line in Figure 88. It is noted that neither model provides an excellent fit to both data points; however the uncertainty range of each model may intersect the uncertainty range of the reported values.

The Akmanov 1996 GaSb study at 2.94 μm used an estimate of $\sigma = 2 \times 10^{-17}$ cm^2 which is over an order of magnitude smaller than the values reported in this work (3.8×10^{-16} cm^2 and 6.5×10^{-16} cm^2). This results in a much higher fit to β, which is

113

expected due to the inverse relationship between β and σ that is visible in the error

surfaces of Figure 51 on page 81.
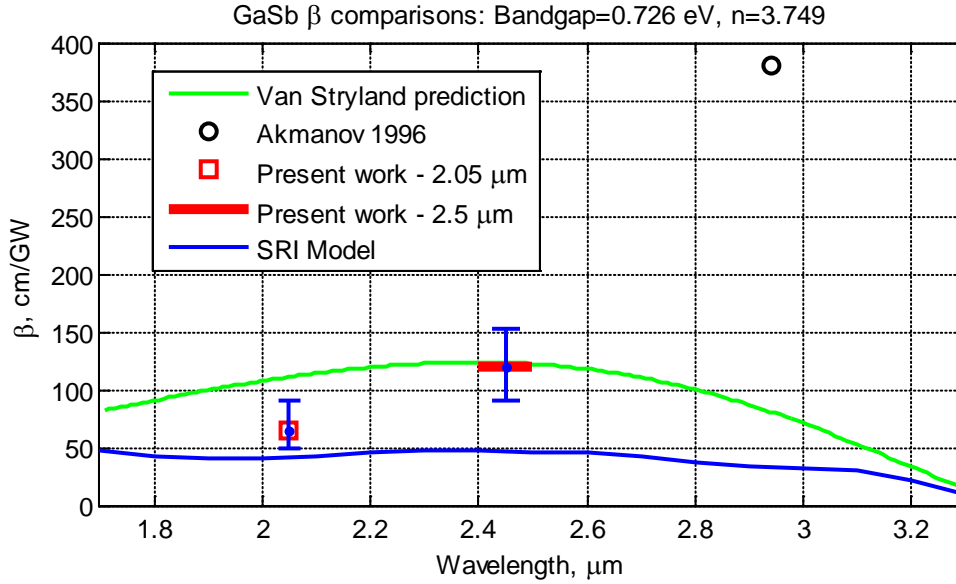
Figure 88.   GaSb dispersion of β in present work and literature values, with a theoretical overlay presented in green and blue

The σ values reported for Ge and GaSb agree with the trend of one wavelength

scaling theory, whose comparison is shown in Figure 89. In this theory, absorption due

to free carriers (α) is given as $\alpha(\lambda) = \frac{\lambda^2 N e^3}{4\pi^2 c^3 n_o \epsilon_o m_{eff}^2 \mu}$ [26], showing that σ is proportional

to λ^2, as α is directly proportional to σ in the expression $\alpha = \sigma N$.

This theory is now applied to the σ values obtained in this work, where σ is

predicted to rise by a factor of $2.5^2 - 2.05^2 = 2.04$. There is good agreement in the

measured values between 2.05 and 2.5 μm, as Ge σ rises by a factor of 1.73 and GaSb

σ rises by a factor of 1.65.

114
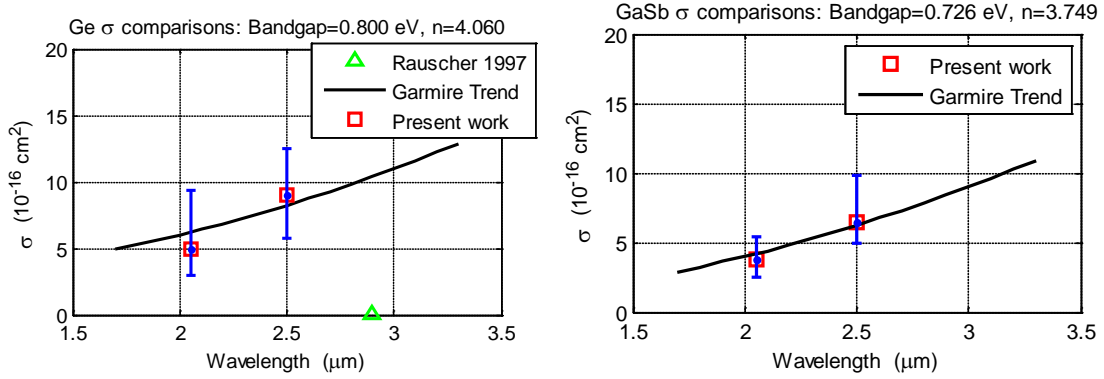
Figure 89. Dispersion of σ for Ge (left) and GaSb (right), including theoretical trend lines and a literature value

Another study [25] calculates $\sigma(\lambda)$ using second order perturbation theory to show that the variation of free carrier absorption with wavelength has higher complexity, as shown for InAs and HgCdTe in Figure 90.
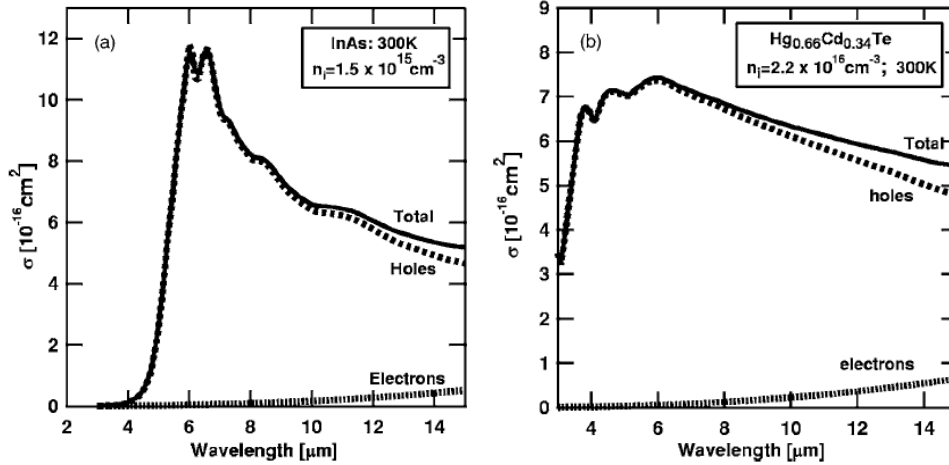
Figure 90. Predicted dispersion of free carrier absorption with wavelength in InAs (left) and HgCdTe (right) [25]

115

Laser-Induced Damage Study Conclusions

Figure 91 presents measured single pulse LIDT's (ps and ns) for these two materials overlaid with predicted thresholds from the FD model. These predictions use no fitting parameters – only measured NLA coefficients, measured beam parameters, carrier density dependent recombination times from the literature and measured temperature dependent linear absorption. The calculated error bars are not shown as they are smaller than the symbol shapes due to the log-log presentation of Figure 91.

Ge: β=68 cm/GW, σ=9.0e-016 cm^{-2}, B$_{rad}$=6.4e-014 cm^3/s, Auger=1.0e-030 cm^6/s, %T=46.3, Melt=1210 °K
GaSb: β=119 cm/GW, σ=6.5e-016 cm^2, B$_{rad}$=1.2e-009 cm^3/s, Auger=5.0e-030 cm^6/s, %T=44.0, Melt=985 °K

Figure 91. Predicted LIDT fluence for Ge and GaSb using measured NLA coefficients, markers indicate experimentally determined LIDT fluences

The range of pulse widths that are modeled in Figure 91 are bounded by free carrier diffusion and dielectric breakdown, which are effects not included in the FD model. Using free carrier diffusion values from Table 11, a diffusion length of 100 μm

116

was selected as the constraint on the longest pulse width modeled. This corresponds to τ_p = 500 ns for Ge and τ_p = 350 ns for GaSb. As the pulse width is decreased, eventually a transition to dielectric breakdown will occur. The shortest pulse width modeled corresponds to the predicted Keldysh theory transition to dielectric breakdown [37,38] using Eq. 11, which was on the order of τ_p = 300 fs for these materials.

The LIDT values are in good agreement with theory with one exception - at a ps pulse width, Ge damaged at a fluence level five times less than predicted. Possible causes for this discrepancy include field enhancement and thermalization, but not dielectric breakdown, which is predicted only if the irradiance were increased by an order of magnitude. The incident electric field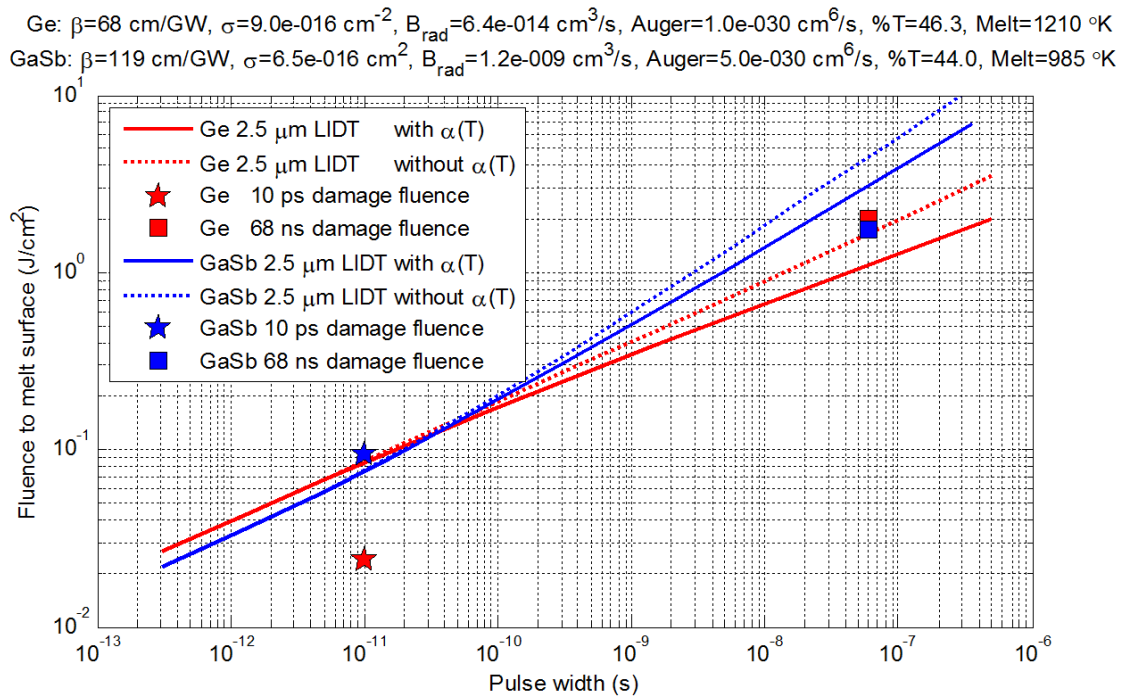 at surface defects is known to be locally enhanced at a rate proportional to n^4 [83], giving Ge a 35% greater enhancement over GaSb. This calculated enhancement is only based on the difference in n, and the 20% greater surface roughness of Ge given in Table 8 will further magnify the field.

While the hot carrier thermalization of Ge was not modeled as it was beyond the scope of this study, its non-equilibrium phonon decay time of 4 ps could certainly contribute towards a lower LIDT for a 10 ps pulse width [95].

For both pulse widths, the aluminum oxide coating on the Ge sample had a lower damage threshold than the uncoated sample. However, this simple coating was optimized for transmission and not for high fluence levels. There are several ways to engineer a coating to increase the damage threshold, as detailed in the results of the annual coating competition held at the Boulder Damage conference. In 2008 the winner had an LIDT of 125 J/cm^2 [93] for 5 ns pulses, compared with a best-of-class LIDT of only 1 J/cm^2 for

180 fs pulses in the 2009 competition [94], which further reinforces the pulse width scaling theory for LIDT.

Future Work

The nonlinear absorption and damage study could be expanded by performing experiments at additional pulse widths and wavelengths. This would allow a better understanding of the scaling properties and modeling efforts that describe two photon absorption [23,24], free carrier absorption [25,26] and single-pulse laser-induced damage thresholds [35]. Testing damage thresholds at pulse widths of 100 fs, 1 ps and 1 ns would allow the transition to dielectric breakdown to be further studied and comparisons made between its onset in an indirect bandgap vs. direct bandgap material.

The pulse energy of the gain-switched Cr^{2+}:ZnSe laser is currently limited by the damage threshold of the optics, as one of the optics has started to damage at 13 mJ pump energy, which corresponds to a fluence of 2 J/cm^2. If the resonant mode size were expanded using custom optics, the pump mode size could be increased. This would in turn decrease the fluence levels, which would allow pump pulse energies closer to the 74 mJ maximum to be explored. Another limitation to pump power is Cr^{2+}:ZnSe crystal size, whose maximum dimension is currently limited by the diffusion doping process. If the hot pressed ceramic method of crystal manufacturing [65] is further refined, larger crystals, mode areas and pulse energies are possible. Finally, wavelength tunability could be explored using a grating, which would minimize the cavity loss for a narrow bandwidth of frequencies.

118

Bibliography

1. S. T. Fiorino, R. J. Bartell, M. J. Krizo, G. L. Caylor, K. P. Moore, T. R. Harris, and S. J. Cusumano, "A first principles atmospheric propagation & characterization tool-the laser environmental effects definition and reference (LEEDR)," in *SPIE Atmospheric Propagation of Electromagnetic Waves II* 2008.

2. A. L. Schawlow and C. H. Townes, "Infrared and optical masers," *Physical Review*, vol. 112, pp. 1940-1949, 1958.

3. T. H. Maiman, "Stimulated optical radiation in ruby," *Nature*, vol. 187, pp. 493-494, 1960.

4. S. B. Mirov, "Recent Advances in Cr^{2+} and Fe^{2+} Doped Mid-IR Laser Materials," in *Conference on Lasers and Electro-Optics/Quantum Electronics and Laser Science Conference and Photonic Applications Systems Technologies*: Optical Society of America Technical Digest CD, paper CFW1, 2008.

5. A. Vogel, "Nonlinear absorption: intraocular microsurgery and laser lithotripsy," *Physics in Medicine and Biology*, vol. 42, pp. 895-912, 1997.

6. E. W. Van Stryland, H. Vanherzeele, M. J. Soileau, A. L. Smirl, S. Guha, and T. F. Boggess. "Two-photon absorption, nonlinear refraction, and optical limiting in semiconductors." *Opt. Engr.*, 24(4):613-623, 1985

7. T. Hallberg, L. Sjöqvist, and S. Svensson, "Protection of Mid-Infrared Sensors Against Laser Radiation," *Swedish Defence Research Agency*, 2001.

8. F. Bartoli, L. Esterowitz, M. Kruer, and R. Allen, "Irreversible laser damage in IR detector materials." *Applied Optics*, vol. 16: *OSA*, 1977, pp. 2934-37.

9. M. Kruer, L. Esterowitz, R. Allen, and F. Bartoli, "Thermal models for laser damage in InSb photovoltaic and photoconductive detectors." *Infrared Physics* vol. 16, 1976, pp. 375-384.

10. H. B. Sun and S. Kawata, "Two-photon photopolymerization and 3D lithographic microfabrication," in Advances in Polymer Science: *Springer*, 2004, pp. 169-273.

11. M. Samoc *et. al.*, "Nonlinear absorption: materials and mechanisms," in Proceedings of the Symposium on Photonics Technologies for 7th Framework Program, Wroclaw, 2006.

12. R. A. Sacks *et. al*., "Laser energetics and propagation modeling for the NIF," *Journal of Physics,* vol. 112, p. 032024, 2008.

13. B. Canaud, X. Fortin, N. Dague, and J. L. Bocher, "Laser Mégajoule irradiation uniformity for direct drive," *Physics of Plasmas*, vol. 9, p. 4252, 2002.

14. M. Göppert-Mayer, "über Elementarakte mit zwei Quantensprüngen" Dissertation: *University of Göttingen*, 1931.

15. W. Kaiser and C. G. B. Garrett, "Two-Photon Excitation in CaF_2: Eu^{2+}." *Physical Review Letters*, vol. 7: *APS*, 1961, pp. 229-231.

16. S. Guha, L. P. Gonzalez, J. O. Barnes, and S. Krishnamurthy, "Optical Nonlinearities and Charge-Carrier Lifetimes in Semiconductors--Experiment and Theory," *Air Force Research Laboratory Publication*, 2006.

17. P. Klocek, Handbook of Infrared Optical Materials: *CRC Press*, 1991.

18. B. G. Streetman, "Solid-state Electronic Devices", 3rd Edition, *Prentice Hall*, 1990

19. D. A. Reis, K. J. Gaffney, G. H. Gilmer, and B. Torralva, "Ultrafast Dynamics of Laser-Excited Solids." *MRS Bulletin*, vol. 31, 2006, p. 601.

20. L. P. Gonzalez, "Investigation of Near Bandgap Optical Nonlinearities in Semiconductors", PhD Prospectus, *University of Dayton*, 2007.

21. S. Krishnamurthy, Z. G. Yu, S. Guha, and L. Gonzalez, "High irradiance light propagation in InAs." *Applied Physics Letters*, vol. 89: *AIP*, 2006, p. 161108.

22. M. Sheik-Bahae and M. P. Hasselbeck, "Third-order optical nonlinearities," in OSA Handbook of Optics, Chapter 17. vol. 4: *OSA*, 2000.

23. B. S. Wherrett, "Scaling rules for multiphoton interband absorption in semiconductors." *JOSA B*, vol. 1: *OSA*, 1984, pp. 67-72.

24. E. W. Van Stryland, M. A. Woodall, H. Vanherzeele, and M. J. Soileau, "Energy band-gap dependence of two-photon absorption," *Optics Letters*, vol. 10, pp. 490-492, 1985.

25. S. Krishnamurthy, Z. G. Yu, L. P. Gonzalez, and S. Guha, "Accurate evaluation of nonlinear absorption coefficients in InAs, InSb, and HgCdTe alloys." *J. Appl. Phys.*, vol. 101: *AIP*, 2007, p. 113104.

26. E. Garmire, Robert K. Willardson, Alan Kost, Eicke R. Weber, "Nonlinear Optics in Semiconductors", *Academic Press*, 1998

27. Sloanes, T. J., "Measurement and Application of Optical Nonlinearities in Indium Phosphide, Cadmium Mercury Telleride and Photonic Crystal Fibres", *University of St. Andrews Dissertation*, (2009)

28. B. V. Zubov, L. A. Kulevskii, et al. (1969). "Two-photon Absorption in Germanium", *Journal of Experimental and Theoretical Physics*, 9: 130.

29. R. G. Wenzel, G. P. Arnold, et al. (1973). "Nonlinear loss in Ge in the 2.5 - 4 μm range". *Applied Optics* 12: 2245-2247.

30. A. F. Gibson, C. B. Hatch, et al. (1976). "Two-photon absorption in indium antimonide and germanium". *Journal of Physics C*, 1976, vol 9: 3259–3275.

31. C. Rauscher, and R. Laenen (1997). "Analysis of picoseconds mid-infrared pulses by two-photon absorption in germanium". *Journal of Applied Physics, 1997, vol* 81: 2818.

32. A. G. Akmanov, B. V. Zhdanov, et al. (1996). Two-photon absorption of IR radiation and its optical saturation in n-type gallium antimonide. *Quantum Electronics*, Turpion Ltd. 26: 882-883.

33. M. D. Turner, W. B. Roh, and K. L. Schepler, "Nonlinear optical properties of GaSb and GaInAsSb and their application for phase conjugation in degenerate four-wave mixing," *J. Opt. Soc. Am. B,* vol 17, 790-804 (2000).

34. J. Yepez, "AFRL Directed Energy Directorate Mission Brief " Phillips Research Site, *Air Force Research Laboratory*, 2005.

35. B. C. Stuart, M. D. Feit, A. M. Rubenchik, B. W. Shore, and M. D. Perry, "Laser-induced damage in dielectrics with nanosecond to subpicosecond pulses." *Physical Review Letters*, vol. 74: *APS*, 1995, pp. 2248-2251.

36. S. H. Lee, J. S. Lee, S. Park, and Y. K. Choi, "Numerical Analysis on Heat Transfer Characteristics of a Silicon Film Irradiated by Pico-to Femtosecond Pulse Lasers." vol. 44: *Taylor and Francis Ltd*, 2003, pp. 833-850.

37. L. V. Keldysh, "Ionization in the Field of a Strong Electromagnetic Wave", *Sov. Phys. JETP* 20, 1307 (1965).

38. B. Rethfeld, H. Krutsch, and D. H. H. Hoffmann, "Towards a Self-Consistent Model of Dielectric Breakdown under Short-Pulse Laser-Irradiation," in *GSI Plasma Physics Annual Report 2006*, paper TT-15, 2006.

39. A. P. Joglekar, H. Liu, G. J. Spooner, E. Meyhöfer, G. Mourou, and A. J. Hunt, "A study of the deterministic character of optical damage by femtosecond laser pulses and applications to nanomachining." *Applied Physics B*, vol. 77: *Springer*, 2003, pp. 25-30.

40. H. Furuse, N. Mori, et al. (2006). "Midinfrared optical absorption in germanium measured with a free-electron laser at room temperature", *Physical Review B*, *APS*. 74: 205206.

41. T. Morishita, M. Okunishi, K. Shimada, G. Prümper, Z. Chen, S. Watanabe, K. Ueda, and C. D. Lin, "High-energy ATI spectra of rare gas atoms," *Journal of Physics B*, vol. 42, p. 105205, 2009.

42. J. C. Phillips and J. A. Van Vechten, "Dielectric Classification of Crystal Structures, Ionization Potentials, and Band Structures," *Physical Review Letters*, vol. 22, pp. 705-708, 1969.

43. R. A. Dragoset, C. W. Clark, W. C. Martin, P. J. Mohr, and B. N. Taylor, "Periodic Table: Atomic Properties of the Elements," *National Institute of Standards and Technology Special Publication (NIST SP) - 0966*, 2002.

44. "Lasers and laser-related equipment -- Determination of laser-induced damage threshold of optical surfaces -- Part 1: 1-on-1 test", *International Organization for Standardization*, 2000.

45. G. E. Jellison Jr, D. H. Lowndes, D. N. Mashburn, and R. F. Wood, "Time-resolved reflectivity measurements on silicon and germanium using a pulsed excimer KrF laser heating beam." *Physical Review B*, vol. 34: *APS*, 1986, pp. 2407-2415.

46. D. Seo, L. C. Feldman, N. H. Tolk, and P. I. Cohen, "Interaction of high-power infrared radiation with germanium", *SPIE Laser-Induced Damage in Optical Materials*, vol. 7132, 2008, p. 713216.

47. L. P. Gonzalez, J. M. Murray, V. M. Cowan, and S. Guha, "Measurement of the nonlinear optical properties of semiconductors using the irradiance scan technique." *SPIE* vol. 6875, 2008, p. 68750R.

48. J. B. McKay, "Power Scaling Feasibility of Chromium-Doped II-VI Laser Sources and the Demonstration of a Chromium-Doped Zinc Selenide Face-Cooled Disk Laser", DTIC number ADA408929, *Air Force Institute of Technology Dissertation*, 2002.

49. T. J. Carrig, G. J. Wagner, W. J. Alford, and A. Zakel, "Chromium-Doped Chalcogenide Lasers," In Near-and Mid-Infrared Solid-state Lasers Vol. 5460, S. Alphan, G. F. James, and R. P. Clifford, Eds.: *SPIE*, 2004, Pp. 74-82.

50. Gonzalez, L., Guha, S., Rogers, J. W., and Sheng, Q., "An effective z-stretching method for paraxial light beam propagation simulations," *Journal of Computational Physics* vol. 227, 7264–78, 2008.

51. L. P. Gonzalez, "Accurate Determination of Nonlinear Optical Parameters of Semiconductors at Infrared Wavelengths," *University of Dayton Dissertation*, 2009.

52. E. Sorokin, I. T. Sorokina, M. S. Mirov, V. V. Fedorov, I. S. Moskalev, and S. B. Mirov, "Ultrabroad continuous-wave tuning of ceramic Cr: ZnSe and Cr: ZnS lasers," in *Advanced Solid-State Photonics* (Optical Society of America, 2010), p. AMC2.

53. R. H. Page *et. al*., "Recent developments in Cr^{2+}-doped II-VI compound lasers," in *OSA Trends in Optics and Photonics, Advanced Solid-state Lasers*. vol. 1, S. A. Payne and C. Pollock, Eds. Washington, DC: Optical Society of America, 1996, pp. 130-136.

54. L. D. DeLoach *et. al*., "Transition metal-doped zinc chalcogenides:spectroscopy and laser demonstration of a new class of gain media," *IEEE Journal of Quantum Electronics*, vol. 32, pp. 885-895, 1996.

55. I. S. Moskalev, V. V. Fedorov, S. B. Mirov, P. A. Berry, and K. L. Schepler, "12-Watt CW Polycrystalline Cr^{2+}:ZnSe Laser Pumped by Tm-fiber Laser," *Advanced Solid State Photonics* (Optical Society of America, Denver, Co, 2008), p. WB30.

56. P. A. Berry and K. L. Schepler, "High-power, widely-tunable Cr^{2+}:ZnSe master oscillator power amplifier systems," *Optics Express*, vol. 18, pp. 15062-15072, 30 Jun 2010.

57. L. F. Johnson, R. E. Dietz, and H. J. Guggenheim, "Optical Maser Oscillation from Ni^{2+} in MgF_2 Involving Simultaneous Emission of Phonons," *Physical Review Letters*, vol. 11, p. 318, 1963.

58. L. F. Johnson, R. E. Dietz, and H. J. Guggenheim, "Spontaneous and Stimulated Emission From Co^{2+} Ions In MgF_2 and ZnF_2," *Applied Physics Letters*, vol. 5, pp. 21-22, 1964.

59. G. Grebe, G. Roussos, and H. J. Schultz, "Cr^{2+} excitation levels in ZnSe and ZnS", *Journal of Physics C: Solid-state Physics*, vol. 9: p. 4511-4516, 1976.

60. P. A. Berry and K. L. Schepler, "Modeling of time-dependent thermal effects in Cr-doped zinc selenide thin disks," in *Proc. SPIE*, Vol. 6100, 61000X, 2006.

61. I. T. Sorokina, "Cr^{2+}-doped II–VI materials for lasers and nonlinear optics," *Optical Materials*, vol. 26, pp. 395-412, 2004.

62. K. L. Schepler, R. D. Peterson, P. A. Berry, and J. B. McKay, "Thermal Effects in Cr^{2+}:ZnSe Thin Disk Lasers," *IEEE Journal of Selected Topics in Quantum Electronics*, vol. 11, pp. 713-720, 2005.

63. A. Sennaroglu, U. Demirbas, A. Kurt, and M. Somer, "Concentration dependence of fluorescence and lasing efficiency in Cr^{2+}: ZnSe lasers," *Optical Materials*, vol. 29, pp. 703-708, 2007.

64. K. L. Schepler, "Mid-IR transition metal lasers," in *Solid-state Lasers XVI: Technology and Devices*, San Jose, CA, USA, 2007, pp. 64510K-11.

65. A. Gallian *et. al*., "Hot-pressed ceramic Cr^{2+}:ZnSe gain-switched laser," *Opt. Express*, vol. 14, pp. 11694-11701, 2006.

66. P. Koranda *et. al*., "ZnSe: Cr^{2+} coherently pumped laser," *Optical Materials*, vol. 30, pp. 149-151, 2007.

67. F. Z. Qamar and Terence A. King (2004). "Passive Q-Switching of the Tm-Silica Fibre Laser Near 2 μm by a Cr^{2+}:ZnSe Saturable Absorber Crystal", The University of Manchester, *Optics Communications*, Volume 248, Issues 4-6, 15 April 2005, Pages 501-508

68. D. M. Simanovskii, H. A. Schwettman, H. Lee, and A. J. Welch, "Midinfrared Optical Breakdown in Transparent Dielectrics," *Physical Review Letters*, vol. 91, p. 107601, 2003.

69. I. S. Moskalev, V. V. Fedorov, S. B. Mirov, P. A. Berry, and K. L. Schepler, "12-Watt CW Polycrystalline Cr^{2+}:ZnSe Laser Pumped by Tm-Fiber Laser," in *Advanced Solid-state Photonics 2008*, Denver, Co, 2008, p. Wb30.

70. C. R. Pollock *et. al*., "Mode locked and Q-switched Cr:ZnSe laser using a SESAM," in *Advanced Solid-State Photonics 2005*, Washington, DC, 2004, p. TuA6.

71. I. T. Sorokina, E. Sorokin, and T. J. Carrig, "Femtosecond Pulse Generation From a SESAM Mode-Locked Cr:ZnSe Laser," In *CLEO/QELS Technical Digest*, Paper CMQ2 (Optical Society of America, Long Beach, Ca May 21-26, 2006)

72. I. T. Sorokina and E. Sorokin, "Chirped-Mirror Dispersion Controlled Femtosecond Cr:ZnSe Laser," In *Advanced Solid-State Photonics*, 2007, P. Wa7.

73. X. Zhang, Y. Wang, and Y. Ju, "LD-pumped actively Q-switched Tm, Ho: YLF laser at room temperature," *Optics and Laser Technology*, vol. 39, pp. 78-81, 2007.

74. Y. Bai, J. Yu, M. Petros, P. Petzar, B. Trieu, H. Lee, and U. Singh, "Highly efficient Q-switched Ho: YLF laser pumped by Tm: fiber laser," in *CLEO*, 2007.

75. O. A. Louchev, Y. Urata, and S. Wada, "Numerical simulation and optimization of giant pulse generation in 2 μm Tm, Ho lasers," *CLEO* 2007, pp. 1-2.

76. O. A. Louchev, Y. Urata, N. Saito, and S. Wada, "Computational model for operation of 2 μm co-doped Tm,Ho solid-state lasers," *Opt. Express* 15, 11903-11912, 2007

77.   E. Tuncel *et. al*., "Free-electron laser studies of direct and indirect two-photon absorption in germanium." vol. 70: *APS*, 1993, pp. 4146-4149.

78.   M. Levinstein, S. Rumyantsev, and M. Shur, "Handbook Series on Semiconductor Parameters", vol. 1,2. London: *World Scientific*, 1996, 1999. Available online at http://www.ioffe.ru/SVA/NSM/Semicond, accessed frequently in 2009 & 2010

79.   T. R. Harris, "Optical Properties of Si, Ge, GaAs, GaSb, InAs, and InP at Elevated Temperatures", *Air Force Institute of Technology Thesis,* 2010.

80.   R. N. Hall, "Electron-Hole Recombination in Germanium," *Phys. Rev*., Vol. 87, P. 387, 1952.

81.   E. Marin *et. al*., "Photoacoustic Determination of Non-Radiative Carrier Lifetimes," in *Journal of Applied Physics*. vol. 83, 1998, p. 2604.

82.   V. Kelley, "diNanoScope Software 7.0 User Guide", revision A, Veeco Instruments, 2006, p178

83.   R. M. Wood, "Laser-induced damage of optical materials: *Taylor & Francis*, 2003, p31-32, 64, 100.

84.   S. J. Sheldon, L. V. Knight, and J. M. Thorne, "Laser-induced thermal lens effect: a new theoretical model," *Applied Optics*, vol. 21, pp. 1663-1669, 1982.

85.   M. D. Dramicanin *et. al*., "Photoacoustic investigation of transport in semiconductors: Theoretical and experimental study of a Ge single crystal." *Phys. Rev. B*, vol. 51: *APS*, 1995, pp. 14226-14232.

86.   P. S. Dutta, H. L. Bhat, and V. Kumar, "The physics and technology of gallium antimonide: An emerging optoelectronic material," *Journal of Applied Physics*, vol. 81, p. 5821, 1997.

87.   V. Nathan, A. H. Guenther, et al. (1985). "Review of multiphoton absorption in crystalline solids", *JOSA B,* vol. 2: 294-316.

88.   Driggers, R. G. (2003). Encyclopedia of optical engineering, *Marcel Dekker*, p1508

89.   L. P. Gonzalez, J. M. Murray, S. Krishnamurthy, and S. Guha, "Wavelength dependence of two photon and free carrier absorptions in InP," Optics Express, vol. 17, pp. 8741-8748, 2009.

90.   D. Zwillinger and S. Kokoska, CRC standard probability and statistics tables and formulae, 30th ed.: *CRC Press*, 1996, equation 643, p 400

91.   J. P. Murray, private correspondence, Nov 2009.

92. J. F. Young, J. S. Preston, H. M. Van Driel, and J. E. Sipe, "Laser-induced periodic surface structure. II. Experiments on Ge, Si, Al, and brass," *Physical Review B*, vol. 27, pp. 1155-1172, 1983.

93. C. J. Stolz, M. D. Thomas, and A. J. Griffin, "BDS thin film damage competition," in *SPIE Laser-Induced Damage in Optical Materials*, 2008.

94. C. J. Stolz, D. Ristau, M. Turowski, and H. Blaschke, "Thin film femtosecond laser damage competition," in *SPIE Laser-Induced Damage in Optical Materials*, 2009, p. 75040S.

95. A. Othonos, H. M. Van Driel, J. F. Young, and P. J. Kelly, "Correlation of hot-phonon and hot-carrier kinetics in Ge on a picosecond time scale." *Physical Review B*, vol. 43: APS, 1991, pp. 6682-6690.

REPORT DOCUMENTATION PAGE

1. REPORT DATE *(DD-MM-YYYY)*	2. REPORT TYPE	3. DATES COVERED *(From – To)*
12-08-2010	Doctoral Dissertation	August 2007 – August 2010

4. TITLE AND SUBTITLE

All Solid-State Mid-IR Laser Development, Nonlinear Absorption Investigation and Laser-Induced Damage Study

5a. CONTRACT NUMBER

5b. GRANT NUMBER

5c. PROGRAM ELEMENT NUMBER
62204F

6. AUTHOR(S)

Torrey J. Wagner, Maj, USAF

5d. PROJECT NUMBER
2003

5e. TASK NUMBER
12

5f. WORK UNIT NUMBER
24

7. PERFORMING ORGANIZATION NAMES(S) AND ADDRESS(S)

Air Force Institute of Technology
Graduate School of Engineering and Management (AFIT/EN)
2950 Hobson Way, Building 640
WPAFB OH 45433-8865

8. PERFORMING ORGANIZATION REPORT NUMBER

AFIT/DS/ENP/10-S07

9. SPONSORING/MONITORING AGENCY NAME(S) AND ADDRESS(ES)

Dr. Kenneth Schepler
Air Force Research Laboratory, Sensors Directorate
AFRL/RYJW, 2241 Avionics Circle
WPAFB, OH 45433

10. SPONSOR/MONITOR'S ACRONYM(S)
AFRL/RYJ

11. SPONSOR/MONITOR'S REPORT NUMBER(S)

12. DISTRIBUTION/AVAILABILITY STATEMENT

APPROVED FOR PUBLIC RELEASE; DISTRIBUTION UNLIMITED.

13. SUPPLEMENTARY NOTES

14. ABSTRACT

In this research, nonlinear optical absorption coefficients and laser-induced damage thresholds are measured in Ge and GaSb, which are materials that are used in IR detectors. Using a simultaneous fitting technique to extract nonlinear absorption coefficients from data at two pulse widths, two-photon and free-carrier absorption coefficients are measured in Ge and GaSb at 2.05 and 2.5 μm for the first time. At these wavelengths, nonlinear absorption is the primary damage mechanism, and damage thresholds at picosecond and nanosecond pulse widths were measured and agreed well with modeled thresholds using experimentally measured parameters. The damage threshold for a single-layer Al_2O_3 anti-reflective coating on Ge was 55% or 35% lower than the uncoated threshold for picosecond or nanosecond pulses, respectively. It was necessary to develop a pulsed 2.5 μm wavelength laser to conduct these measurements, as prior lasers at this wavelength possessed insufficient pulse energy to induce nonlinear absorption or damage these materials. Using a Cr^{2+}:ZnSe gain medium, a 3.1 mJ pulse energy laser was created whose peak power exceeded all Cr2+:ZnSe literature by a factor of eight. The characteristics of the laser include nanosecond pulse width, 52% slope efficiency, beam quality of $M^2 = 1.4$, Gaussian spatial profile and a spectral line width of 110 nm.

15. SUBJECT TERMS

16. SECURITY CLASSIFICATION OF:			17. LIMITATION OF ABSTRACT	18. NUMBER OF PAGES	19a. NAME OF RESPONSIBLE PERSON
a. REPORT	b. ABSTRACT	c. THIS PAGE			Dr. Kenneth Schepler
U	U	U	UU	141	19b. TELEPHONE NUMBER *(Include area code)* (937) 528-8661; email: kenneth.schepler@wpafb.af.mil